Ab initio Structure Inversion for Amorphous Materials

A dissertation presented to

the faculty of

the College of Arts and Sciences of Ohio University

In partial fulfillment

of the requirements for the degree

Doctor of Philosophy

Bishal Bhattarai

December 2018

This dissertation titled

Ab initio Structure Inversion for Amorphous Materials

by

BISHAL BHATTARAI

has been approved for

the Department of Physics and Astronomy

and the College of Arts and Sciences by

David A. Drabold

Distinguished Professor of Physics and Astronomy

Joseph Shields

Interim Dean, College of Arts and Sciences

Abstract

BHATTARAI, BISHAL, Ph.D., December 2018, Physics and Astronomy

Ab initio Structure Inversion for Amorphous Materials (103 pp.)

Director of Dissertation: David A. Drabold

Advancement and understanding of amorphous materials has been limited by conventional computer simulations [1]. A *generic* approach of "*Melt-Quenching*" (MQ) with molecular dynamics (MD) has several shortcomings. First: a slow quenching rate limits model size for *ab initio* method while efficient empirical potentials undermine the accuracy of results. To overcome this restrictions in this dissertation we have modeled large and realistic models of different amorphous systems with an accuracy comparable to density functional theory (DFT) calculations. We have used a recently developed method Force Enhanced Atomic Refinement (FEAR) [2, 3]. FEAR offers the logical advantage of using *a priori* knowledge, but within an *ab initio* simulation framework. It utilizes Reverse Monte Carlo (RMC) technique [a simple stochastic scheme to find coordinates matching a diffraction experiment] and relaxation using *ab initio* interactions. We have extensively explored large systems with 648-800 atom utilizing the FEAR method to get a better understanding of these systems. We have used FEAR to generate amorphous carbon (648 atoms) across densities 0.95-3.5 g/cm^3. We study the low density regime of amorphous carbon and reveal that nano-porous carbon obtained in diffraction experiment is actually interconnected and wrapped form of amorphous graphene. We summarize our conclusion on amorphous graphene by thoroughly investigating and comparing its properties with two-dimensional amorphous graphene, crystalline graphene and schwarzite. In addition, vibrational properties of amorphous silica and amorphous carbon have been thoroughly studied.

In memory of my loving father

Murari Bhattarai

Acknowledgments

The past five years during my PhD has helped me to grow both as a researcher and as a person. I was extremely lucky to have met people who are kind, supportive and understanding. Undoubtedly, without the support of them I would not have achieved my PhD. I would like to take this opportunity to thank all these wonderful people who have made my PhD study a perpetuating memory.

First and foremost, I would like to express my sincere gratitude to my advisor Prof. David A. Drabold. His dedicated guidance, continuous support and motivation has made my PhD possible. As an advisor, he is extremely knowledgeable, understanding and supportive. His enthusiasm, passion and quest for science has left me a long-lasting impression. I see him as an ideal *role model* for any young researcher. I feel really lucky to have him as my advisor and I will cherish his teachings throughout my life.

I would also like to thank Prof. Gang Chen at Ohio University who has been extremely supportive and gave me valuable suggestions from an experimental perspective. I would also like to thank Prof. Parthapratim Biswas at the University of Southern Mississippi for his helpful suggestions and discussions in all the projects that we worked together. I would also like to thank Prof. Martin Kordesch and Prof. Sumit Sharma at Ohio University for serving in my thesis committee and for their valuable suggestions.

I would like to thank my colleagues Dr. Anup Pandey, Dr. Kiran Prasai, Dale Igram, Kashi Subedi and Rajendra Thapa for wonderful discussions and fond memories.

I want to extend my gratitude to my family: my mother and my brother. I would also like to thank my dear friends Abinash Pun, Rajib K. Pandit, Oscar Avalos, Zhejie Ding, Saroj Dhakal and Eliza Thapa for their unconditional support and encouragement through these years.

Lastly, I would also like to acknowledge all the funding agencies for their financial support. I would also like to thank Maryann Chase for providing the fund for the Vishwa

S. Shukla Memorial Scholarship. I am thankful to Ohio University for providing me an opportunity to pursue my PhD in this wonderful research environment.

Table of Contents

List of Tables

Table Page

List of Figures

1 Introduction

1.1 Background

Amorphous materials have many applications ranging from art to optoelectronics. Our ancestors had knowledge of making glass since Bronze age (ca. 3000 BC), yet the structure of these materials have only been explored in the last century [4]. In spite of these recent studies, the structure of amorphous materials are not fully understood as compared to crystalline materials. Amorphous materials like amorphous silicon (a-Si) and its hydrogenated amorphous silicon (a-Si:H) counterpart have myriad applications in solar cell technologies, thin-film transistors, active-matrix displays, etc [5]. Similarly, amorphous carbon (a-C) has multiple applications depending upon sp^3 content. a-C with high sp^3 content is widely used for coating for optical windows, hard drives and other electromechanical devices [6, 7]. Meanwhile, porous carbons are used in several applications like gas storage, filtration, energy and steel production [6, 8]. Amorphous silica (a-SiO_2) or window glass has high mechanical resistance and high dielectric strength which acts as a major material in microelectronics. a-SiO_2 alloyed with transition metal has been explored as a potential candidate for solid electrolyte used in Conducting Bridge Random Access Memory(CBRAM) technologies [9].

1.2 Structural Order

Structural order is a fundamental concept in condensed matter physics. In this concept Bravais lattice, an array of points in space such that if any point is considered as origin than position vector ($\vec{R}$) satisfies,

$$\vec{R} = n_1 \vec{a}_1 + n_2 \vec{a_2} + n_3 \vec{a_3} \tag{1.1}$$

Where $\vec{a}_1$, $\vec{a_2}$ and $\vec{a_3}$ are fixed lattice vectors and n's are integers.

Further, every lattice point is associated with identical group of atoms called a basis and in a perfect crystal every basis is identically located and oriented with respect to its lattice point [10]. In the early 1900's William Henry Bragg detected these ordered patterns by shining X-rays in a crystalline material and discovered which is now well known as"Bragg diffraction" patterns. This finding led to a whole new field of diffraction experiments and by analyzing these diffraction angles and wavelength of the X-rays, one can ascertain the full structure of a crystal. The determination of *unit cell* which only contains few atoms and repetition of these unit cells (building blocks) can generate the structure of whole crystal [11].

Meanwhile, this is problematic for amorphous materials as the unit cell for amorphous materials can be regarded as infinite size with no patterns (*unit cell*) to repeat and obtain the structure [11]. The lack of a fundamental repeated structure in amorphous solids pose question like,

Why should we study amorphous system: isn't it structurally random and chaotic ?

We follow the definition of *S. R. Elliott* [11] to answer this question. The structural ordering in amorphous solid is non-periodic but not truly random and has a statistical nature. *Elliott* defines amorphous solids by sub-dividing microscopic structure of amorphous solids in two parts: short-range order ($0 - 5$ Å) and medium-range order ($5 - 20$ Å). These microscopic length scales are based on the typical diffraction probes (e.g. X-rays or neutron) used to study amorphous materials.

Amorphous materials lack long range order thus have non unique structural solution. The spatial correlation present also rapidly decays with distance. Despite the lack of long range information, local environment information such as coordination, chemical ordering, bond length distribution, bond angles are used to characterize these systems. Short range order is of paramount importance as it reveals the *chemical* and coordination

nature of a solid [12]. The information about the coordination number (number of atoms connected to a particular atom) is crucial to reveal different bonding types [12].

1.3 Theoretical Study of Amorphous Solids

1.3.1 Continuous Random Networks

One of the earliest theoretical approaches to study amorphous solids was proposed by *W. H. Zachariasen* [13] in 1932. In *Zachariasen's* approach to amorphous materials one interprets them as a *continuous random network* (CRN). The CRN concept is a simplified model to study amorphous solids. The CRN satisfy these following conditions [12]:

- Every atom has perfect coordination[1] and is devoid of defects or dangling bonds. For a covalent system, coordination satisfies Mott's $8 - N$ rule [14] ("N" is number of valence electrons).
- The nearest neighbors distance is same or similar to crystal.
- The bond angle distribution exhibits some dispersion (no spread in crystal).
- Absence of long range order (LRO).

Early models studied using CRN methods were hand-made models [15, 16] but later (1974-1976) *Guttman* [17–19] studied CRN using computer models.

1.3.2 Wooten-Weaire-Winer (WWW) Method

Wooten-Weaire-Winer (WWW) in 1985 introduced a bond-switching algorithm which was able to produce appealing CRN models for amorphous column IV materials [20, 21]. This method was extended to binary compounds by *Mousseau and Barkema*. The WWW method is successful for modeling systems where *a priori* knowledge of bonding environments is known and, it has been used as a backbone to

[1] Each atom has same number of neighbors.

study several materials [22–25]. The WWW method is limited in a sense that it uses *a priori* information of bonding environment, has only been used to model handful of systems and it uses an extremely simple potential. In spite of the limitation of this method, WWW models of amorphous silicon (*a-Si*) and tetrahedral amorphous carbon (*t-aC*) are still considered best models with lowest strain and perfect coordination.

1.3.3 Method of Molecular Dynamics

Molecular dynamics (MD) simulations are popular methods used to simulate amorphous systems. In MD simulation, atoms are represented as point particles, guided by classical Newton equations of motion. These equations are integrated over time to obtained the dynamical evolution of system. In amorphous systems we use method of "*melt and quench*"[2] (MQ) to prepare models via MD simulation. In MQ scheme we start the simulation by forming a liquid (above melting point). This liquid phase (*"melt"*) is then well-equilibrated for many MD steps such that the model essentially forgets how it was created. Equilibration at such high temperature helps the system to organize in the liquid state such that all initial biases are forgotten. After forming a well equilibrated liquid, the system is allowed to quickly cool (*"quench"*) essentially copying the glass-formation process [4]. MD approach is very useful when the structure of liquid and glass are similar and the ordering for both liquid and glass are local [4]. Powerful computers have aided computational study of materials. In particular, MD techniques have certainly benefited from this development aiding to timescale and accuracy of MD based simulation. The MD process is mostly used with two types of interactions to prepare a model. The choice of interactions depends upon the requirement and has its own benefits and shortcoming. We discuss the two main types of interactions in the following subsections:

[2] Also referred as *"cook and quench"* in some texts.

1.3.3.1 Empirical or Classical Interactions

Empirical or classical interactions for a system are generated by guessing the correct functional form for a model potential with free parameters [4]. The free parameters are adjusted to ensure correct properties (bond-length, bond angle etc.) of the material [4]. MD with classical interactions is extremely efficient and one can model large systems. The system size for these simulation range from several thousands to millions of atoms.

In spite of its efficiency, MD simulations with empirical interactions is plagued by transferability issues. Simple potentials fail for covalent systems and are difficult to use with Carbon. Carbon is hard to model, as it has different bonding (sp^3 , sp^2 , sp) preferences at various densities. Meanwhile, silicon is easier to model for empirical interactions as the bonding preference is homogeneously tetrahedral with other parameters (like bond-length, bond-angle) also being constant for all the atoms. This method is also applicable to materials in which ionicity forbids wrong bonds (e.g. a-SiO_2) [4].

1.3.3.2 Density Functional Theory (DFT) Approach

The limitation of pair potentials can be resolved by treating the atoms quantum mechanically. This suggests working with a many body Schrodinger equation the solution of which is prohibitively complex.

"It therefore becomes desirable that approximate practical methods of applying quantum mechanics should be developed, which can lead to an explanation of the main features of complex atomic systems without too much computation."

-Paul Dirac in "Quantum mechanics of many-electron systems" [26].

This formulation was simplified by Hohenberg, Kohn and Sham [27, 28]. In density functional theory (DFT) approach, the electron ground state density ($n_0(r)$) is considered a fundamental variable instead of many-body Schrodinger wavefunctions [29]. DFT is

based on the fact that there exists an effective potential (V_{eff}) which depends only on electron density ($n_0(r)$) i.e. "*Hohenberg-Kohn theorem*". The challenge with this formulation is that the exact form of this effective potential is unknown and various approximations are used to obtain (V_{eff}). The local density approximation (LDA) [30–32] and generalized gradient approximation (GGA) [33–35] are the two most widely used approximations to solve the problem. The details of these approximations and DFT are detailed in standard reference [29].

In this work we have extensively used two DFT codes namely: (a) Spanish Initiative for Electronic Simulations with Thousands of Atoms (SIESTA) [36] and (b) Vienna *Ab initio* Simulation Package (VASP).

SIESTA is a density functional code that uses the standard Kohn-Sham [27, 28] self-consistent DFT method with LDA [30–32] or GGA [33–35] approximations. It uses pseudo-atomic orbitals as a basis sets, allowing the user to choose different size of basis set (single-ζ, double-ζ, single-ζ polarized and so on.). This option to choose basis set is particularly useful to accelerate calculations. It also has an option of Harris energy functional [37], a non self-consistent approach to approximate Kohn-Sham energy (useful for covalent system). This approximation saves considerable CPU time [29].

Meanwhile, VASP is another density functional code which we have extensively used to carry out our calculations. In VASP molecular dynamics (MD) simulations are carried out using either pseudo-potentials or the projector-augmented wave method (PAW) and using a plane wave basis set. The electron and ion interactions in VASP is described using either ultra-soft Vanderbilt pseudo-potentials [38] or PAW method [39, 40]. The exchange correlation can be approximated using either LDA or GGA approximations.

1.3.4 Inverting Experiments

1.3.4.1 Reverse Monte Carlo (RMC) Method

Reverse monte carlo (RMC) method offers a different approach to model amorphous system which assumes a sensible principle that a model should agree with experiment [4]. A model is constructed explicitly to agree with experimental data. This approach was developed and extended by *McGreevy and Puzstai* in 1988 [41, 42]. The basic idea is to minimize (χ^2), the difference between experiment and model:

$$\chi^2 = \sum_i \left[\frac{F_E(k_i) - F_C(k_i)}{\sigma(k_i)} \right]^2 \tag{1.2}$$

Here, $F_E(k_i)$ represents the experimental data, $F_C(k_i)$ represents the model and $\sigma(k_i)$ is the weight of the experiment. In equation(1.2), value of i extends over all data points. This allows us to determine atomic positions to make a model agree with several experimental result. These experimental data typically include pair-distribution function, X-ray or neutrons scattering data, short-range atomic structure (bond length, coordination number, bond angle and so on). Logically, it makes sense to include as many experiments as possible. However, in reality this incorporation of multiple experiments is extremely difficult to minimize with assignment of weight factor ($\sigma(k_i)$) becomes increasingly challenging.

The basics of reverse monte carlo (RMC) method can be summarized as [42],

(1) Start by placing N atoms in a periodic supercell randomly with the correct density i.e. consistent with the experimental data. Impose a condition for minimum distance of approach between atoms, typically chosen $20 - 30\%$ lower than the average bond length of the system.

(2) Compute value of χ_0^2 using equation (1.2).

(3) Move an atom chosen at random, within the allowed maximum move distance. If any two atoms are closer than the minimum distance approach (cut-off) reject the move. Choose another new atom at random and again move within the allowed distance until it satisfies the minimum distance of approach condition.

(4) Compute the new value of χ_n^2 using equation (1.2) for this new configuration.

(5) If $\chi_n^2 < \chi_0^2$ move is accepted and the new configuration becomes the old configuration. Continue with steps 2-5 until desired convergence of χ^2 is achieved. If $\chi_n^2 > \chi_0^2$ accept with metropolis probability else reject the move. Repeat steps 2-5 until desired convergence is achieved.

Amorphous solids as discussed in section (1.2) lack long range order thus simply inverting diffraction data unguided with any constraints does not result in chemically sensible solution of a system. This is the major drawback of RMC. Several constraints have to be incorporated into the cost function to provide meaningful chemical description of the system as RMC method by itself does not include any kind of interactions. This however introduces bias into the modeling.

1.3.4.2 Hybrid RMC Method

As RMC does not include any interatomic interactions appropriate supplementary information has to be included to make a *chemically* meaningful model. Several Hybrid versions have been proposed to include energy functional based constraints [43]. These energy functional constraints minimize potential energy (empirical or *ab initio*) in addition to structural minimization. This minimization of potential have been implemented differently by different authors for e.g. it can occur after every RMC step, alternating between RMC steps and so on. To name few of these methods, hybrid reverse monte carlo method (HRMC) [44], experimentally constrained molecular relaxation

(ECMR) [45, 46], monte carlo method with molecular mechanics [47] and the force enhanced atomic refinement (FEAR) method [2, 3].

1.3.4.3 Force Enhanced Atomic Refinement (FEAR) Method

Force enhanced atomic refinement (FEAR) is a recently developed hybrid method used to invert diffraction data. FEAR has been implemented with both empirical and *ab initio* framework. FEAR method ability to predict accurate structure with correct chemical composition, starting from a random structure without any constraints has been its major feature of this approach. FEAR is an efficient and robust method to model different amorphous systems. It has been so far successfully applied to *a-Si*, *a-SiO*$_2$, Ag-doped *GeSe*$_3$ and a-*C* at various densities [2, 3, 48–50]. In the case of amorphous silicon, FEAR has been successfully implemented for up to 1024 atoms to create *ab inito* based models [51].

To tersely define FEAR, we begin with some definitions. For a energy functional $V(X_i....X_n)$ and atomic coordinates $\{X_i\}$, we compute χ^2 which is the discrepancy between a diffraction experiment and computer model. We try to find a set of atomic coordinates $\{X_i\}$ with the property that "$V(X_i....X_n)$" is *minimum* for a configuration and simultaneously χ^2 is within experimental error. FEAR consists of (i) starting with a random structural model at an assumed density (consistent with the experimental data density), (ii) invoking N accepted RMC moves followed by M relaxation steps (conjugate-gradient (CG) or gradient descent) using *ab initio* interactions. The second step (ii) is iterated to convergence (fitting the experimental data and finding a suitable minimum of DFT interactions). Accurate and unbiased chemical information is included in the CG step.

1.4 Observables for Amorphous Materials

Amorphous materials are characterized by atomic local environments. This local information can be described mathematically using several descriptors. Discussion on

common notation used in total scattering has been discussed else where [52]. We briefly define the most used definitions in this dissertation below.

1.4.1 Static Structure Factor

The static structure factor for amorphous solids is experimentally obtained by X-ray, neutron or electron diffraction. The details are available elsewhere [10, 11, 53]. In this dissertation we follow the definition presented in [10],

$$S(Q) = 1 + 4\pi\rho_0 \int_0^\infty dr r^2 \frac{sin(Qr)}{Qr}(g(r) - 1) \tag{1.3}$$

Here, $S(Q)$ is the total static structure factor and $g(r)$ is the pair correlation function or radial distribution function (RDF), which gives the corresponding structural information in real space.

1.4.2 Pair Distribution Function

Conversely, the pair correlation function $g(r)$ can be defined as, [10]

$$g(r) = 1 + \frac{1}{2\pi^2\rho_0} \int_0^\infty [S(Q) - 1] \frac{Q^2 sin(Qr)}{Qr} dQ \tag{1.4}$$

$g(r)$ is obtained by Fourier transform of $S(Q)$.

1.4.3 Ring Statistics

Ring statistics is another crucial information which gives the connectivity of atoms in a system. The most common definitions of ring statistics have two criterion:

(1) The connected atoms form a closed loop (i.e. starting and ending at same node) and number of connected atoms is greater than two.

(2) The number atoms connected in a loop is the shortest path for the starting node.

The number of atoms connected in the closed loop is defined as the ring size for that starting node. *King's* and *Franzblau's* definitions [54, 55] of ring statistics are widely followed. Ring statistics is crucial to measure accuracy of amorphous model (a-Si) as RMC prepared or very quick quench rate results in models with a lot of defects reflected by the increase of small rings (ring size 3-4) [43]. These quantities ($S(Q)$, $g(r)$ and ring statistics) can be readily obtained by using a open-source software ISAACS [56].

1.5 Electronic Structure

In amorphous solids, electronic structure is described by the electronic density of states (EDOS). The lack of periodicity in amorphous solids implies electrons cannot be expressed as Bloch states [11]. The energy eigenvalues E_i are important to describe electronic density of states (EDOS) in amorphous solids. In particular, we carryout DFT calculations and use the Kohn-Sham eigenvalues to describe the EDOS. We can define EDOS as below [29],

$$D(E) = \frac{1}{N}\sum_{i=1}^{N}\delta(E - E_i), \tag{1.5}$$

Where N is the size of basis set, E_i is the i^{th} eigenvector and $D(E)$ is the electronic density of states. The EDOS is an important descriptor for amorphous solids as several experimental techniques (photo-emission spectroscopy, electron spin resonance etc. [11]) depend upon the electronic spectrum. This makes EDOS an important observables to analyze a model. In a similar manner projected density of states (PDOS) also can be expressed as,

$$D_n(E) = \sum_{i=1}\delta(E - E_i)|<\phi_n|\psi_i>|^2, \tag{1.6}$$

Where ϕ_n is the local orbital, ψ_i is the i^{th} eigenvector and $D(E)_n$ is the projected electronic density of states on site n.

1.5.1 Electronic Localization

The electronic states in amorphous solids are not all spatially extended as in case of crystals. The defects and inherent disorder present in amorphous solids result in localized states [57]. In most cases, localization occurs in edges i.e conduction and valance band edges whereas most part of the system are extended [11]. The electronic localization can be quantified by computing inverse participation ratio (IPR). IPR, measures number of sites over which a wavefunction has a significant value. Mathematically IPR can be evaluated as [58],

$$\mathcal{I}(\psi_j) = N\frac{\sum_{i=1}^{N} a^{j4}}{\left(\sum_{i=1}^{N} a^{j2}\right)^2}, \tag{1.7}$$

where, $\psi_j = \sum_{i=1}^{N} a_i^j \phi_i$ is the jth eigenvector and ϕ_i is a local atom-centered orthogonal basis orbital. For a completely localized state, $\mathcal{I}(\psi_j)$=1 (only one atomic site contributing to that state). Small IPR are due to the extended states, where the electronic wavefunctions are more evenly distributed in space. Technical modifications are required for a non-orthogonal representation in Equation (1.7).

1.6 Vibrational Properties

The low-energy modes are related to mechanical properties and low temperature thermal conductivity of a material [59–62]. Thermal properties of materials are of key interest to both the scientific and engineering community especially heat transport [61].

The calculation of dynamical properties is carried out in the harmonic approximation [11]. The dynamical matrix is the key ingredient to analyze the vibrational properties of the model, which is obtained from a well relaxed system for which the

inter-atomic forces can be evaluated. The dynamical matrix is given by the relation [63],

$$D_{\alpha i,\beta j} = \frac{1}{(m_i m_j)^{\frac{1}{2}}} \frac{\partial^2 \phi}{\partial u_{\alpha i} \partial u_{\beta j}} \tag{1.8}$$

where, ϕ is the total energy of the system, m's are the ionic masses of the atoms and α and β are the Cartesian coordinates of atom i and j, respectively. The indices i and j run over the atoms. Now, when the i^{th} atom is displaced by $\Delta x_{\alpha i}$ in the α direction, the forces($F_{\beta j}$) on all the atoms are computed, so that the above relation can be replaced by [63],

$$D_{\alpha i,\beta j} \approx \frac{1}{(m_i m_j)^{\frac{1}{2}}} \frac{F_{\beta j}}{\Delta x_{\alpha i}} \tag{1.9}$$

The dynamical matrix is obtained by displacing each atom in 6-directions ($\pm x$,$\pm y$,$\pm z$) with a small displacement of ($\sim 0.02\ A^o$) . After, each such displacement an *ab initio* force calculation is performed to obtain the force constant matrix resulting from the displacement of each atom from it's equilibrium position. The eigenvalue problem reads,

$$\sum_{\alpha\beta} D_{\alpha i,\beta j} e^n_{\beta j} = -\omega_n^2 e^n_{\alpha i} \tag{1.10}$$

where, ω_n and $e^n_{\alpha i}$ represent the $3N$ eigenfrequencies and the eigenvectors respectively.

If ω is the frequency then $g(\omega)d\omega$ describes the number of modes within the interval [ω, $\omega + d\omega$], where $g(\omega)$ represents the VDOS of the system. The VDOS for amorphous systems with N number of atoms is defined as,

$$g(\omega) = \frac{1}{3N} \sum_{i=1}^{3N} \delta(\omega - \omega_i) \tag{1.11}$$

1.6.1 Vibrational Localization

We can evaluate the localization of different vibrational modes near the band edges oscillating with different frequencies by computing inverse participation ratio (IPR) much like the case for electrons. The IPR can be easily calculated from the normalized displacement vectors, and the IPR for the vibrations can be defined as:

$$\mathcal{I} = \frac{\sum_{i=1}^{N} |u_i^j|^4}{\left(\sum_{i=1}^{N} |u_i^j|^2\right)^2} \tag{1.12}$$

Where, (u_i^j) is normalized eigenvector of j^{th} mode.

1.6.2 Specific Heat within Harmonic Approximation

The evaluation of the specific heat within the harmonic approximation is straightforward with the help of the density of states, $g(\omega)$. The only significant provision is that not all of the vibrational excitations can be represented with a finite size model: vibrational excitations with wavelength larger than our supercell size are not included in the obtained VDOS data [63]. With the VDOS in hand, we may compute the $C_v(T)$ by the relation [64],

$$C(T) = 3R \int_0^{E_{max}} \left(\frac{E}{k_B T}\right)^2 \frac{e^{E/k_B T}}{\left(e^{E/k_B T} - 1\right)^2} g(E) dE \tag{1.13}$$

where the VDOS, $g(E)$ is normalized to unity[3].

1.7 Outline of Dissertation

The rest of the dissertation is outlined in following manner. In Chapter 2 and Chapter 3, we extensively present our studies on vibrational properties of two amorphous systems.

[3] see Ref. [64] Sec III, page 45

In Chapter 2, we present our results for vibrational properties of large *ab initio* model of $a\text{-}SiO_2$. In Chapter 3, we present our result on DFT based simulation of low density carbon. We introduce FEAR based large and realistic models of amorphous solids in Chapter 4. In this work we highlight key points of these large size models and effectiveness of FEAR method over conventional methods to model amorphous system. We present details of our finding on *amorphous graphene* obtained by successful inversion of neutron diffraction data. We confirm *amorphous graphene* to be constituent part of low density amorphous carbon. This confirmation is based on detailed comparison of sp^2 models of 2D-graphene, crystalline/pristine graphene and schwarzite. In Chapter 5 conclusion of this work and future prospects are discussed. All the work presented in Chapter 3,4,5 have been already published in peer-reviewed journals [49, 50, 65, 66] and we present key highlights of these work in consequent Chapters.

2 Vibrations in Amorphous Silica

The work presented in this chapter has been published as B. Bhattarai, D.A. Drabold, Vibrations in amorphous silica, *J. Non-Cryst. Solids*, 439 (2016), 6-14.

2.1 Introduction

There has been much theoretical research to understand the physics of amorphous silica (a-SiO_2), yet a perfect model for the vibrational properties and derived quantities like the vibrational specific heat has been lacking. Phonon calculations demand a precise calculation to satisfactorily model the vibrational excitations. Significant controversy exists in the literature about artifacts of small structural models and/or imperfect inter-atomic potentials.

We have employed a 648-atom model of a-SiO_2 with self-consistent density functional interactions to study the vibrational properties of the system. We study the vibrational properties by diagonalizing the dynamical matrix which gives us the eigenvalues and eigenvectors (classical normal modes). Our results are in improved agreement with experiment and we present interesting new results for the low temperature specific heat. We thoroughly characterize these modes, by including the *Taraskin-Elliott* correction (connecting experiment and theory), and computing phase quotients and estimating bond stretching/bending behavior. Our work is also of some interest as the largest (648-atom) *ab initio* study of vibrations in amorphous silica presented to date.

2.2 Model and Methodology

The models of a-SiO_2 were obtained with the help of *ab initio* software "Spanish Initiative for Electronic Simulations with Thousands of Atoms "(SIESTA) [36], a density functional code using the local-density approximation (LDA) with *Ceperley-Alder* (CA) exchange correlation functional. The 648-atom model of a-SiO_2 consisted of 216 Si

atoms and 432 O atoms with a cube side length of |22.3| $\mathring{A}$. The simulation was performed with single-ζ basis, a self-consistent field and periodic boundary conditions, and the final model was relaxed using the conjugate gradient (CG) method. The simulation was *initially* performed at constant volume, sampling the Brillouin zone only the Γ ($\overrightarrow{k} = \overrightarrow{0}$) point to compute the forces and energies. During the final relaxation, the system was allowed to relax to zero pressure for the single-ζ Hamiltonian. This allowed the system volume to change and resulted in a non-cubic cell, with a slightly lower density of 1.95 g/cm^3 than the experimentally reported density. [4]

2.3 Structural Properties

For investigating vibrational properties of materials, a good structural model is required and *ab initio* interaction have been the most reliable. In Fig. 2.1 we have compared the static structure factor $S(Q)$ of the 648-atom *a*-SiO_2 model with neutron-diffraction experimental results [69]. The comparison of $S(Q)$ shows an excellent fit for most of the range of Q, although some discrepancy after $Q \sim 11\mathring{A}^{-1}$. This discrepancy of the model and experiment is not due to finite size effects [22].

Partial structure factors were also calculated for the 648-atom model, which gave us a better idea of the origin of various peaks in the total structure factor $S(Q)$. Results for the partial structure factor are given in Fig. 2.2. We can infer from Fig. 2.2 that the first peak in $S(Q)$ arises from all three partial factors. The second peak in $S(Q)$ arises mostly from

[4] Previous simulations of this system have either constrained the volume to match experiment [67], or used empirical potentials that are concocted to reproduce the density [68]. This makes the pair correlations look slightly better, but then one is not considering vibrational excitations around the true minimum, an essential assumption of the Harmonic Approximation. In addition, by carrying out this zero-pressure simulation the cubic symmetry of the supercell also slightly breaks, yielding lattice vectors: $\langle 22.28, -0.24, -0.12\rangle$, $\langle -0.24, 22.48, 0.03\rangle$ and $\langle -0.13, 0.02, 22.07\rangle$. While the effect is fairly small compared to our earlier calculation (as characterized by the structure factor, and quantities like bond angle distributions), we think this is a more appropriate starting point than an artificially constrained case. We verified that with a more complete double-ζ basis, the lattice constant was indeed close to experiment, as expected. Since the vibrational calculations require 6N force calls, a phonon calculation with the full basis would be quite expensive for a cell with 648 atoms.

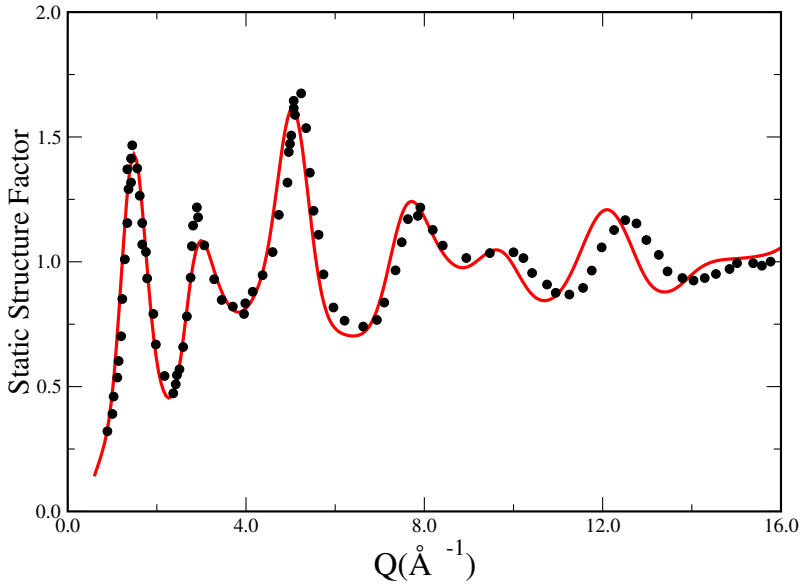

Figure 2.1: Calculated total neutron static structure factor for the 648-atom SiO_2 (solid red line) compared with the experimental data (black circle, neutron) [69].

the $Si-Si$ and $O-O$ correlations, while the contribution from $Si-O$ provides a partial cancellation. The third and fourth peak involves the contribution from $Si-Si$, $Si-O$ and $O-O$ depending upon the corresponding concentration and the scattering length. The Fourier counterpart of the structure factor (partial pair correlation) in real space is shown in Fig. 2.2. The first sharp peak of the pair correlation function gives us information about the bond length between nearest neighbors and the results obtained from the plot shows that the first peak of $Si-Si$ bonds is at 3.23 Å, similarly $Si-O$ and $O-O$ have their first maximum at 1.65 Å and 2.71 Å respectively. The average pair distances reported are, 3.100(0.113)Å, 1.621(0.022)Å and 2.65(0.109)Å for the $Si-Si$,$Si-O$ and $O-O$ respectively. The numbers in the brackets are the standard deviation for the data [70].

We have also reported bond angle distribution of our 648-atom model a-SiO_2 (Fig. 2.3). This is in agreement with our previous results for the 192-atom model [22]. The obtained structure has an average $O-Si-O$ angle of 108.97^o which is close to the

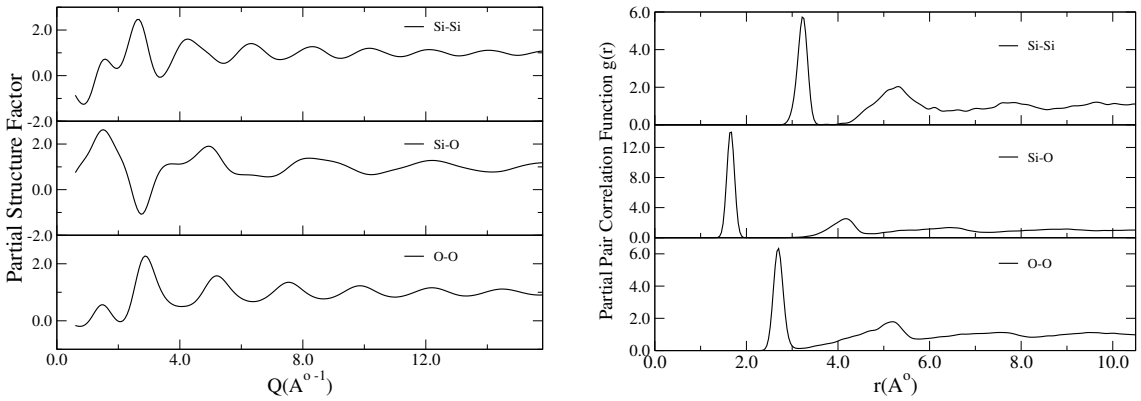

Figure 2.2: **(Left panel)** Calculated partial structure factors for the 648-atom model of *a*-SiO_2 , **(Right panel)** Calculated partial pair correlation functions for the 648-atom model of *a*-SiO_2 .

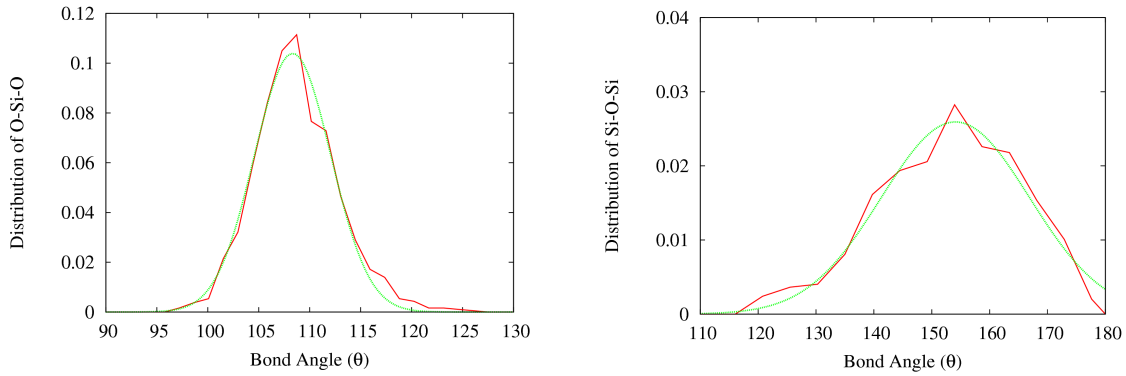

Figure 2.3: **(Left panel)** Bond-angle distribution function, $O-Si-O$(red),gaussian-fit (dotted green), **(Right panel)** Bond-angle distribution function, $Si-O-Si$ (red,), gaussian-fit (dotted green).

tetrahedral angle of 109.47 ^{o}. The broadening of the $Si-O-Si$ angles is consistent experimental results which also vary within the range of 142^o - 152^o [71]. It is also to be noted that different measurements give slightly varying results. The FWHM (gaussian fit)

for the two bond angle distributions $O-Si-O$, $Si-O-Si$ are 8.81^o and 31.21 ^{o} respectively.

2.4 Electronic Density of States and Localization

The electronic properties were analyzed with the electronic density of states (EDOS) and localization of different energy eigenstates. The localization is obtained by calculating Fig. 2.4 shows the plot of the EDOS and IPR.

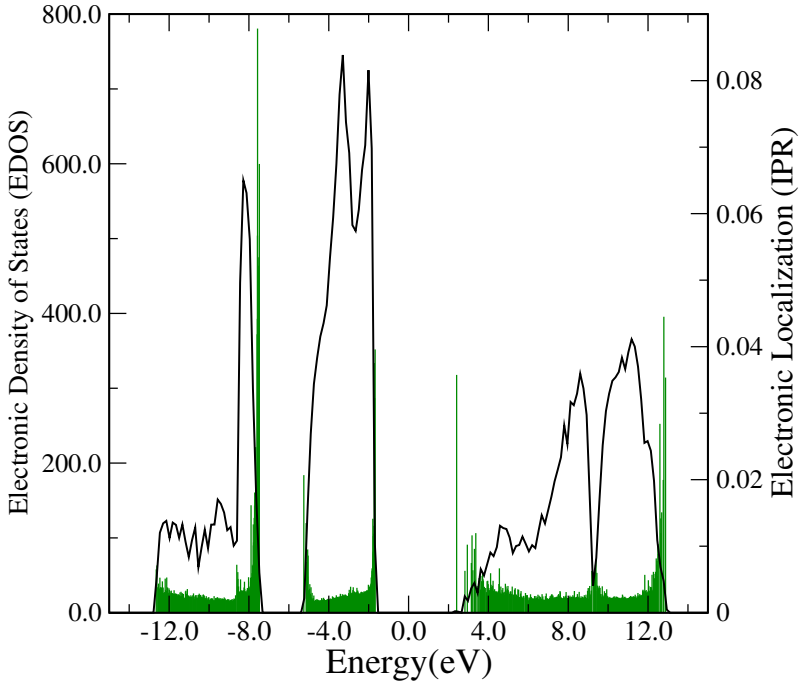

Figure 2.4: Electronic Density of States (EDOS) (black, solid line) and the IPR (green, drop lines), with the Fermi Energy shifted to 0 ev for 648-atoms a-SiO_2 model.

2.5 Dynamical Properties

If ω is the frequency then $g(\omega)d\omega$ describes the number of modes within the interval [ω, $\omega + d\omega$], where $g(\omega)$ represents the VDOS of the system. The VDOS for amorphous systems with N number of atoms is defined as,

$$g(\omega) = \frac{1}{3N} \sum_{i=1}^{3N} \delta(\omega - \omega_i) \tag{2.1}$$

We evaluate the VDOS by Gaussian broadening the eigenvalue with the standard deviation σ = 2.5 meV or 20.15 cm^{-1}(See Fig. 2.5). The first three frequencies are very close to zero, and arise from supercell translations. These have been neglected for the evaluation of both VDOS and derived quantities like specific heat.

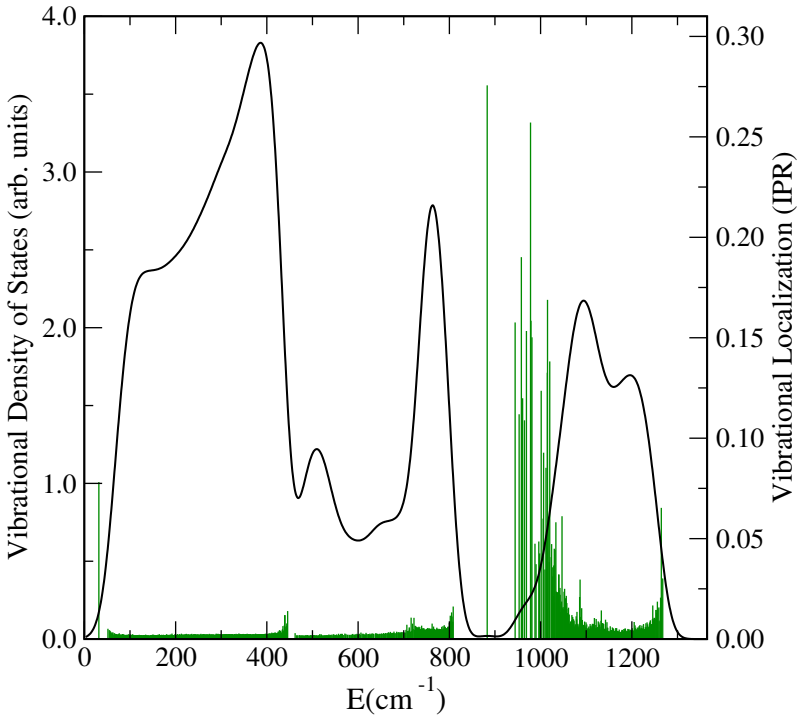

Figure 2.5: Vibrational Density of States (VDOS) (black, solid line) and the IPR (green, drop lines) for 648-atom a-SiO_2 model.

The VDOS of amorphous silica shows several peaks. Our 648-atom model shows well-defined peaks occurring at low frequencies at 390 and 507 cm^{-1}, and intermediate frequency at 766 cm^{-1}. At high frequency the two peaks are at frequencies 1095 cm^{-1} and 1198 cm^{-1}.

The VDOS of amorphous SiO_2 has been well studied. In celebrated work, *Bell and Dean* [15] reported peaks at frequencies near 400 cm^{-1}, 550 cm^{-1}, 750 cm^{-1} and 1050 cm^{-1}. *Bell and Dean* [15] were able to evaluate the effects of vibration due to the non-bridging oxygen atoms and their effects on VDOS. The importance of the motion of non-bridging oxygen atoms was vital for the peaks obtained at 300 cm^{-1} and 850 cm^{-1}. The bending motion of non-bridging oxygen (NB) plays a large part for motion at 300 cm^{-1} and the peaks observed at 850 cm^{-1} is mostly due to the stretching motion of non-bridging oxygen (NS).

The total density of states is projected onto the two species according to their respective weights of the eigenmodes and they satisfy the relation $g(\omega) = \sum_\alpha g_\alpha(\omega)$. The partial density of states can be defined as [67],

$$g_\alpha(\omega) = \frac{1}{3N} \sum_{i=1}^{N_\alpha} \sum_n |e_i^n|^2 \delta(\omega - \omega_n) \tag{2.2}$$

The vibration among the various species is mostly dominated by the oxygen atoms. From Fig. 2.6 we can infer that the vibrational motion of both the atoms Si and O are mixed through the spectrum except near 766 cm^{-1}, where the vibration is dominated by the Si-atoms.

Taraskin and Elliott [72] gave a detailed analysis of the connection between the true vibrational density of states and the experimentally measured VDOS from an inelastic neutron experiment. They observed that only the effective VDOS can be measured with experimental techniques. The true VDOS and the effective VDOS are related via a correction function. Mathematically, the correction function is defined by [72],

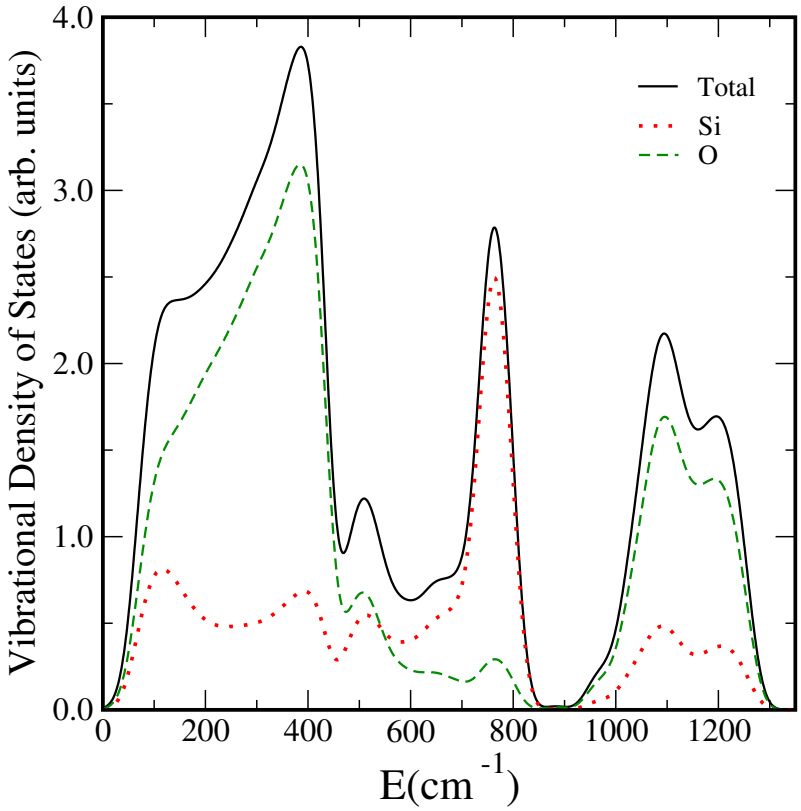

Figure 2.6: Plot of total VDOS (black, solid line), partial VDOS for Si (red, dotted line) and partial VDOS for O (green, dashed line) for 648-atom $a\text{-}SiO_2$ model.

$$C(\omega) \simeq 1 + \frac{A}{3} \sum_{\alpha} \frac{\overline{b_\alpha^2}}{m_\alpha} [\rho_\alpha(\omega_j) - \rho_\alpha^{(0)}] \tag{2.3}$$

where, A$= \frac{3<m>}{<\overline{b_\alpha^2} e^{-2\overline{W}}>}$ is a constant depending upon the scattering length , the mass of the ions and the Debye-Waller factors. Similarly, the quantities $\rho_\alpha(\omega_j) = \frac{g_\alpha(\omega_j)}{g(\omega_j)}$, $\rho_\alpha^{(0)} = \frac{N_\alpha m_\alpha}{N<m>}$, represent the relative partial VDOS and the zero-frequency partial VDOS respectively for the species α.

The true VDOS is connected to the effective VDOS by the relation [72],

$$g_{eff}(\omega) = C(\omega) g(\omega) \tag{2.4}$$

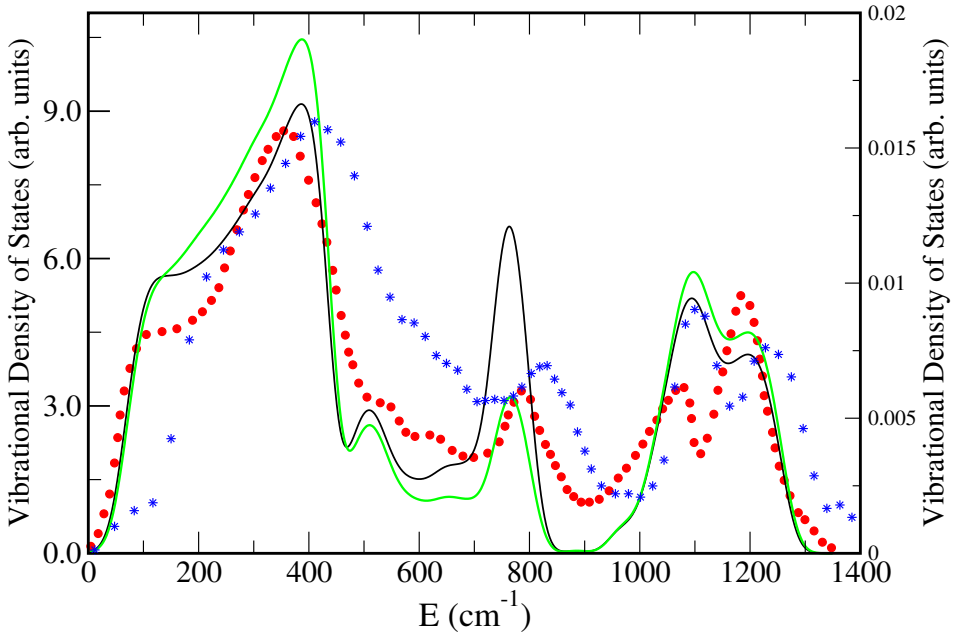

Figure 2.7: Plot of total VDOS as shown in Fig. 2.5 (black, solid line), effective VDOS obtained by Eq.(2.4) (green, solid line), experimental data (red, dots) [73] and experimental data (blue, stars) [74] for 648-atom a-SiO_2 model.

So with appropriate values of the constants and the relative partial VDOS, we evaluated the correction function and applied it to obtain the effective VDOS, which can be measured in an inelastic neutron experiment. The maximum and minimum values for the correction function were obtained as, C_{max} = 1.495 (1.48) , C_{min} = 0.435 (0.58) which were very close to the prescribed values (in brackets). Also, the normalization constant (G) for SiO_2 was obtained as 1.10 which is very close to the suggested value of (1.14). The obtained effective VDOS was plotted with a direct comparison with the reduced neutron experiments [73, 74]. The effective VDOS is shown in Fig. 2.7. The plot of the effective VDOS shows some slight variation from the uncorrected original (true VDOS). Changes are observed at the peaks 390 cm^{-1} (increased effective density) , 766 cm^{-1}

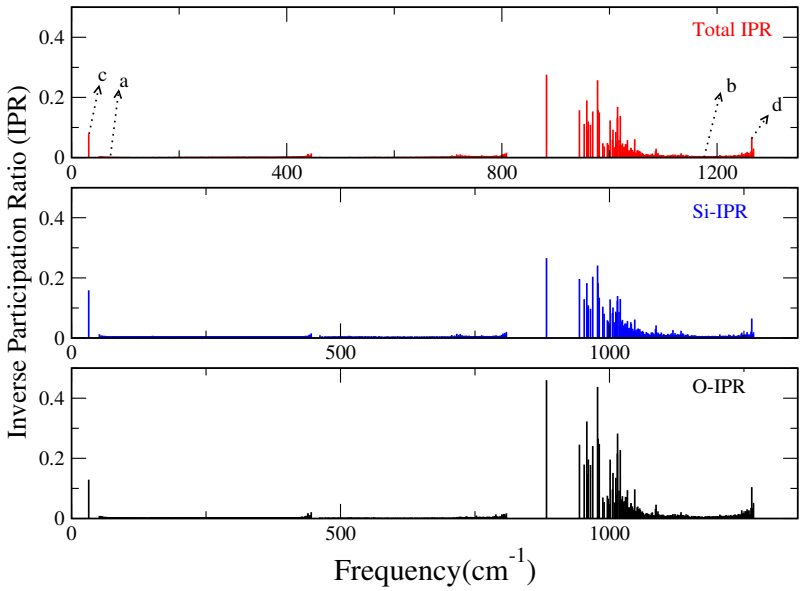

Figure 2.8: Plot of vibrational IPR: total IPR (top), Si-IPR (middle) and O-IPR (bottom) for 648-atom $a\text{-}SiO_2$ model.

(decreased effective density) and at the high frequencies 1095 cm^{-1}(increased effective density) and 1198 cm^{-1} (increased effective density).

We observe from Fig. 2.7 that the two experiments don't exactly coincide. This makes the interpretation of our computed VDOS more challenging. It is evident in the above figure that we have a general good agreement with the experiments regarding the occurrence of the major peaks in VDOS, while there are some discrepancies in weighting, between the experiment and theory.

A plot of vibrational IPR is shown in Fig. 2.8. It can be seen that the low frequency band of the vibrations is de-localized with the only localized modes occurring at the frequency 2.5 31 cm^{-1}. There is clear band gap ($\approx$ 135 cm^{-1} or 4.04 THz) excepting a heavily localized state at $\sim$ 885 cm^{-1}. As expected, these localized modes involve the motion of few atoms as opposed to the motion of nearly all the atoms in the de-localized frequencies.

The middle and bottom panels of Fig. 2.8 show, the partial or species projected vibrational localization of the two atoms. It can be asserted that the contribution of oxygen atoms is more pronounced with respect to both vibration and localization. To obtain the species-projected IPR we use the same equation (1.12) but the summation is restricted to particular atoms, in our case silicon or oxygen.

The modes were further analyzed by using visualization techniques [5] [6]. The modes were investigated using an earlier recipe [76]. In this recipe, each atom is represented with a color code on the basis of the percentage of vibration it contributes to a particular frequency mode. This is done in such a way that it includes at least 80 percent of the total vibrations in a particular mode.

Legend: *Each atom shown is labeled with different colors with respect to the fraction of total vibration: gray (*$> 1/1024$ *and* $< 1/256$*), blue (*$> /256$ *and* $< 1/64$*), red (*$> 1/64$ *and* $< 1/16$*), yellow (*$> 1/16$ *and* $< 1/4$*) and green (*$> 1/4$ *and* < 1*). The larger atom represents silicon (Si) and the smaller one denotes the oxygen (O) atoms.*

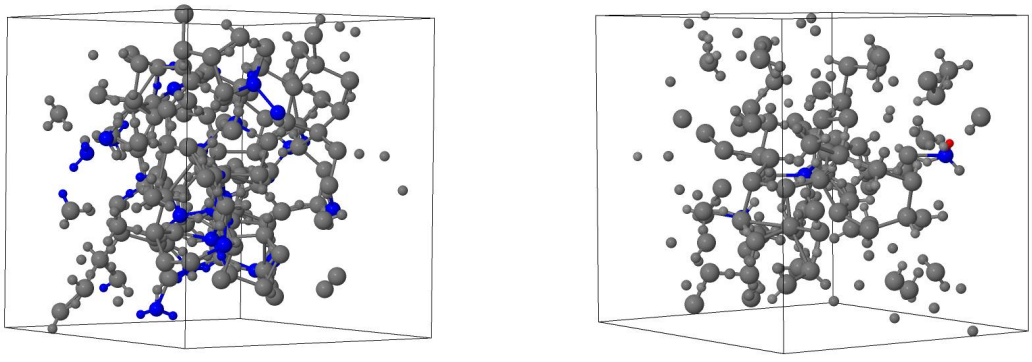

Figure 2.9: Jmol visualization of extended modes: **(Left panel)** 72.38 cm^{-1} and IPR =0.0025, **(Right panel)** 1176.38 cm^{-1} and IPR =0.0028.

[5] **Jmol**: an open-source Java viewer for chemical structures in 3D.
[6] **VMD**: a molecular visualization program [75].

In the two Figs. 2.9 (Left panel) and 2.9 (Right panel), we analyze two extended modes with comparable values of IPR. In Fig 2.9 (Left panel) the vibrations occurring at one of the low frequency mode (72.38 cm^{-1}) is shown while Fig 2.9(Right panel) gives a visual description of a high frequency mode (1176.38 cm^{-1}). The two plots resemble each other in most aspect, with the notable difference is that vibrations of silicon is more in low frequency mode (Fig. 2.9 (Left panel)) than the high frequency mode (Fig. 2.9 (Right panel)).

We also used this visualization technique to observe some of the prominent localized states, notably occurring at the frequencies 31.85 cm^{-1} and 1264.56 cm^{-1}. The localized modes exhibit few atoms vibrating in the network, with some of the atoms contributing more than the 50 percent of the vibration at a particular frequency. The localized modes occurring well inside the optical band or the high frequency region of the spectrum were throughly studied, with the intent of identifying the possible signatures of voids and to distinguish the possible pattern of vibrational localizations. These plots are shown in Fig. 2.10 (Left panel) and Fig. 2.10 (Right panel).

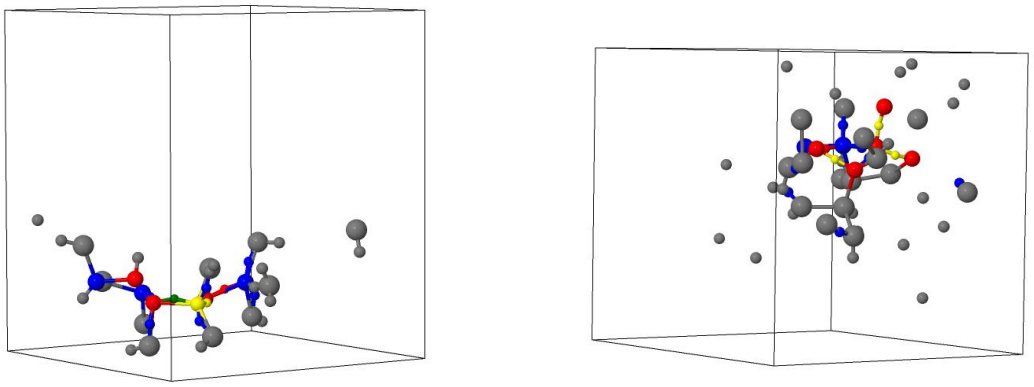

Figure 2.10: Jmol visualization of localized modes: **(Left panel)** 31.85 cm^{-1} and IPR =0.0781, **(Right panel)** 1264.56 cm^{-1} and IPR =0.0653.

Fig. 2.10 (Left panel) and Fig. 2.10 (Right panel) depicts the two localized states, one occurring at the low frequency end and the other at the high frequency part of the spectrum. The comparison of the two localized modes shows that the vibrations are not as evenly distributed as in Fig. 2.9 (Left panel) and Fig. 2.9 (Right panel), were most of the atoms had almost similar vibrational contribution.The localized state at the band gap at that frequency (882.94 cm^{-1}) (not shown) is particularly peculiar as one of the oxygen atom has more than half of the total vibrational weight.

We also used the visualization techniques to obtain snapshots of the vibrational motions at a particular frequency. These several frames of snapshots were further visualized in VMD and were studied as movies(see supplementary section [65]). We found that these states to be consistent with the bending and stretching motions assigned earlier.

2.5.1 Phase Quotient

The eigenvectors of the dynamical matrix have complete information about the atomic motions within the harmonic approximation. We can calculate the phase relationship among the neighbors of an atom by classifying whether the motion of atoms are in phase or out of phase with each other. The (*Bell and Hibbins-Butler*) [77] definition of phase quotient can be stated as [78],

$$q_j = \frac{1}{N_b} \sum_i \sum_{i'} \frac{u_i^j . u_{i'}^j}{|u_i^j| . |u_{i'}^j|} \tag{2.5}$$

where, N_b is the number of valance bonds , u_i^j and $u_{i'}^j$ are the normalized displacement vectors. In equation (2.5), i sums over all the silicon atoms and i' enumerates all the oxygen atoms which are the neighbors of the silicon atom. A complete acoustic motion will have a value of 1, while the optic like modes will attain a negative value for the phase quotient.

In Fig. 2.11 we show the plot of phase quotient (q_j). The plot shows three clear branches with an abrupt change of phase quotient at around $\sim 450\ cm^{-1}$ and the other jump at the band gap ($\sim 850\ cm^{-1}$), which indicates a different nature of optic vibrations [78, 79].

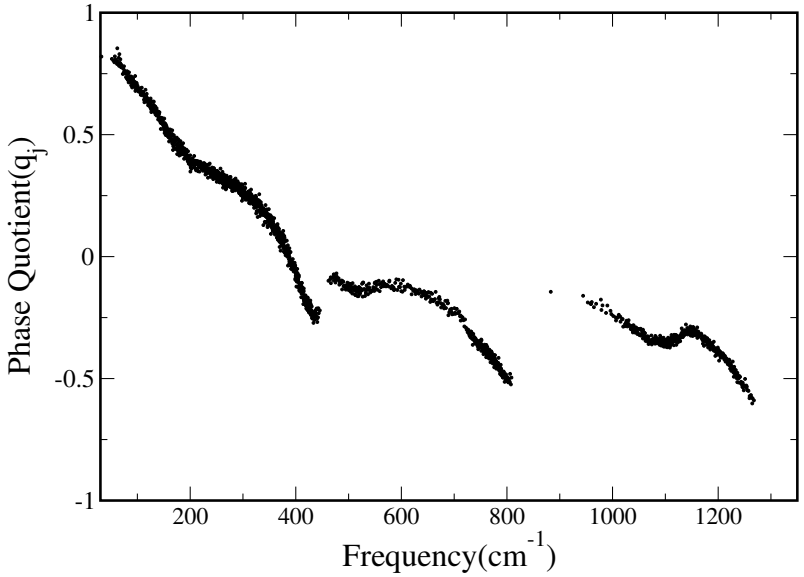

Figure 2.11: Phase Quotient (q_j) versus the frequency (ω) for 648-atom $a\text{-}SiO_2$ model.

2.5.2 Stretching-Bending Character

To further investigate the modes, we studied the stretching character of our 648-atom model. The stretching and bending character defines the extent to which a mode is stretching type or bond-bending type and it is defined as [79],

$$S(\omega_p) = \frac{\sum_m |(u_p^i - u_p^j).\hat{r_{ij}}|}{\sum_m |u_p^i - u_p^j|} \tag{2.6}$$

where, u_p^i and u_p^j are the eigen vectors of the p^{th} mode, $\hat{r_{ij}}$ is the unit vector parallel to the m^{th} bond. $S(\omega)$ is close to unity when the mode of vibration is predominantly of bond-stretching type and will be close to 0 if the mode is of a bond-bending type. The plot

of $S(\omega)$ is shown in Fig. 2.12. The plot of $S(\omega)$ can be divided in three distinct regions similar to the phase quotient. The three regions can be distinguished with a clear gap at ~ 450 cm^{-1} and ~ 850 cm^{-1}. The modes less than ~ 450 cm^{-1} shows bond-bending type of character, the regions ~ 450-850 cm^{-1} shows a mixed type of behavior and the high frequency range shows a clear stretching character. The obtained $S(\omega)$ is in a good agreement with the previous calculations [79] with a slight difference in the amplitude.

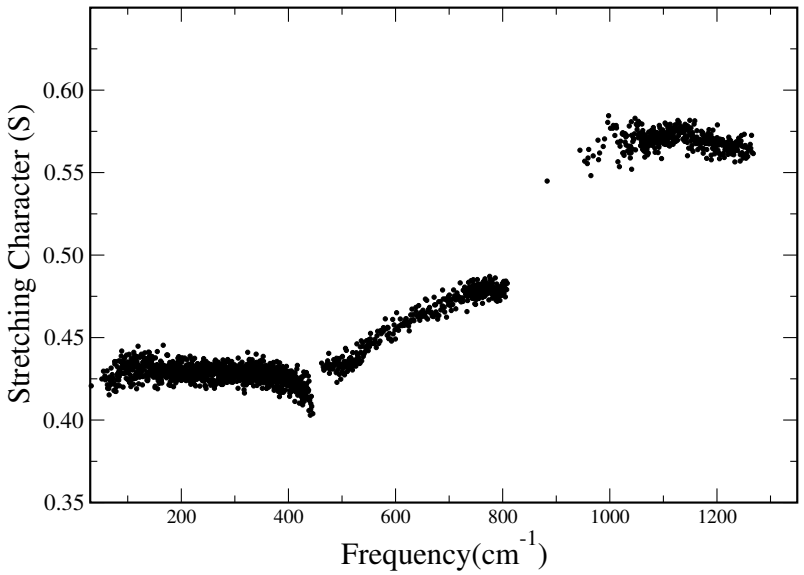

Figure 2.12: Stretching character ($S(\omega)$) versus the frequency(ω) for 648-atom a-SiO_2 model. The small values of (S) is bond-bending, large values corresponds to optical streching modes.

2.5.3 Specific Heat and The Boson Peak

In Fig. 2.13 we can see that the obtained plot of $C_V(T)/T^3$ with our 648-atom a-SiO_2 model is in reasonable agreement with the experimental findings. It is to be noted that our peak is little shifted to the right and has somewhat reduced amplitude. But, our results are substantially improved over the previous simulation results of *Taraskin and*

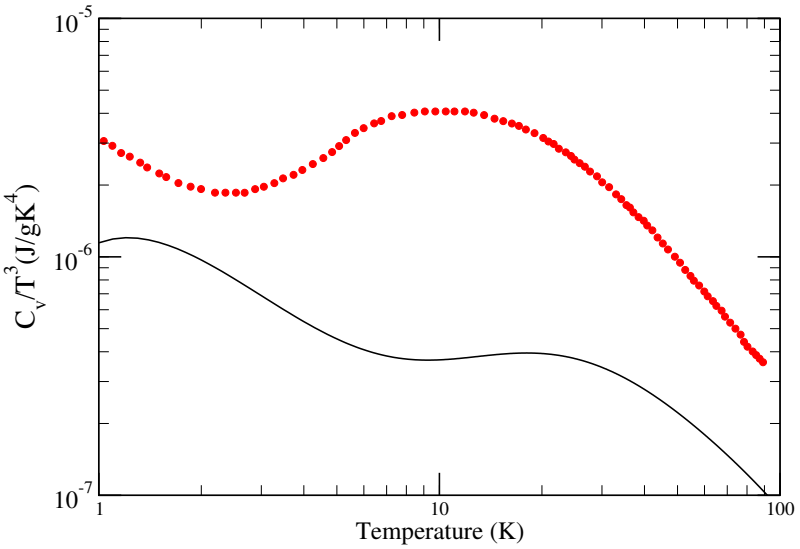

Figure 2.13: Low temperature dependence $C(T)/T^3$: our model (black, solid line), expt.(red, dotted line) [80].

Elliott [78] using the Van Beest potential [81]. A similar calculation was done by *Horbach et. al* [82] using 8016 ions with a larger box size but the results do not reproduce the $C_V(T)/T^3$ curve.

The authors [78, 82] have assigned this discrepancy in the plot of $C_V(T)/T^3$ to finite size effects and the cooling rates of their samples [82]. But, our calculation with the same number of atoms (648) as *Taraskin and Elliott* produced more better result. The calculation of *Horbach et. al* with a larger cell does not improve the results significantly. Thus, we can infer that the discrepancy between the theory and the experimental calculation is due to inter-atomic interactions. An *ab initio* potential is required to qualitatively reproduce $C_V(T)$ for small T.

The $C_V(T)/T^3$ curve has a noticeable plateau at a temperature $\sim 20K$. The acoustic modes in the vibrational density of states (VDOS) has a Debye ($\sim \omega^2$) spectrum. In the Debye spectrum an additional peak seen in the region $30 - 120\ cm^{-1}$, usually referred as

"*Boson peak*". We calculated the specific heat by excluding the frequencies lying in the region of "*Boson peak*"and notable changes were observed at the plateau of the $C_V(T)/T^3$ graph around the region (20 K). We have illustrated these modes in Fig. 2.14. A representative example in this frequency range is the extended transverse mode of Fig. 2.9. It has been shown that the Boson peak satisfies the *Ioffe-Regel* criterion [83], which is the reason many authors have proposed this to be a hybridized state of the acoustic band and the optic band. In agreement with *Taraskin and Elliott* we note that these are transverse-bond bending rather than stretching excitations.

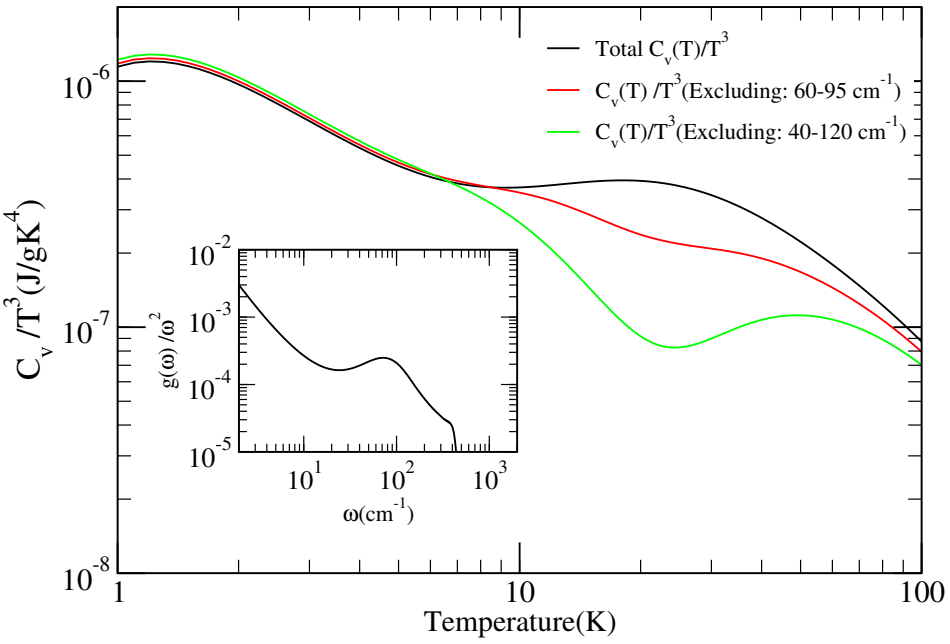

Figure 2.14: Low temperature dependence $C(T)/T^3$: Black (total), Red (excluding the frequency range: 60-95 cm^{-1}), Green (excluding the frequency range: 40-120 cm^{-1}). Inset: Plot of $g(\omega)/\omega^2$ versus the frequency.

2.6 Conclusion

We found that our model of 648-atom *a-SiO*$_2$ reproduces most of the known experimental properties while improving on some earlier calculations. The structure of our 648-atom *a-SiO*$_2$ model is in good agreement with the experimental results as obtained from the experimental techniques of diffraction and inelastic neutron scattering, and is "fully first principles" in the sense that the supercell geometry is optimized to minimize the total energy for the Hamiltonian we employ. The vibrational properties were analyzed with the help of eigenfrequencies and eigenvectors, obtained by diagonalizing the dynamical matrix. The VDOS obtained with our method showed a good agreement with the experimental data. It was able to produce all the principal peaks obtained in the experimental measurements on amorphous *a-SiO*$_2$. In addition to the principal peaks, there was a peak observed at the frequency $\sim$ 495-507 cm^{-1} in both the 192-atom [22] and the current 648-atom model.

The localization of vibrational modes was also studied through the evaluation of inverse participation ratio (IPR) and with the help of the visualization techniques. We found that these modes were consistent with the different types of motion (rocking, bending, etc.) previously assigned by different authors [15, 78]. A through analysis of the localization was done by using visualization techniques including animations in the Supplementary Material (see Ref. [65] supplementary materials). In addition, we were able to make an improved prediction for the low temperature specific heat compared to previous work [78, 82]. We were also able to verify that plateau observed ($\sim 20K$) in the plot of specific heat ($C(T)/T^3$) was due to the "*Boson peak*"seen in the VDOS. We provide some evidence that the modes associated with Boson peak may be computed and analyzed in simulation.

In conclusion, we found that our 648-atom model have improved the understanding of *a-SiO*$_2$ while describing the structural, electronic and vibrational properties and

clarifying the importance of interatomic potential and model size on vibrational quantities. Additionally, we have successfully studied vibrational study of bilayer silica for a bigger system (1200 atoms) using same recipe [84].

3 *Ab initio* Simulation of Low Density Amorphous Carbon

The work presented in this chapter has been published as B. Bhattarai, D.A. Drabold, Amorphous carbon at low densities: an ab initio study, *Carbon*, 115 (2017), 532-538.

3.1 Motivation

Amorphous carbon has been an important research topic both for its many technological applications, and its scientific interest due to its remarkable ability to form an array of microstructures. Carbon forms bonds of sp, sp^2 and sp^3 type [85], and these tend to be surprisingly energy-degenerate. An interesting question we will explore is the concentration of these three types of bonds as a function of density. Experimentally, non-hydrogenated amorphous carbons are challenging [86], which further justifies a new theoretical study. The variation in low density carbon samples arise in part from the method of preparation of the sample and heat-treatment [87]. Furthermore, glassy carbon may be extracted from various polymers, which may leave a residue of bonded H. The presence of hydrogen significantly impacts the inelastic neutron scattering spectrum [88].

In this chapter, we present new models for low density carbon. We have used state of the art *ab initio* interactions for our calculations. This approach provides a benchmark, as we obtain atomistic models without any *a priori* assumptions of the system and accurate interatomic forces. Further, this work will be an extension of the previous *ab initio* method based theoretical work done for higher densities of amorphous carbon [89].

3.2 Computational Methodology

We have prepared models of glassy carbon [90] with densities ranging from (0.923 g/cm^3 - 1.6 g/cm^3). These models were prepared by using *ab initio* Package "Vienna *Ab initio* Simulation Package "(**VASP**), a molecular dynamics package with a plane-wave basis and using the local-density approximation. The electron-ion interactions for the

plane wave basis or VASP models were described by the Projector Augmented-Wave (PAW) method [39, 40] with *Ceperley-Alder* exchange correlation functional. A liquid phase at each density was equilibrated and then "cooled" as described below yielding an arrested solid phase, which was then fully relaxed using the conjugate gradient (CG) method. All simulations were performed at constant volume, employing only the $\Gamma(\vec{k} = 0)$ point to compute the forces and total energies.

3.3 Models

Table 3.1: Nomenclature and details of our models: density of the models (ρ), position of first (r_1) and second (r_2) peak of RDF, Mean co-ordination number (n), percentage of sp^3, sp^2 and sp, cooling time/cooling rate (*refers to cooling time or cooling rate from 8000 K to 600 K.*) and Free energy per atom of the relaxed models(E_0) (*after substraction from lowest value of* E_0.).

Model	$\rho(g/cm^3)$	r_1(Å)	r_2(Å)	n	% of sp^3	% of sp^2	% of sp	cooling time(ps)/rate(K/ps)	$E_0(eV/atom)$
c64_4ps	1.50	1.43	2.45	2.90	6.25	78.12	15.63	4.0/ 1850.0	0.13
c120_15ps	1.50	1.45	2.49	2.90	4.17	81.67	14.16	15.0/ 493.3	0.15
c120_20ps	1.50	1.44	2.48	2.93	9.17	75.00	15.83	20.0/ 370.0	0.11
c72_16ps	0.92	1.41	2.48	2.67	0.00	66.67	33.33	16.0/ 462.5	0.35
c72_20ps	1.40	1.43	2.46	2.89	7.00	75.00	18.00	20.0/ 370.0	0.00
c72_20ps†	1.60	1.43	2.47	2.86	4.17	77.78	18.05	20.0/ 370.0	0.02

We have prepared models with system size ranging from 64 atoms to 120 atoms [7]. We have chosen densities varying between 0.923 g/cm^3 - 1.6 g/cm^3. We began with random coordinates, these were "heated" to 8000 K, equilibrated at 8000 K and then

[7] We also prepared a larger model (with 216 atoms) using SIESTA [36], with (*Harris Functional*). The non-self consistent scheme resulted in slighty larger fraction of sp^3 and a minor shift in RDF was observed, with almost no change in other properties.

cooled to 300 K in multiple steps. Finally, a well-equilibrated model at 300 K was relaxed using the conjugate gradient (CG) scheme.

The resulting six models provide us with a reasonable selection of low density regime in amorphous carbon. These models will hereafter be identified as c64_4ps, c120_15ps, c120_20ps, c72_16ps, c72_20ps and c72_20ps†. These assigned nomenclatures indicate : the number of atoms in the cell, and the cooling time used for each model. We have summarize our models in Table. 3.1.

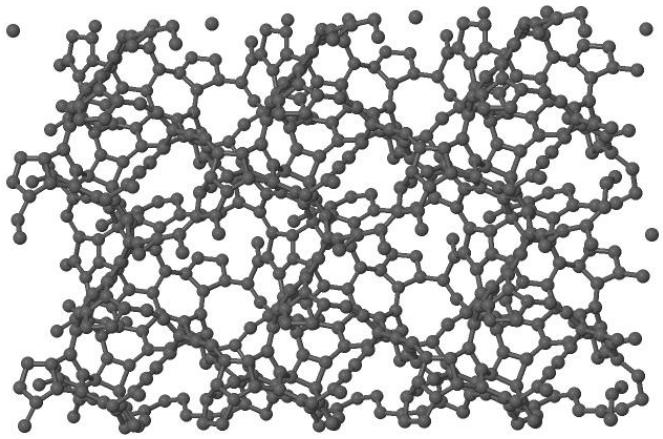

Figure 3.1: Visualization of model c120_15ps, 720 atoms are shown (*replicated by using periodic boundary condition).*

3.4 Structural Properties

A visual representation of these models has been provided in Fig. 3.1 and Fig. 3.2. We have used periodic boundary conditions to replicate the c120_15ps model and show 720 atoms in Fig. 3.1. Meanwhile, in Fig. 3.2, the various bonding environments have been assigned different colors. This reveals that sp^3 bonding mainly inter-connects the sp^2 bonding networks and that sp^2 bonding dominates for lower density. Interestingly, a

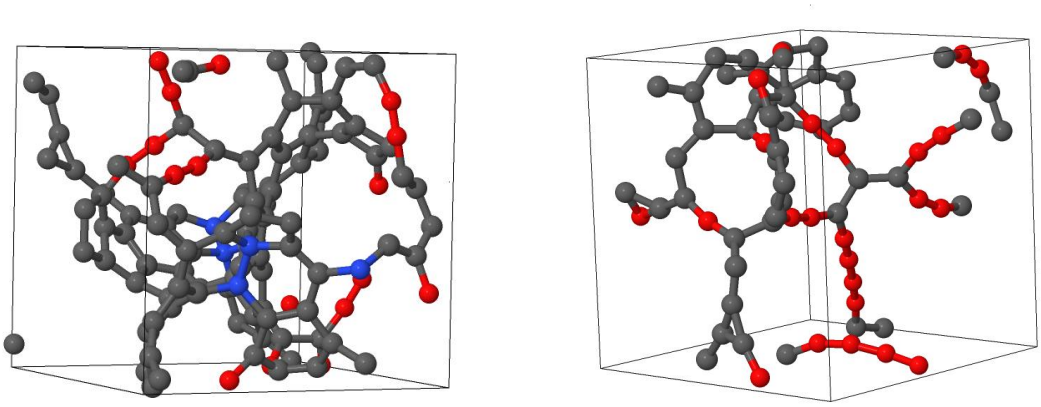

Figure 3.2: Visualization of the different bonding: grey(sp^2), blue(sp^3) and red(sp). **(Left panel):** c120_15ps , $\rho = 1.50 g/cm^3$ and **(Right panel):** c72_16ps , $\rho = 0.923 g/cm^3$, *Periodic boundary condition were used, only atoms in reference cell are shown.*

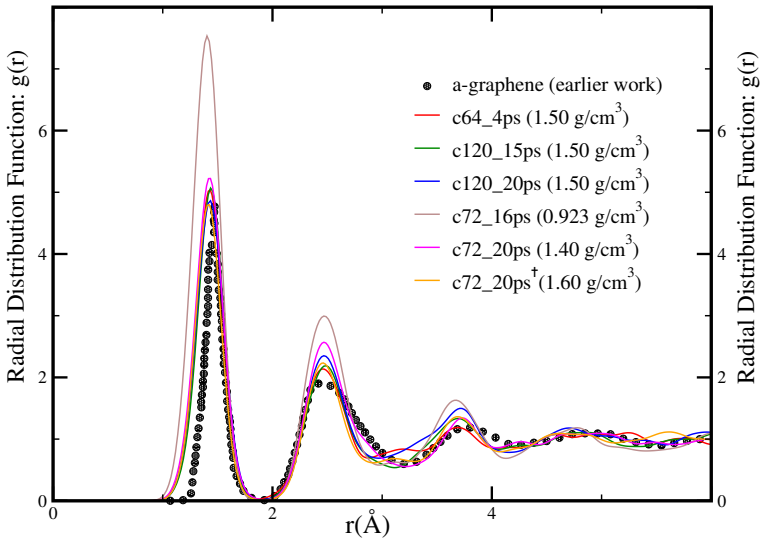

Figure 3.3: Radial distribution function of different models for low density amorphous carbon (solid lines) and comparison with the amorphous graphene [24].

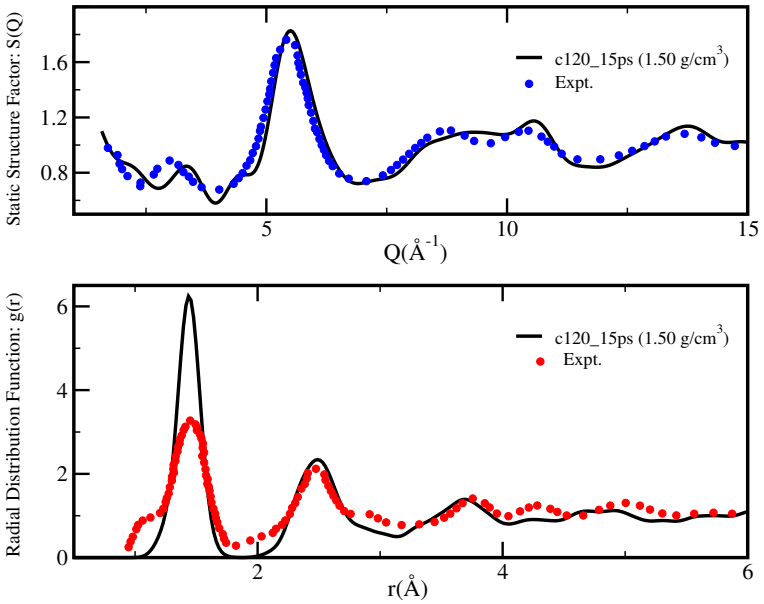

Figure 3.4: Static structure factor for the model **c120_15ps** (black, solid line) versus experimental structural factor data of amorphous carbon ($\rho = 2.0 g/cm^3$) [91] (blue, solid circles), (bottom) RDF for the model **c120_15ps** (black, solid line) versus experimental RDF for density ($\rho = 1.55 g/cm^3$) [92].

significant fraction of *sp* bonded atoms are also formed in low density carbon, providing a chain-like topology, familiar from a-Se [93]. In particular, our model (c72_16ps) at a density of 0.923 g/cm^3 has 33% *sp* bonded atoms. To our surprise this model has the same final free energy per atom (E_0), as the other model with much less *sp* content, which suggests that at low concentration the *sp* bonding is expected [94] and justifies the common assertion that the three hybridizations yield similar local energetics. The *sp* bonded model is shown in Fig. 3.2 . These *sp* chains were first conjectured in the work of *McCulloch et. al* [89], we show that their conclusions were valid. We have also compared our results (see Fig. 3.3) with the amorphous graphene network [24]. To our surprise, despite the fact that our amorphous carbon is three dimensional in nature (see Fig. 3.1),

structurally it resembles strictly the two dimensional amorphous graphene (albeit puckered around pentagonal structures) [95].

The structure of low density carbon has been controversial as different heat treatment protocols yields different structural features [92]. Further, there has also been a debate about the bonding present in these structures. *Mildner and Carpenter* [87] suggested that the concentration of sp^3 bonding in these materials is less than 10 %. Our models are in agreement with this claim, as all of our models have sp^3 fraction below 10 %.

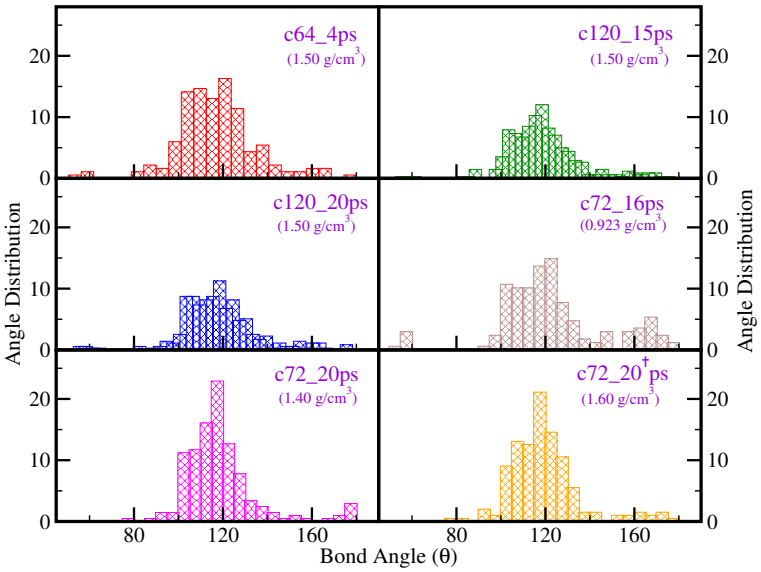

Figure 3.5: Bond-angle distribution function of low density amorphous carbon models.

Structurally, glassy carbon can be described with the help of the Static Structure Factor in reciprocal space or its real space counterpart the Radial Distribution function (RDF). The RDF obtained for the models are plotted in Fig. 3.3 and also for a model of amorphous graphene. The position of the first and second peak from the RDF is similar for the different models irrespective of the different carbon bonding environments and the method used for making the models. The peak positions and the coordination number are in good agreement with previous calculations[92, 96, 97] and with experiment [87].

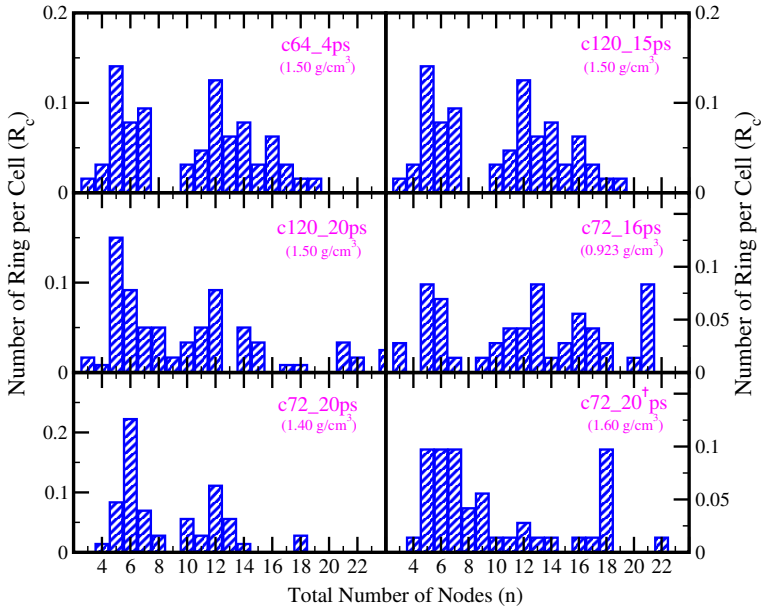

Figure 3.6: Ring distribution of low density amorphous carbon models [54, 56].

Comparison of experiment and theory for the structure factor and the radial distribution function (RDF) are given in Fig. 3.4. Firstly, we compare the obtained structure factor with the experimental data for amorphous carbon at a density ($\rho = 2.0 g/cm^3$) [91]. Similarly, Fig. 3.4 shows another comparison of experimental data obtained for the glassy carbon at a density ($\rho = 1.55 g/cm^3$) [92], with the radial distribution function. Experimentally, the first three peaks of the RDF for glassy carbon are at distances, 1.42 $\AA$, 2,46 $\AA$ and 3.75 $\AA$. There is pleasing agreement with these observations. Additionally, there are peaks or shoulders occurring at distances, 2.84 $\AA$, 4.27 $\AA$ and so on [87, 92, 98]. As seen in Fig. 3.4, there is a narrow shoulder at distance (~ 1.10 $\AA$) in the experimental RDF [92] and it is also seen in the TBMD simulation [96] (*especially for the low density models*). This narrow shoulder is not seen in our models. From Table. 3.1, it should be noted that different cooling temperatures for the simulation

results in slight difference in the fraction of (sp^2, sp^3 and sp) bonds with little or no effect on the RDF and peak positions.

The coordination numbers (listed in Table 3.1), are dominated by trigonal for low density carbons. This indicates that the carbon-carbon angle distribution is likely to peak near 120^o. Several models and experiments indicate a slightly different value of the bond angles for these carbon. *Beeman et. al.* [97] calculated the angle distribution for classic handmade models and found these angles slightly less than expected $\sim 117.7^o$ for the three coordinated models.

The angle distribution functions for the models are plotted in Fig. 3.5. The peaks are in harmony with our assumptions except for the model c72_16ps. In this model the presence of a high percentage of sp bonds results in a broader distribution of the peaks. Further, a tiny (and probably physically meaningless) fraction of bond angles are seen at $\sim 50^o$.

The ring distribution provides us with more information about the connectivity of the networks. The ring statistics are shown in Fig. 3.6 and were obtained by King's shortest path [54] scheme, using the ISAACS [56] program. The ring statistics thus obtained have a broad distribution of with the maximum of most models peaking at 5-membered-rings as opposed to 6-membered-rings for graphite [89]. The results of ring statistics obtained here (albeit with inter connecting sp-chains) are consistent with the previous results [89, 92]. The connectivity of the high sp model c72_16ps has a slight different characteristics as, a few rings are observed with high number of nodes.

3.5 Vibrational Properties

The dynamical matrix was obtained by displacing each atom in 6-directions ($\pm x$,$\pm y$,$\pm z$) by a small displacement of 0.015 $\AA$. Then, *ab initio* force calculations were performed to obtain the force constant matrix. The details of the force constant matrix

calculation is provided elsewhere [65]. We have Gaussian broadened the eigenvalues (using a width $\sigma \sim 3.0$ meV) to obtain the VDOS. The first three $\omega = 0$ frequencies (arising from rigid cell translations) have been ignored for both the VDOS and the vibrational IPR.

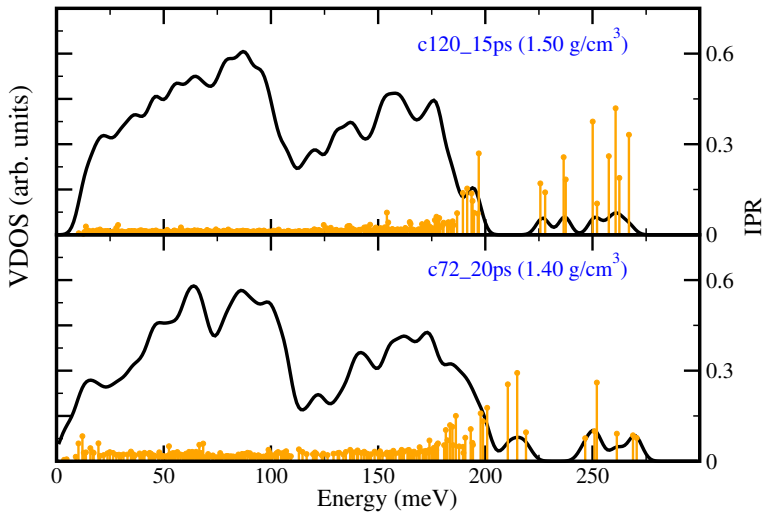

Figure 3.7: Vibrational Density of States (VDOS) at densities 1.50 g/cm^3 and 1.40 g/cm^3 (black, solid line), The Inverse Participation Ratio (IPR) describes the localization of the modes (orange, drop lines).

Although we obtained the VDOS for the six models only four VDOS is plotted in Fig. 3.7 and 3.8. The other two VDOS for models (c64_4ps and c120_20ps) at density $1.50 g/cm^3$ are very similar to model c120_15ps with density $1.50 g/cm^3$. In spite of their differences, the VDOS obtained have a similar character for example, models below ($\sim$ 200 meV) are well extended modes. Further, despite the fact that the densities of these four models vary from 1.6 g/cm^3 to 0.923 g/cm^3, we didn't obtain any low energy localized modes as seen in calculations with voids for a-Si [76]. Additionally, we show a comparison of the plot between the VDOS obtained for a-graphene [95] and our model (c72_20ps, $1.40 g/cm^3$) in Fig. 3.9. The plots have bear considerable similarity, excepting

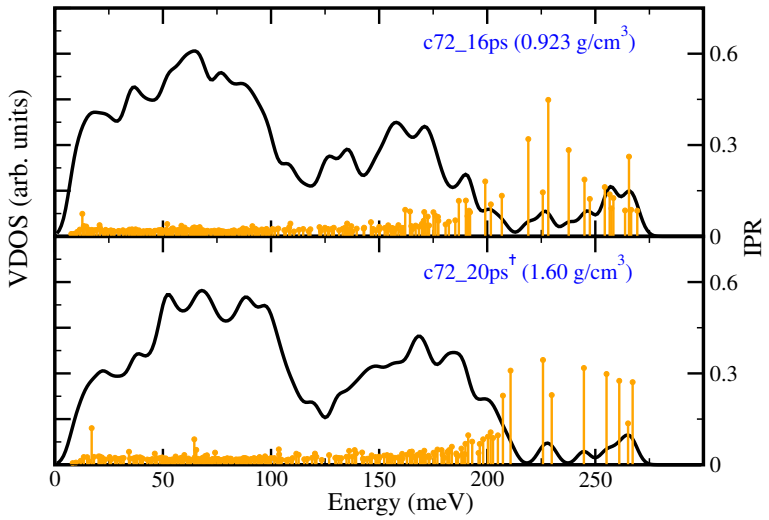

Figure 3.8: Vibrational Density of States (VDOS) at densities 0.923 g/cm^3 and 1.60 g/cm^3 (black, solid line), The Inverse Participation Ratio (IPR) describes the localization of the modes (orange, drop lines).

an intense peak near 80 meV. The band between about 110 meV-200 meV is strikingly similar for amorphous graphene and our 1.40 g/cm^3 model. The intense peak could perhaps be used as a diagnostic for the presence of amorphous graphene.

In our previous calculations [65], we presented the details for computing the species-projected VDOS. Here, we computed the VDOS contributions due to the different bonding($sp - sp^2 - sp^3$) for the 4 models with different densities. This projection gives further insight to the different contribution to the vibration among the bonding units. These projected VDOS are plotted in Fig. 3.10 and 3.11. As expected, the sp^2 contribution to the VDOS is the most significant [99], and makes contributions to all the major peaks in the VDOS. The sp^3 and sp contributions largely perturb the peaks originating primarily from the sp^2-associated modes. At higher energy ($\sim$ 200 meV or more), the contributions are mostly from sp and sp^2 modes, as one might expect from the strength of these carbon bonds.

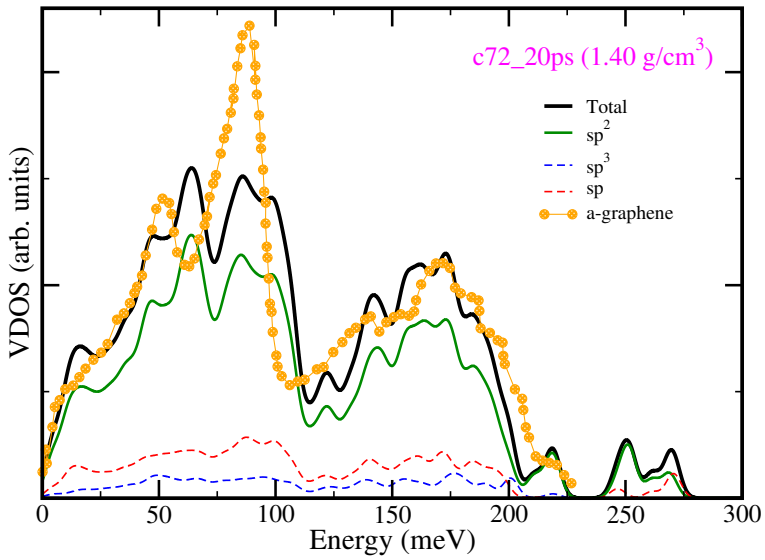

Figure 3.9: Vibrational density of states of model (c72_20ps, $1.40 g/cm^3$) compared with amorphous graphene [95].

We have also compared with the experimental results of *Kamitakahara et al.* [100] for the glassy carbon (see Fig. 3.10 and 3.11). We observe qualitative agreement with the experimental results. Our VDOS matches the experimental results at the lower energy regime (~ 50 meV), while some discrepancies are is seen at higher frequencies. We have previously shown [65] in our work on $a\text{-}SiO_2$, that an accurate potential and the system size greatly affects the VDOS to obtain well defined resolution of the notable peaks.

We also investigate the contribution to the localization due to each type of bonding environments with our system. It is not surprising to see that the most localized modes arise from sp and sp^3 bonding. The results of the projected IPR is presented in Fig. 3.12. Where, the model with the least sp^3 bonding [present in an amount of (< 10 %)] has the most localized modes. Meanwhile, sp bonding yields fairly extended modes for the lower regime (< 200 meV), while there are few significant localized modes on the optical

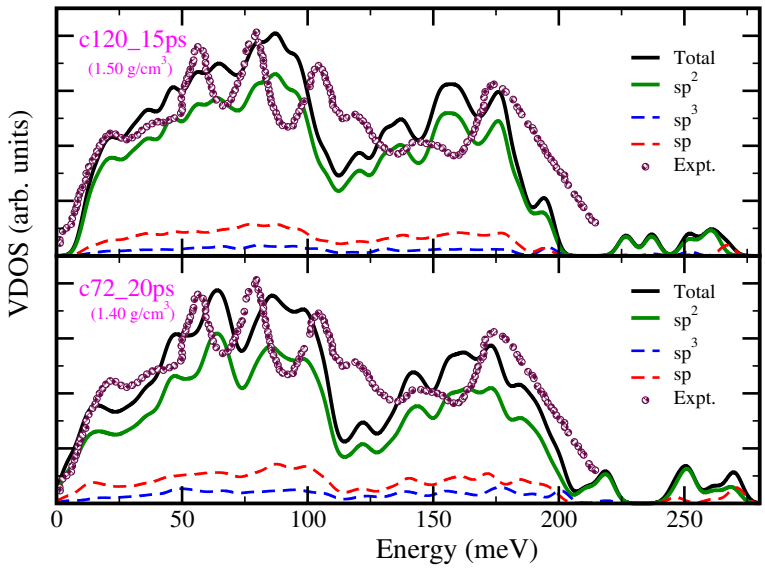

Figure 3.10: Plot showing Total VDOS, (sp^3, sp^2, sp) projected VDOS and the experimental results [100] for glassy carbon.

regime. This also suggests that a few percent of sp modes in these low density carbons are expected.

In Fig. 3.13, we see that $C_V(T)$ for our four models is in reasonable agreement with experiment. Glassy carbon has a higher value of specific heat and lower density than graphite [101]. These facts are manifested by our models. Inferring from Fig. 3.13, the model (c72_16ps) (Fig. 3.13) which has the lowest densities (0.923 g/cm^3) among the models has a higher value of specific heat compared to the other models.

Similar to the ($sp - sp^2 - sp^3$) projected VDOS, we have computed the specific heat due to partial contribution of different bonding environments. The results due to this decomposition leads to an interesting result. We observe that the contribution due to the partial-sp^2 VDOS in the low temperature specific heat matches quite well with the experimental result [101]. It must be noted that the sp bonding has a significant effect on the total specific heat obtained for the models, while the contributions from the sp^3

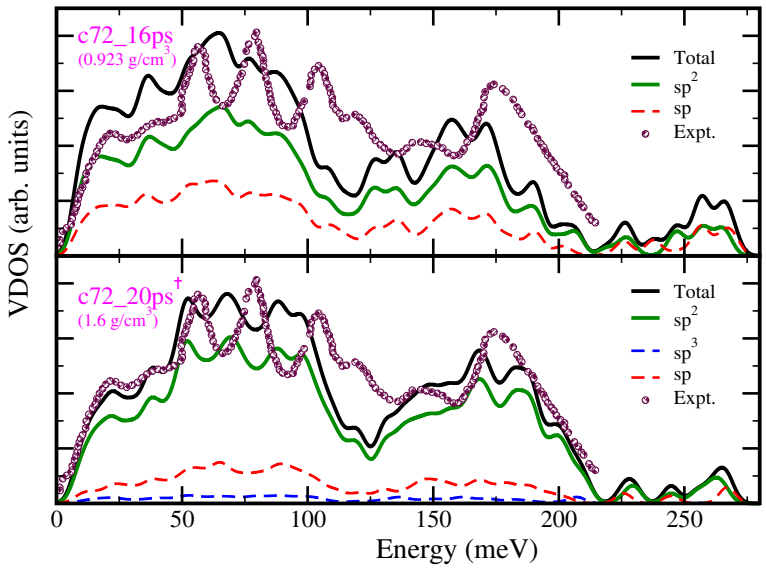

Figure 3.11: Plot showing Total VDOS, (sp^3, sp^2, sp) projected VDOS and the experimental results [100] for glassy carbon.

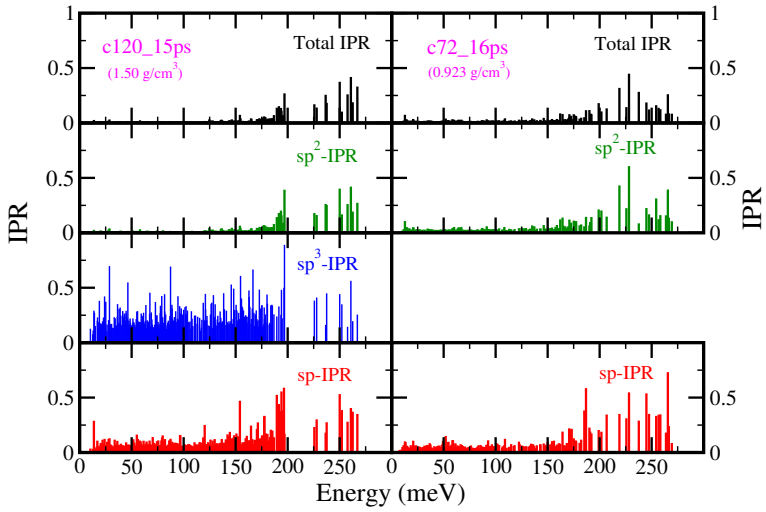

Figure 3.12: Plot of (sp^3, sp^2, sp) projected IPR along with the total IPR for the obtained models.

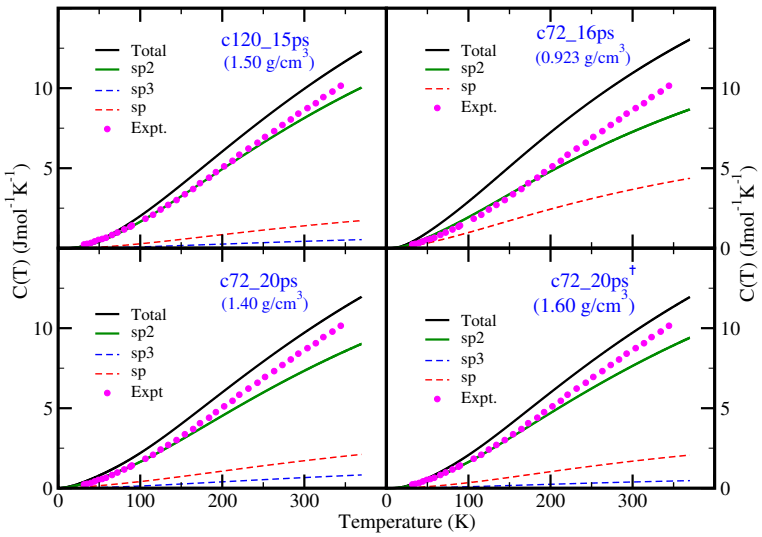

Figure 3.13: Low temperature dependence of specific heat for the four models versus the experimental results [101].

bonding remains minimal. We have also verified the "3R-limit" (Dulong-Petit) limit at high temperature for our models (not shown here)[8].

3.6 Electronic Properties

The concentration of sp, sp^2 and sp^3 states is determined by the density [89]. The electronic density of states (EDOS) is strongly impacted by these different electronic hybridizations. The EDOS plot of one representive model in shown in Fig. 3.14. Our EDOS is in agreement with earlier research [89, 102]. In Fig. 3.14, we show that the p-orbital contribution is more significant near the conduction edge. The electronic localization (IPR) [103] shows that at these lower densities these amorphous carbon are conductive (with a large density of extended states near the Fermi level) as expected [89]. This pattern of EDOS is consistent through out our other models without any significant

[8] To the extent that the hybridization-projected specific heat functions are well defined and distinct, it may prove possible to use the temperature depen- dence of the specific heat to estimate the concentrations of the sp, sp2, and sp3 concentrations in a sample. More work is needed to see if this could be practical.

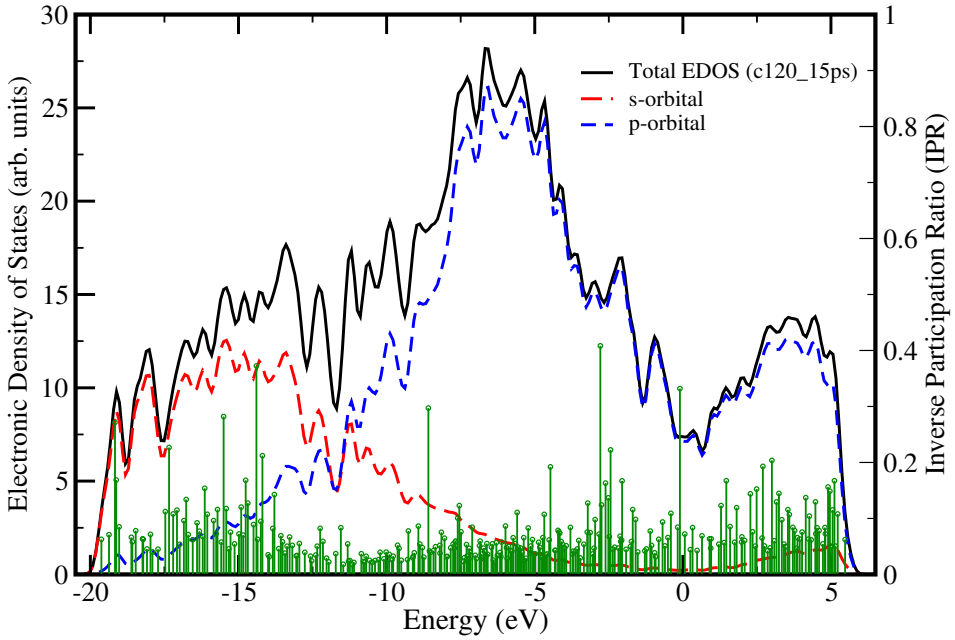

Figure 3.14: Plot of EDOS (E_F=0) for the c120-a model: (black, total EDOS), (red-dashed, s-orbital EDOS), (blue-dashed, p-orbital EDOS), the localization (green-drop lines, IPR).

differences, other than different weightings arising from the various hybridizations present for different densities.

3.7 Conclusion

We found that our *ab initio* based models reproduce most of the properties of the low density amorphous carbon, while improving upon some of the previous calculations and drawing comparisons to amorphous graphene. At these low densities, amorphous carbon consists of a mixed network involving sp^2, sp^3 bonds as expected and at the lowest densities a non-negligible contribution from sp bonds.

We have predicted that the vibrational contribution of the sp^2 bonding is the most significant and it governs the total vibrations in these materials. Further, we also show that these sp^2 guided vibrations are extended and evenly distributed. We note that the

vibrational modes are more complex and non-local than simple molecular models would suggest. While such models certainly capture some of the basic character of the vibrations, the real modes are delocalized and sometimes mix with other nearly resonant modes. We believe that there is both scientific and pedagogic values in the animations that we provide from this work. We also note similarities and differences between a-C and hypothetical amorphous graphene materials.

4 *Ab initio* Inverse Modeling of Large and Realistic Amorphous Systems

The work presented in this chapter has been published as B. Bhattarai, D.A. Drabold, Evolution of amorphous carbon across densities: An inferential study, *Carbon*, 131 (2018), 168-174 and B. Bhattarai, P. Biswas, R. Atta-Fynn and D. A. Drabold, Amorphous graphene: a constituent part of low density amorphous carbon, *Physical Chemistry Chemical Physics* 20 (2018), 19546-19551.

4.1 Motivation

Amorphous carbon (*a-C*) exists with various bonding environments (sp, sp^2 and sp^3) depending upon the sample density. A lack of long-range order, different bonding environments and presence of porosity in a-Carbon, imposes a challenge for condensed matter theorists [8]. The usual method of "*melt and quench*" (MQ) has several limitations. In particular, *a-C* empirical potentials are difficult to model as they exist with different bonding environment (sp, sp^2 and sp^3) as a degenerate state. It is really challenging to have a common potential which could differentiate between different topologies [4]. It has been shown that incoherent concentration of sp, sp^2 and sp^3 is obtained from simulation using different empirical interactions under same condition [6]. Meanwhile, accurate *ab initio* methods have fast quench rate and are limited to few hundred atoms. We bridge the divide between these approaches in this work.

In first section of this chapter, we present a series of large models (648 atom) of amorphous carbon at various densities using a uniform approach (FEAR) for all. We systematically report the dependence of observables on the density. In second section, we apply FEAR method to invert diffraction data for nano-porous carbon and infer that these nano-porous carbon are indeed amorphous graphene. To infer this conclusion, we

compare and contrast obtained FEAR model with sp^2 bonded structures namely: 2-dimensional amorphous graphene, crystalline graphene and schwarzite structures. We calculate several observables to support our claim that these low density amorphous carbon are indeed amorphous graphene.

4.2 Amorphous Carbon Across Densities

4.2.1 Introduction

We have implemented Force Enhanced Atomic Refinement (**FEAR**) [2, 3, 48] method in a-Carbon. FEAR offers the logical advantage of using *a priori* knowledge, but within an *ab initio* simulation framework. Its ability to predict accurate structure with correct chemical composition, starting from a *random* structure without any constraint has been a important feature of this approach. We have used FEAR with state of the art *ab initio* interaction for our calculations. We present a series of models of amorphous Carbon at various densities using the same approach for all. We systematically report the dependence of observables on the density.

4.2.2 Models and Methodology

We have prepared four models of a-Carbon with 648 atoms at densities 3.50 g/cm^3, 2.99 g/cm^3, 2.44 g/cm^3 and 0.951 g/cm^3 using FEAR (see Fig. 4.1). In FEAR, we begin with *randomly* chosen coordinates which are subjected to partial structural refinement with M accepted RMC steps and partial relaxations with the conjugate gradient (CG) method for N relaxation steps[9]. This cycle is repeated until the model is fully converged (fitting the data and at the same time, sitting at a suitable minimum of the DFT interactions) [2, 3]. To our knowledge, these are the largest *ab initio* models offered to date for a-Carbon.

[9] (M/N) are chosen with a ratio 0.01, with M=100 and N=1 for this work [48]

The relaxation step was performed with a single-ζ basis, periodic boundary conditions and Harris functional at constant volume using **SIESTA**[10]. As an additional check of our models, we have relaxed the converged models using the *ab initio* package **VASP** with plane wave basis [39] $\Gamma(\vec{k} = 0)$, plane-wave cutoff of 400 eV and an energy convergence tolerance of 10^{-4} eV. To compare and contrast, we have also prepared *ab initio* based MQ models. We have prepared three models (160 atom) each using SIESTA (LDA, Harris functional) and VASP (LDA, self-consistency).

The starting random configuration is fitted to appropriate experimental data with **RMCProfile**[11]. After every ~100 accepted RMC moves [2, 3, 48], the total energy and forces were evaluated (using a single force call) and the atoms were moved along the gradient to reduce the total energy. We have chosen a maximum RMC step size of 0.25$\mathring{A}$-0.375$\mathring{A}$, a minimum approach of 1.05$\mathring{A}$-1.20 $\mathring{A}$, with a fixed spacing of 0.02 $\mathring{A}$ and $0.04 - 0.085$ weight of the experimental data. Meanwhile, CG relaxation is carried out using SIESTA.

In the meantime, we implemented MQ calculations with random coordinates, which were equilibrated at 7000 K, then cooled to 300 K, further equilibrated at 300 K and finally relaxed using CG method. This process employed a time step of 1.0 fs for a total simulation time of 26 ps. We have also prepared a self-consistent MQ model using VASP. These models were started from random, then heated to 8000 K, equilibrated at 8000 K, cooled to 300 K and finally relaxed with CG method. A time step of 1.5 fs was used for total time of 24 ps.

These models will hereafter be identified as (**F648, S160 and V160**). The assigned nomenclature indicates: method of preparation (FEAR-SIESTA-VASP) and number of atoms in the cell of each model. We have used our previous VASP prepared model (V72 at

[10] A local-orbital density functional code using LDA with Ceperley-Alder exchange correlation [36]
[11] RMC based applications for the structural refinement [104]

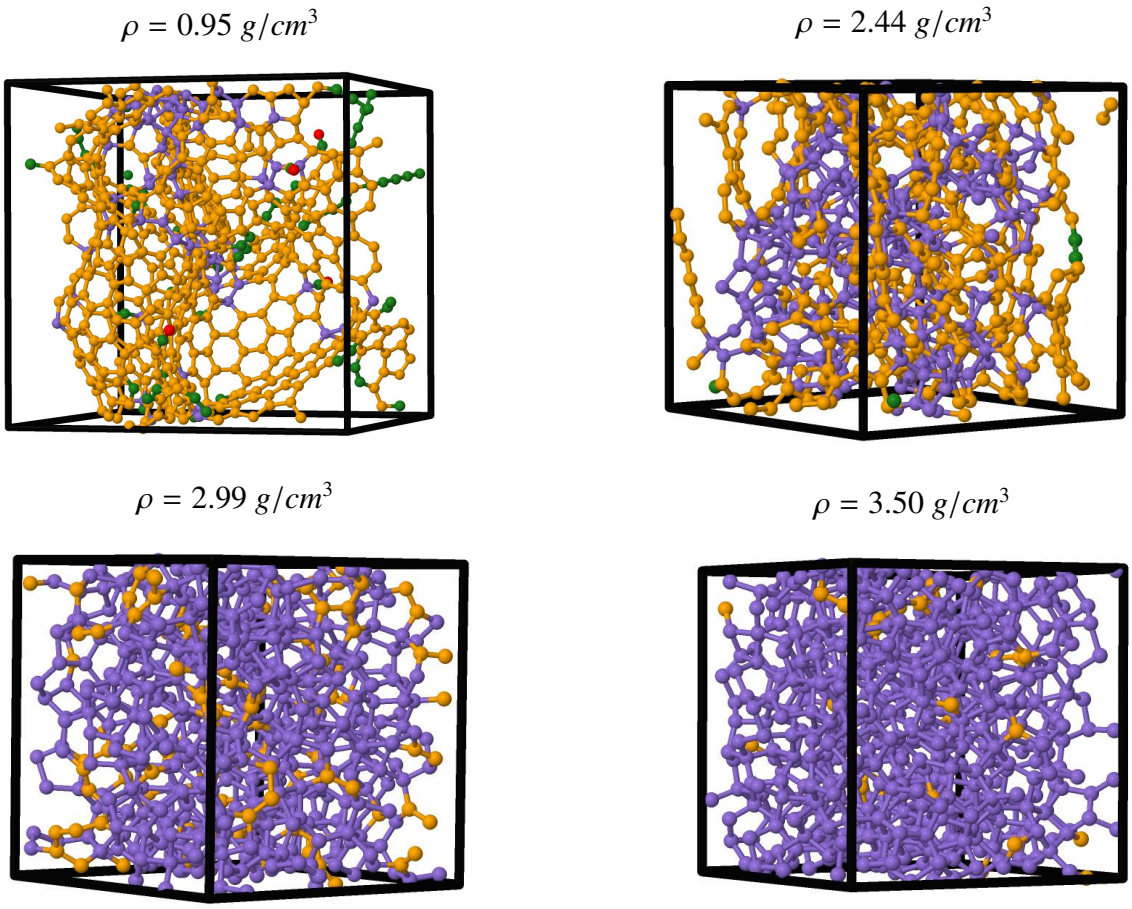

Figure 4.1: Visualization of the bonding in amorphous carbon for four different densities ρ. (F648): purple (sp^3), orange (sp^2), green (sp) and red (singly bonded). Periodic boundary condition were used, only atoms in reference cell are shown. Note the presence of amorphous graphene fragments with ring disorder at ρ = 0.95 g/cm^3

0.92 g/cm^3) [66] to compare the result of our lowest density model. Our models are summarized in Table. 4.1.

Table 4.1: Nomenclature and details of our models: Position of first minimum of RDF (r_{min}), average co-ordination number (n), percentage of sp^3, sp^2 and sp and total CPU time for the simulation (T_0).

Models	ρ = 3.50 (g/cm^3)			ρ = 2.99 (g/cm^3)			ρ = 2.44 (g/cm^3)			ρ = 0.95 (g/cm^3)	
	F648	V160	S160	F648	V160	S160	F648	V160	S160	F648	$V72^a$
n	3.96	3.98	3.94	3.83	3.75	3.85	3.41	3.26	3.58	3.00	2.67
% of sp^3	96.00	97.50	93.75	82.70	75.00	85.00	42.00	26.87	58.13	10.80	—
% of sp^2	4.00	2.50	6.25	17.30	25.00	15.00	57.40	72.50	41.25	79.00	66.67
% of sp	—	—	—	—	—	—	0.60	0.63	0.62	9.60	33.33
T_0^b	28.12	100	—	30.73	100	—	23.58	100	—	—	—

[a] *at density* 0.92 g/cm^3. *[66]*

[b] *CPU time for fixed number of total cores.*

4.2.3 Structural Properties

Structurally, amorphous carbon at density 3.50 g/cm^3 is diamond-like, (sp^3) whereas near graphitic density 2.27 g/cm^3 it is mostly sp^2 bonded and at even lower densities (< 2.0 g/cm^3) we observe a few sp conformations juxtaposed with sp^2 bonded carbon structures [89]. This evolution of bonding with density is shown in Fig. 4.1. We have assigned different color codes (via. Jmol[12]) for varying coordinations. Our sp^2/sp^3 ratios are close to experimental findings [107, 108]. In Fig. 4.2, we show a comparison of experimental static structure factor *S(Q)* and radial distribution function (RDF, *g(r)*) with our FEAR models.

[12] Jmol: an open-source Java viewer for chemical structures in 3D

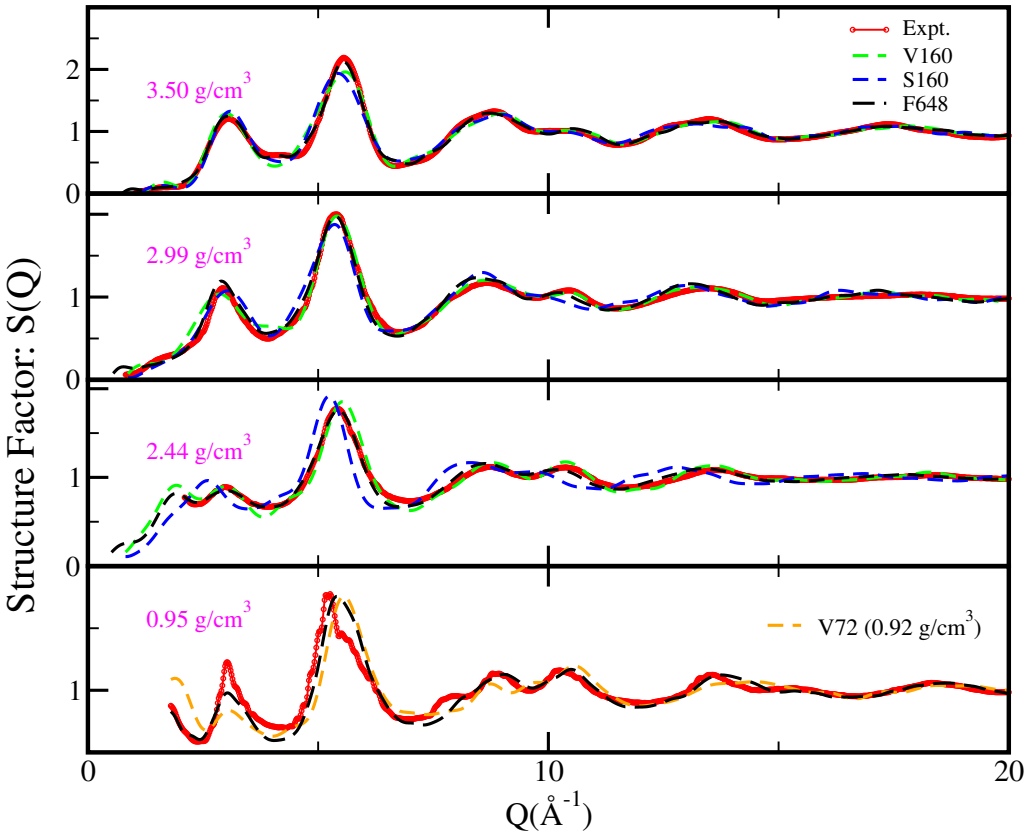

Figure 4.2: Structure factor for different models and their comparison with experiments (or WWW model for 3.50 g/cm^3). The experimental data are excerpted from previous literatures. [8, 21, 91, 105, 106]

At density 3.50 g/cm^3, we have used a Wooten-Wearie-Winer (WWW) [21] model as our input diffraction data, as no experimental data is available for this density. The WWW model is obtained with a bond-switching-algorithm [20] yielding an idealized (100 % sp^3) bonded network. These models have had many fruitful applications to tetrahedral amorphous systems and beyond [22]. We obtained close agreement for both *S(Q)* and *g(r)* with the WWW model, and we found 96 % sp^3 content in our model (Table 1). In contrast, earlier finding [109] report a lower concentration of sp^3 at this density.

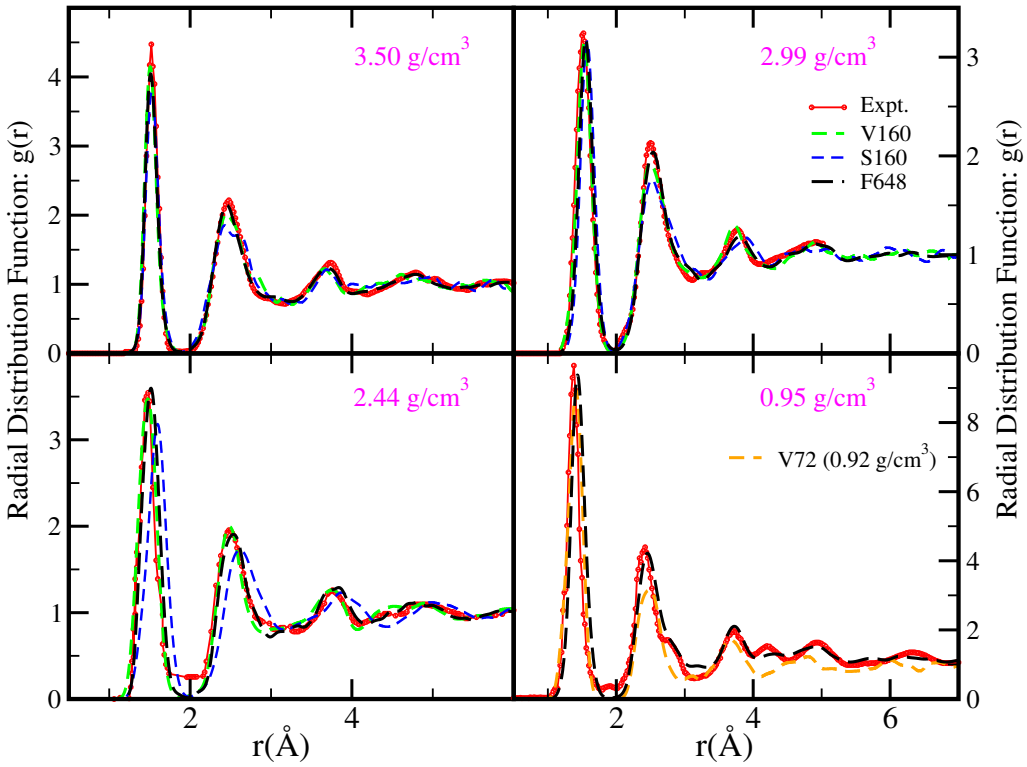

Figure 4.3: Radial distribution function of different models and their comparison with experiments. The experimental data are excerpted from previous literatures [8, 21, 91, 105, 106]

We have used experimental diffraction data for the next three calculations. At a density 2.99 g/cm^3, we employed the neutron diffraction data of *Gilkes et al.* [105] which is estimated to have 84% sp^3 bonding and a mean coordination-number n = 3.84. Our obtained *S(Q)* and *g(r)* are in an excellent agreement with experiment and we reproduce 82.70 % sp^3 bonding with mean coordination n = 3.83. Similarly, at density 2.44 g/cm^3, we have used experimental diffraction data of *Li and Lannin* [91] as our RMC input. We obtain pleasing agreement with the experimental diffraction data (*S(Q)* and *g(r)*) while some deviations are seen in MQ models. These results for densities (2.99 g/cm^3 and 2.44

g/cm^3) are in better agreement with the experiment compared to some earlier work [8, 89, 109].

At low density, our models reveal the presence of voids. For a density lower than graphite (2.26 g/cm^3) the system is comprised mostly of sp^2 carbon, interconnected with a small fraction of sp^3 sites. [110] A notable amount of sp bonded carbon is also seen at these densities [111]. Amorphous carbon at this density is also known as glassy carbon, a bit of a misnomer as the materials are not conventional glasses. The uncertainty of density, structure and significant H-content makes it difficult to study glassy carbons [87, 92, 112–114]. Most calculations include strong assumptions, such as building in perfect hexagonal graphitic or graphene sheets, coordination restrictions, bond-angle restrictions and so on [92, 113–115]. Some of these constrained models were found to be unstable and changed significantly upon relaxation [112].

We have previously carried out calculations in the low density regime [66]. We worked in a density range of 0.923 g/cm^3 - 1.6 g/cm^3. As a representative of this lower density regime in this paper, we have employed neutron diffraction data obtained for silicon carbide-derived nanoporous carbon(SIC-CDC) [106] at a density 0.95 g/cm^3 as FEAR input. Our F648 model yields the most reliable picture of glassy carbon starting from random, a suitable minimum of SIESTA and without any bias (*ad hoc* constraints). The resulting model consists of obvious fragments of interconnected and warped amorphous graphene fragments (with sp^2 bonding, and ring disorder: hexagons, pentagons, heptagons and octagons). We have successfully reproduced the major RDF peaks for glassy carbon occurring at, 1.42 $\AA$, 2.46 $\AA$, 2.84 $\AA$ and so on [98]. There is a slight deviation in the low Q range which was also observed in previous work [92, 106] done with (> 3200 atoms), hinting that it is not a finite size artifact.

Bond angle distribution (BAD) and ring statistics provide vital information about microstructure. In a typical RMC simulation with a perfect fit to experiment, an

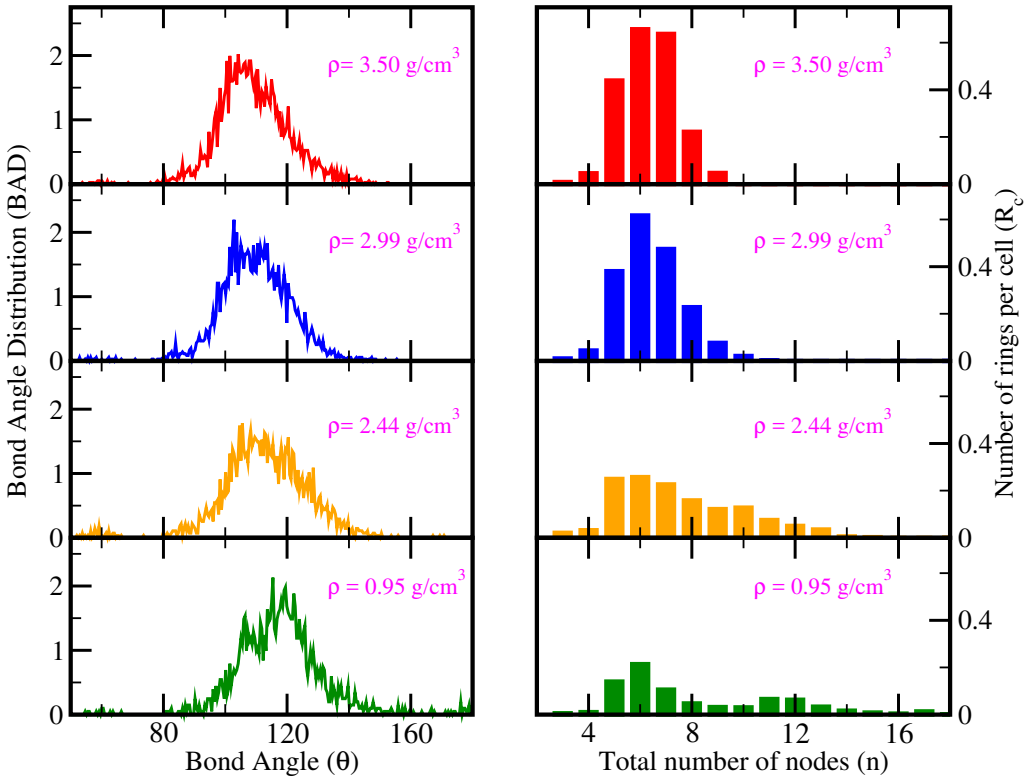

Figure 4.4: Bond angle distribution (BAD) and ring statistics of FEAR (F648) models.

exaggerated peak near $\sim 60.0^o$ is observed in BAD [2]. Although, constraints have been employed [8] to avoid these unrealistic cases, FEAR achieves it without external bias. We report our results for BAD and ring statistics in Fig. 4.4. At the highest density the BAD peak is close to the tetrahedral angle of 109.5^o, with small deviation. At low densities the BAD peak is closer to 120.0^o, indicating trigonal symmetry is dominant in these structures. It is reported that even with high sp^2 content BAD peak at low density is close to 117.0^o [97].

We have shown in Fig. 4.4 that amorphous carbons mostly prefer 5-7 membered ring structures. This is also true for the high sp^2 concentration structures which further clarifies that these a-C structures are different from graphite (only 6 membered rings). A negligible fraction of smaller ring structures were also observed but these are less than

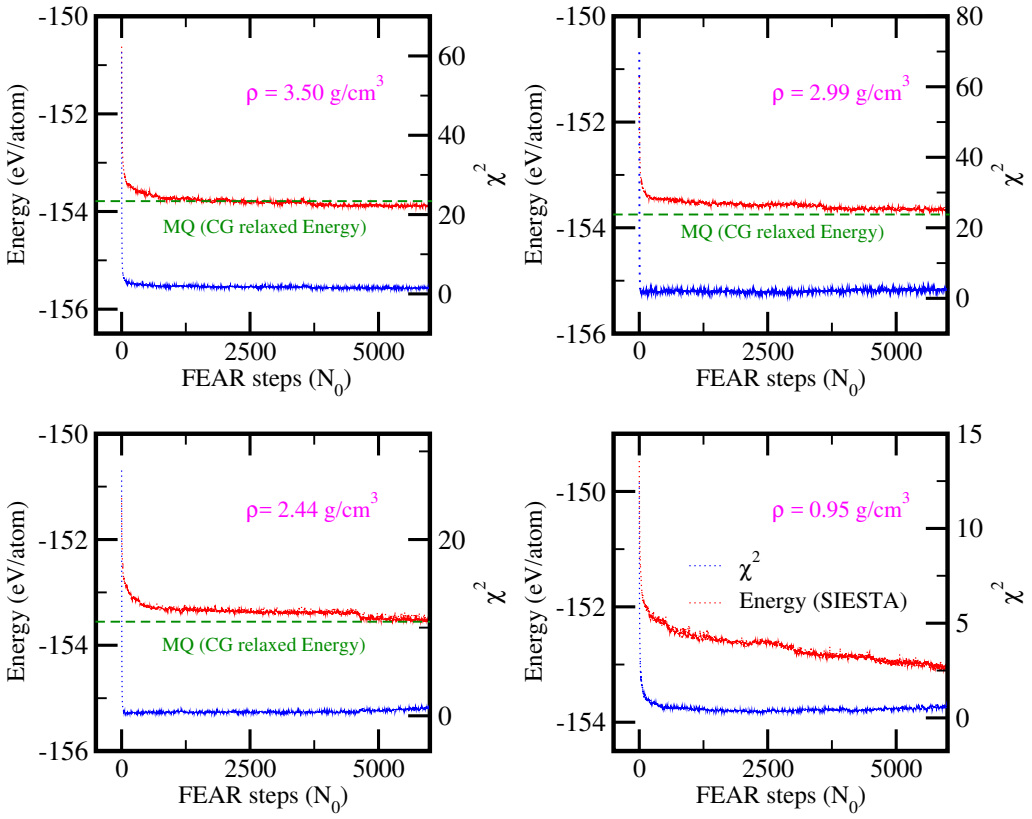

Figure 4.5: Plot of total energy (SIESTA) per atom (red line, F648) and cost function (blue line, F648) (χ^2) versus number of FEAR steps (N_0). Final relaxed MQ energies are shown for comparison (green line, S160)

MD and other calculations [8]. The ring statistics were evaluated with King's shortest path method [54] using ISAACS software [56].

In FEAR, we obtain low values of χ^2 in conjunction with a local energy minimum.[13] Our plot of the variation of total energy (E) and χ^2 is shown in Fig. 4.5. The results obtained shows that an initial structure is formed within few hundred FEAR steps. These states have more or less the same average energy and as we move along with FEAR steps these defects are removed, leading ultimately to a chemically realistic structure.

[13] χ^2 measures goodness of fit between experimental and FEAR model [2, 3, 48]

4.2.4 Electronic Properties

The concentration of sp, sp^2 and sp^3 sites strongly influences the electronic density of states (EDOS). As in the case of diamond, a-Carbon with high sp^3 is non-conducting. We have presented plots of the EDOS of our F648 models in Fig. 4.6, where we have also decomposed the total EDOS by sp^3, sp^2 and sp contributions. We can clearly see that the sp^2 states for density 3.50 g/cm^3 act as a defect and leads to formation of a pseudo-gap. [116] Subsequently, a-Carbon models at lower density appear to be conducting as expected [89, 102]. In Fig. 4.6 (Right panel) we show the plot of Inverse Participation Ratio (IPR) [103], IPR gives information about the spatial localization of electronic states. As seen in Fig. 4.6, the gap states for high density are highly localized while the lower two density have much more extended states.

4.2.5 Vibrational Properties

The vibrational density of states (VDOS) provides crucial information about changes in local bonding environment which is very effective test for theoretical models [117] and offers a remarkably direct comparison between experiment and theory. It is well know that a-Carbon exhibits two major peaks in VDOS and Raman spectra; occurring at: $\sim$ 1500 cm^{-1} and $\sim$ 800 cm^{-1} [91]. In contrast, several theoretical models show a single broad peak occurring roughly at $\sim$ 1100 cm^{-1} [116, 118].

We have also calculated the vibrational density of states (VDOS) of our four F648 models. The dynamical matrix was obtained by displacing each atom in 6-directions ($\pm x$,$\pm y$,$\pm z$) by a small displacement of 0.015 $\AA$ (see details [65]). Our VDOS plots for the four models are shown in Fig. 4.7.

Our results show reasonable agreement with the literature. There is distinct bifurcation seen in our F648 models as seen in several experiments. At 3.50 g/cm^3, we compare our result with VDOS obtained for 216-WWW model [21]. We observed a slight

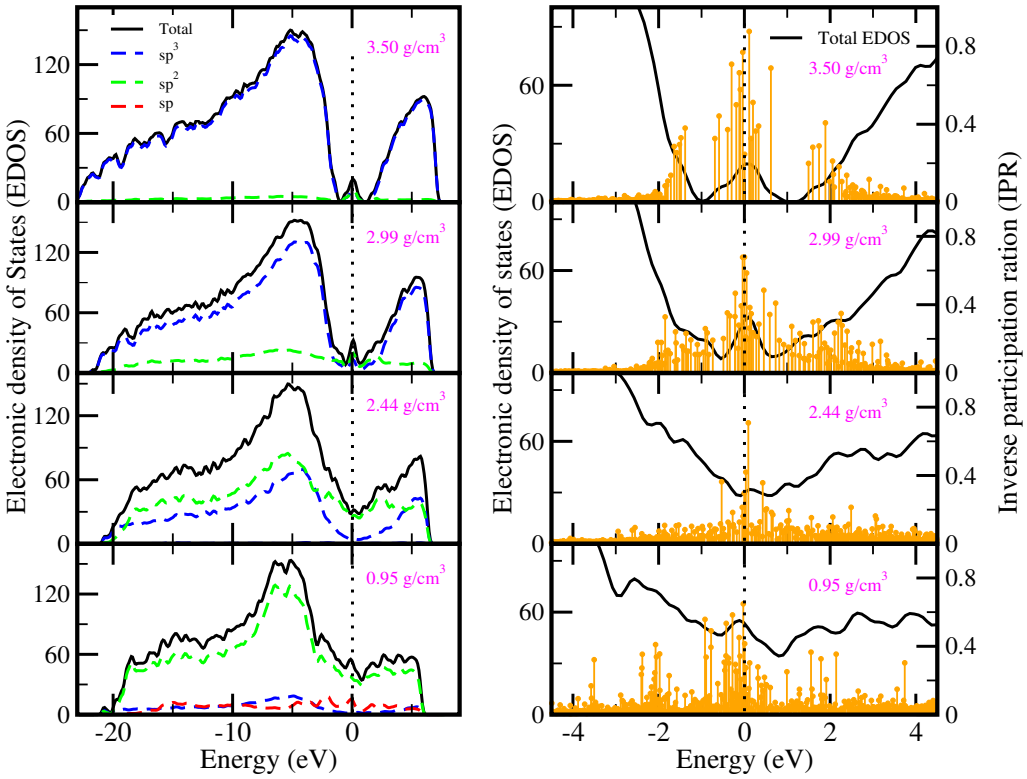

Figure 4.6: Plot of EDOS (E_F=0 eV) of F648 models: (**Left panel**) black-solid (total EDOS), blue-dashed (sp^3 EDOS), green-dashed (sp^2 EDOS) and (green-dashed, sp EDOS). (**Right panel**) orange-drop lines (IPR) and black-solid (total EDOS).

shift for 2.99 g/cm^3 as compared to model at 3.50 g/cm^3. At 2.44 g/cm^3, we have compared our results (sp^3 fraction 42.0%) with experimental data [117] obtained for amorphous carbon containing sp^3 fraction at 60% ± 10%, we have a qualitative match with the experimental finding. The position of two peaks and their relative intensity is reported to slightly differ for different incident energies and sp^3 fraction [117, 119].

At low density 0.95 g/cm^3, our model resembles distorted graphene structures (see Fig. 4.1). We have compared our results with 2D a-graphene result of *Li and Drabold* [95]. The plots bear a remarkable similarity, most notably the peak occurring at $\sim 700cm^{-1}$ and $\sim 1400cm^{-1}$. This is surprising in view of significantly different topology

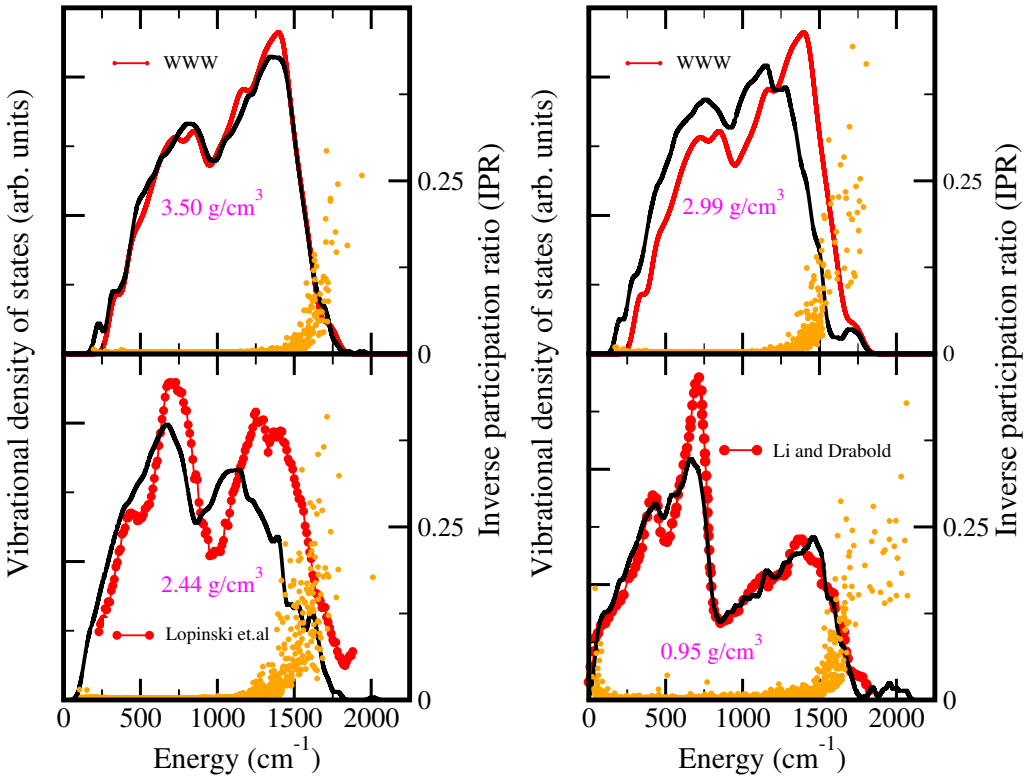

Figure 4.7: Plot of Vibrational density of states (VDOS)(black line, F648), comparison with previous literatures(red dots and lines) [21, 95, 117] and Inverse participation ratio (IPR) (orange dots) for F648 models.

(one is 3-D, the other one 2-D). We have also computed the inverse participation ratio (IPR) for our F648 models. IPR, gives localization of these vibrational modes [65, 66]. Our result for IPR shows that vibrational modes are extended at the low frequency regime and localized modes are only observed a higher frequency than $\sim 1500 cm^{-1}$, which are likely to be localized stretching modes [66, 118].

4.2.6 Conclusion

We have used a *uniform approach* to model a-Carbon using FEAR at various densities. We have used method FEAR efficiency to obtain large size (648 atom) "*ab*

initio" models. The inclusion of *ab initio* interactions not only guides us towards a chemically correct structures, it directly helps us to avoid chemically unphysical structures. A typical RMC based calculation fails to accurately model amorphous systems without the addition of experimental based constraints. In our experience, FEAR yields a *lower DFT energy* and takes far less computer time to converge compared to MQ with identical interactions. We have established a set of accurate *ab initio* models for amorphous carbon that we hope will serve as a benchmark for future modeling studies.

4.3 Amorphous Graphene: A Constituent Part of Low Density Amorphous Carbon

4.3.1 Introduction

Amorphous graphene (a-G): an idealized 2-D structure consisting of 5-6-7 polygons with predominant sp^2 bonding has presented a challenge for extraction. This has been achieved by exposure of an of electron beam to a crystalline/pristine graphene (p-graphene) sheet, to produce an amorphous monolayer [120]. Similarly, a-G has been modeled by introducing 5 and 7 member rings with a *Wooten-Weaire-Winer* (WWW) scheme [24, 25, 95, 121]. In this work we have used a recently developed hybrid approach FEAR (Force Enhanced Atomic Refinement) method, an *ab initio* structural refinement technique, to show that low density phases of Carbide-Derived Carbons (CDC) [110, 122–124] are a form of three dimensional a-G (warped, wrapped 2D a-G sheets with ring disorder and defects).

4.3.2 Model and Methodology

In this work, a starting *random* configuration is fitted to experimental data with RMCProfile [104] with values of $M = 1$ and $N \sim 100$ respectively. We have used silicon carbide-derived nanoporous carbon (SIC-CDC) [106] at density 0.95 g/cm^3 as our experimental data. We have used a maximum RMC step size of 0.15-0.375 $\mathring{A}$, restricting

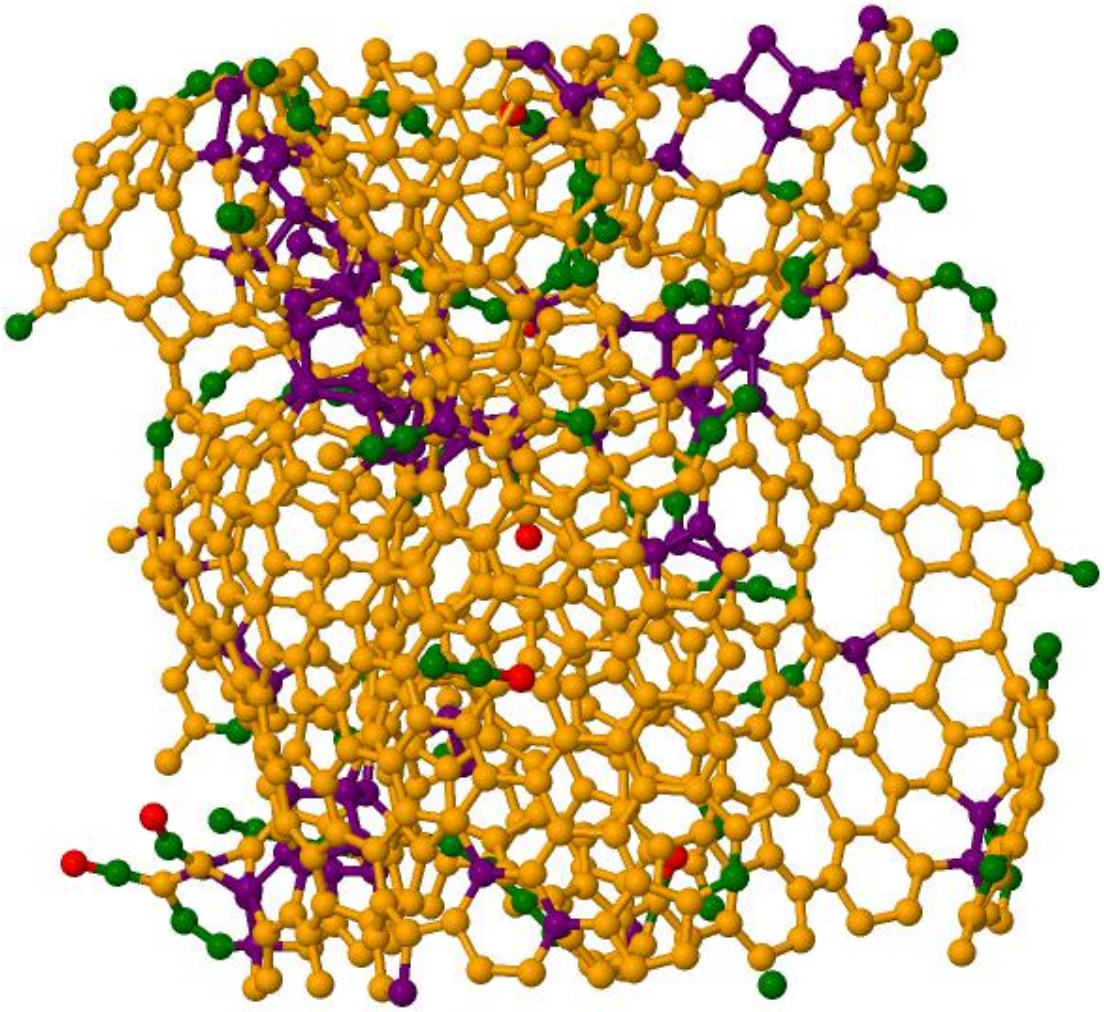

Figure 4.8: Structure model of 3-D amorphous graphene (800 atom). color coding: purple (sp^3), orange (sp^2), green (sp) and red (singly bonded).

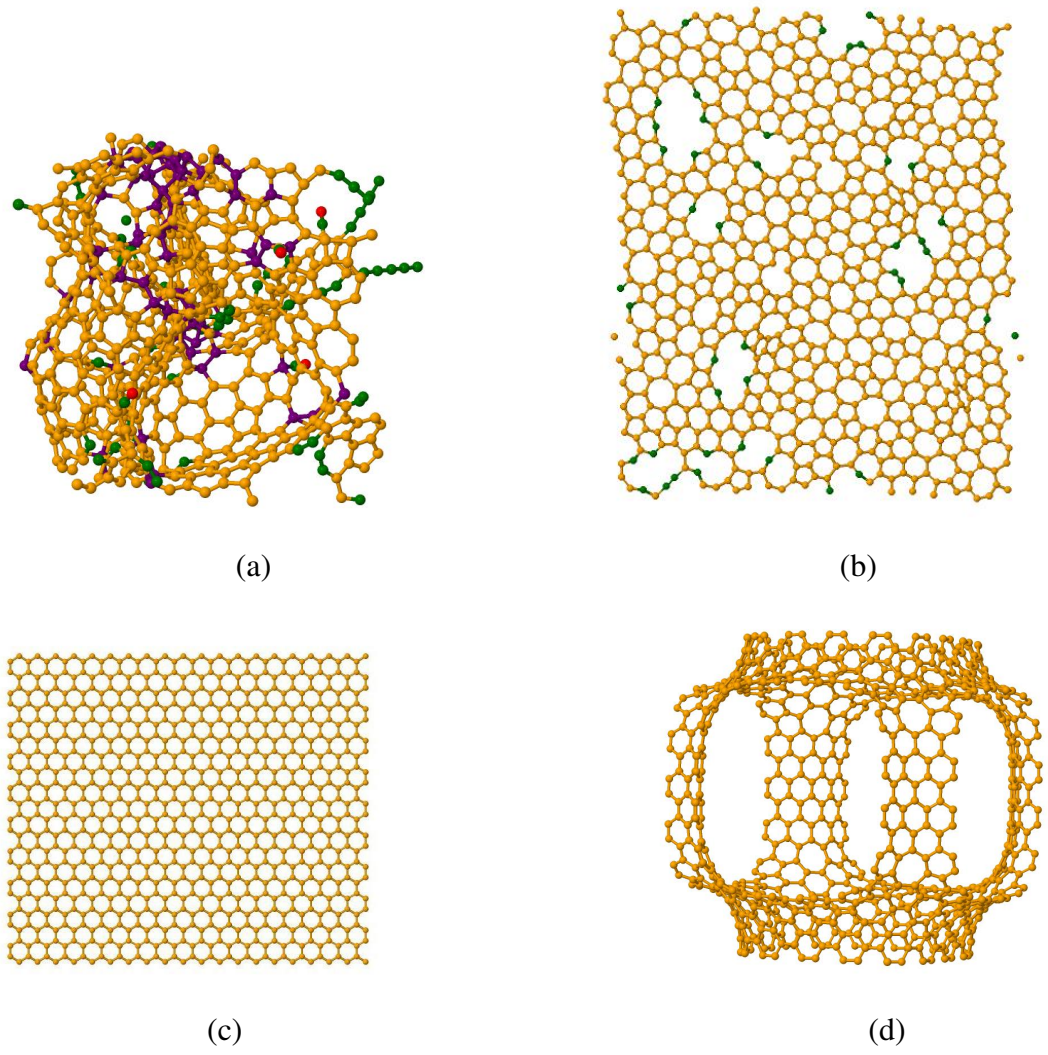

Figure 4.9: Structure models: (a) 3-D a-graphene (648 atom), (b) 2-D a-graphene [95] (c) 2-D crystalline graphene, and (d) 3-D schwarzite [125]. color coding: purple (sp^3), orange (sp^2), green (sp) and red (singly bonded).

minimum approach distance between atoms to 1.05 $\AA$, a fixed spacing of 0.02 $\AA$ and 0.04 weight of the experimental data. The relaxation step was performed with single-ζ basis, periodic boundary conditions and Harris functional at constant volume using DFT code SIESTA [36]. Finally, we relax converged models using Vienna *ab initio* package

(VASP) [126, 127]. All the calculations were performed with a single k-point $\Gamma(\vec{k} = 0)$ and the local density approximation, and PAW potentials. We started with random initial configurations, and made FEAR models with 216, 648 and 800 atoms. We observe in passing that FEAR is computationally highly advantageous compared to MQ, requiring far fewer calls to the *ab initio* code (in the FEAR CG step). We explore reproducibility with models containing 216, 648 and 800 atoms, and show that a consistent network topology emerges.

To explain and calibrate the results, we have created MQ models with 648 and 216 atoms. The 648-atom MQ model was equilibrated at 7000 K, then cooled to 300 K, and after further equili- bration at 300 K, was relaxed using the CG method. This process required 50 ps of total simulation time. Due to the large size of the system we have used the DFT code SIESTA with Harris functional to form this model. We also have created a 216-atom MQ model with the help of plane wave DFT code VASP, using the local-density approximation with Ceperley-Alder (CA) exchage correlation functional. The VASP model was first equilibrated at 7500 K, then quenched to 300K in multiple steps over a total simulation time of 42 ps using a time step of 2 fs. A plane wave cut off of 350 eV and energy difference criteria of 10^{-4} was chosen for the simulation. These are typical simulation times used in preparing accurate models of amorphous systems[14] Additionally, we discuss crystalline/pristine graphene (**p-graphene**, 800 atoms) [95] and a schwarzite model (792 atoms) [125] for comparison.

[14] It is worth noting that melt-quench (MQ) process does depends on cooling rate. However, our earlier study done for several models of amorphous carbon at different cooling rates showed only slight differences in bonding (sp, sp^2 and sp^3) preferences without much change in other observables such as electronic density of states or vibrational properties [66]. Recently it has been shown that very slow quenching rate improves the quality of MQ models [128, 129]. These simulations are very extended and do not seem to be an efficient way to model amorphous systems. FEAR produces models with DFT accuracy taking less CPU time. Computationally speaking, our 216 atom FEAR model presented here requires 1/14 the time used for the 216 atom VASP (MQ) model and requires total force calls of ($\sim$ 6000 − 8000) to obtain a converged model.

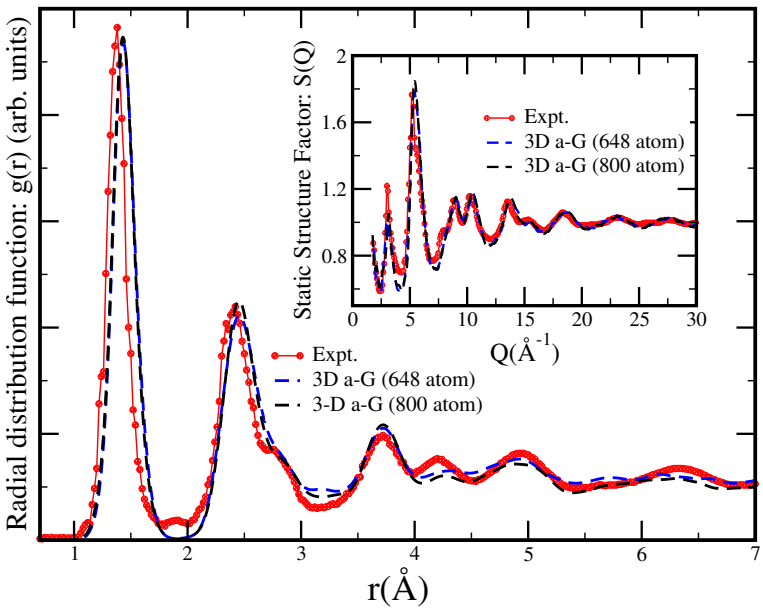

Figure 4.10: Comparison of radial distribution function $g(r)$ and structure factor ($S(Q)$, inset) of FEAR models with experiment(ρ = 0.95 g/cm^3). [106].

4.3.3 Results

In Fig. 4.9, we show the topology of our models. sp^2 bonding (in orange) dominates each of these structure. 3-D amorphous graphene has a few sp^3 bonded sites ($\sim 11\%$) which mainly connect one sp^2 graphene fragment to another. Similarly, a few sp bonded sites appear in both 3-D and 2-D amorphous graphene. In Fig. 4.10, we compare our results with the experimental results of nano-porous Silicon Carbide Derived Carbon (SiC-CDC) at density 0.95 g/cm^3 [106]. We observe good agreement with the experiment (by construction) while a slight deviation is observed upon complete *ab initio* (VASP) relaxation. We have plotted the radial distribution function $g(r)$ for the four models and the static structure factor $S(Q)$ in Fig. 4.11. 3-D a-graphene model has first nearest-neighbor distance at 1.42 $\AA$ and second nearest-neighbor distance at 2.45 $\AA$ same as crystalline graphene model. Meanwhile, the 2-D a-graphene model [25, 95] reveals a

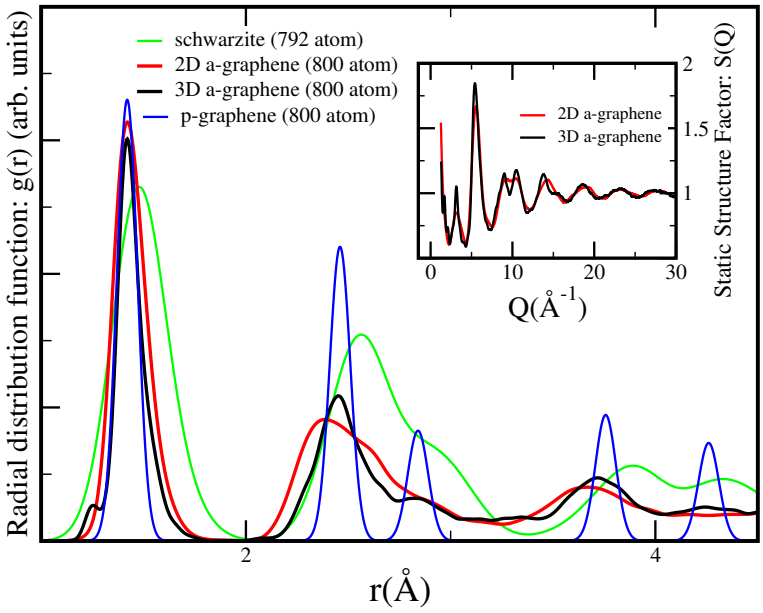

Figure 4.11: Radial distribution functions $g(r)$ of four models (3-D a-graphene (800 atom), 2-D a-graphene (800 atom), crystalline/pristine graphene (p-graphene, 800 atom) and schwarzite (792 atom)), **(inset)** Comparison of static structure factor $S(Q)$ between 3-D and 2-D a-graphene.

second peak in $g(r)$ with second nearest-neighbor at 2.38 $\AA$, suggesting a broader distribution bond-angles than 3-D a-graphene model [118] (see Fig. 3(right panel)).

Both 2-D and 3-D a-graphene exhibit bond angle distribution (BAD) with peak around $\sim 120^o$. The full width at half maximum of BAD has a value of 27.45^o and 26.65^o for 2-D and 3-D graphene respectively. It is observed that with high sp^2 concentration, BAD is around 117.0^o [97]. The plot of static structure factor $S(Q)$ for 2-D and 3-D a-graphene shows a striking similarity between these structures.

In Fig. 4.12, the ring distribution shows that both 2-D and 3-D a-graphene have ring structures of various sizes (mostly 5, 6 and 7), as in shungite [130]. In contrast, both schwarzite and p-graphene exhibit 6-membered rings (exception: schwarzite has few

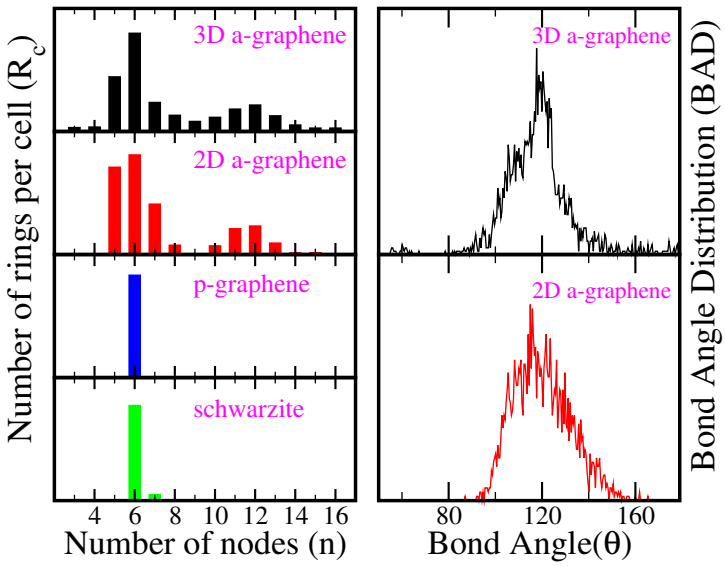

Figure 4.12: Comparison of ring distribution between the four models and plot of bond-angle distribution of 3-D and 2-D a-graphene.

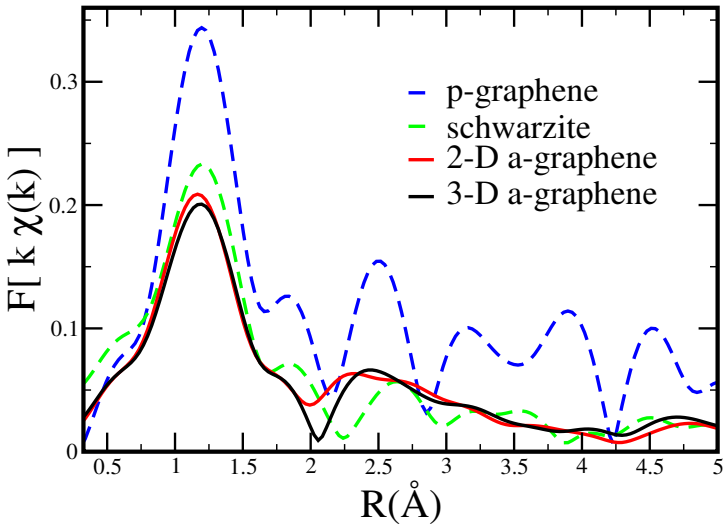

Figure 4.13: Fourier transform of Carbon K-edge EXAFS spectra [$k\chi(k)$] for the four models.

7-membered rings). We have also computed Extended X-ray Absorption Fine Structure (EXAFS) for our four models (see Fig.4.13). EXAFS is valuable for the first-shell information [131]. We observe strong structural correlation of 3-D graphene and 2-D graphene in our EXAFS plot, [132, 133] whereas pristine graphene and schwarzite structures distinctively differ from these structures. We show an EXAFS signatures differentiating 2-D and 3-D a-G (a peak at $\sim 2.2\ \mathring{A}$, see Fig. 4.13).

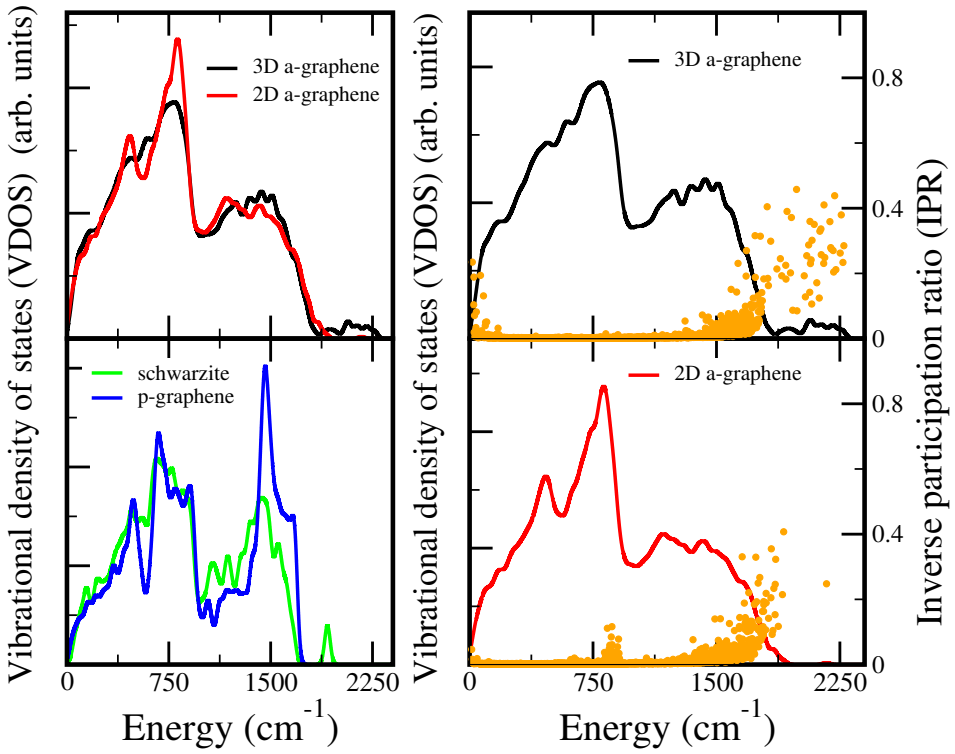

Figure 4.14: Plot and comparison of vibrational density of states for the four models. The 3-D graphene (a-carbon) has excellent similarity with the 2-D a-graphene. The yellow dot represent vibrational inverse participation ratio.

The electronic density of states (EDOS) and vibrational density of states (VDOS) are reported next. The low energy modes are related to mechanical properties and low temperature thermal conductivity of a material [59–62]. The force constant matrix was

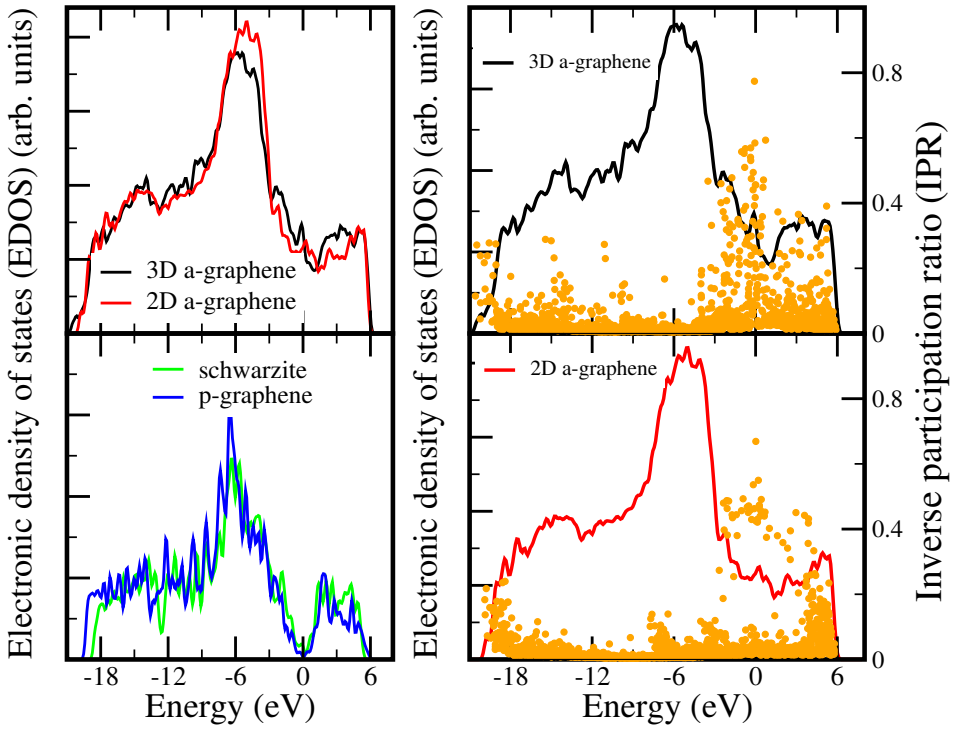

Figure 4.15: Plot and comparison of EDOS (E_F=0 eV) and localization (IPR, yellow dots).

obtained from a finite difference method displacing every atom in 6-directions ($\pm x$,$\pm y$,$\pm z$) with a small displacement of 0.015 cm^{-1}. The first three frequencies arising due to supercell translations which are very close to zero are neglected in our calculation and all our other frequencies are positive (no imaginary modes). Once again due to gigantic size of our model we have Harris functional to our advantage with a double-ζ basis (see details [65, 66]). Our 3-D amorphous graphene shows two distinctive components in VDOS (see Fig. 4.14). A sharp peak around $\sim$ 814 cm^{-1} and a broader peak at $\sim$ 1300 cm^{-1}, and a narrow neck is observed at $\sim$ 470 cm^{-1}. We have an surprising match of VDOS for our model and 2-D amorphous graphene. The VDOS for crystalline graphene and schwarzite reveal a different profile to amorphous graphene. The pristine graphene VDOS peaks are observed at: $\sim$ 490 cm^{-1}, $\sim$ 678 cm^{-1} and $\sim$ 1460 cm^{-1}, with peak intensities and position quite different to amorphous graphene. We associate the peak at

$\sim 814\ cm^{-1}$ with a-graphene and a peak around $\sim 1460\ cm^{-1}$ for p-graphene as signature peaks.

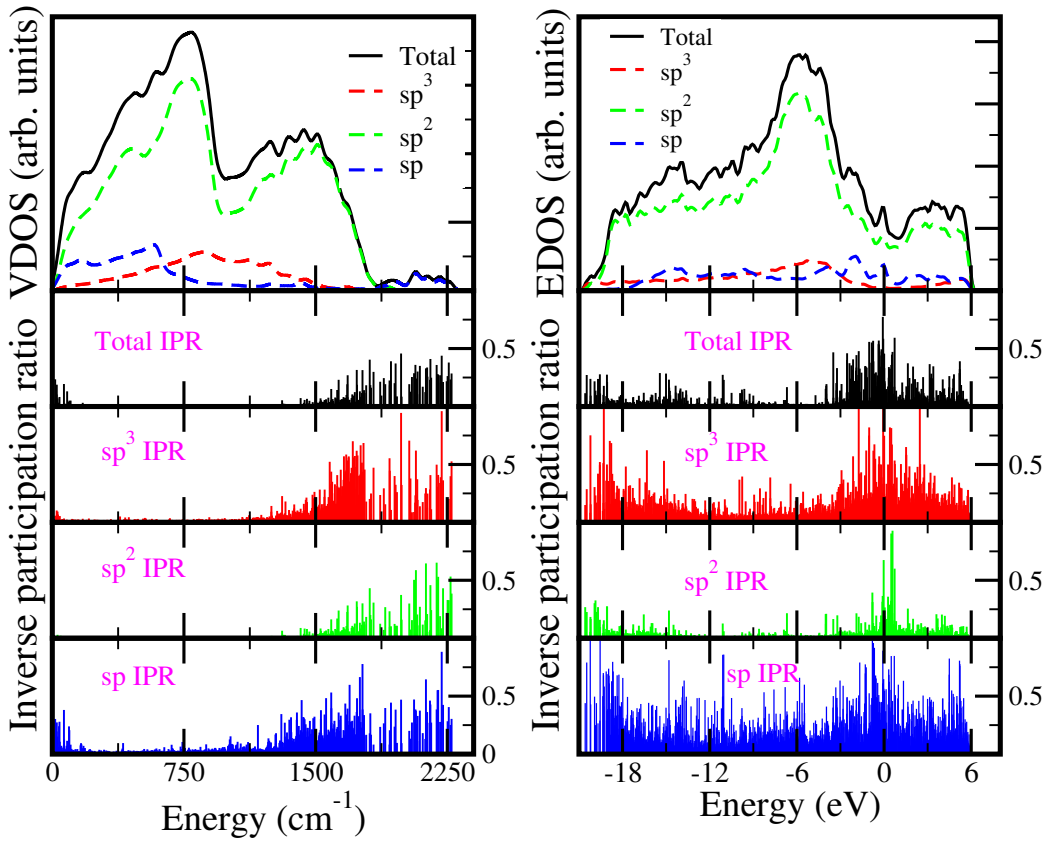

Figure 4.16: **(Left panel)** Plot of Total, (sp^3, sp^2, sp) projected VDOS and vibrational IPR for 3-D a-graphene model. **(Right panel)** Plot showing Total, (sp^3, sp^2, sp) projected EDOS and electronic IPR for the 3-D a-graphene model.

In Fig. 4.15, we report the EDOS for these four models. The EDOS for both 3-D and 2-D graphene exhibit a striking similarity, and various defects (sp^3 and sp) and topology seem to have modest effect. A similar observation was also seen in ZrC-CDC structure [122]. Separate computations (not shown here) are in agreement with previously

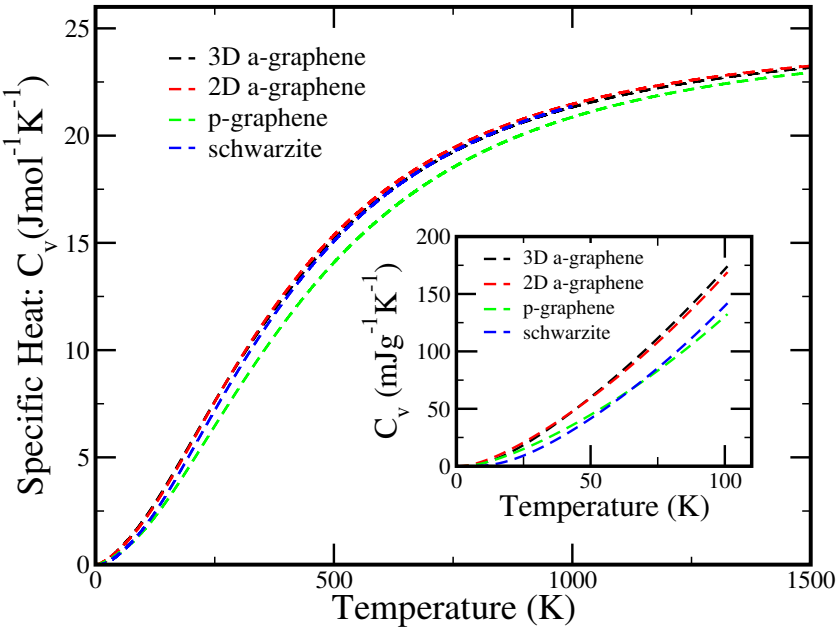

Figure 4.17: Specific heat plots for the four models. (**Inset**) Low temperature specific heat of the four models.

established result of *Van Tuan et. al* [134]. We note that the EDOS of crystalline graphene and schwarzite are quite distinct from its amorphous counterpart.

The electronic states and vibrational states of amorphous solids are affected by disorder present in the structure. The localization of electronic/vibrational states can be quantified by computing inverse participation ration (IPR) [58]. A completely localized state would have an IPR value unity while an extended state has a value of $(1/N)$ i.e. distributed over N atoms. Vibrational IPR is evaluated using obtained normalized displacement vectors (u_i^j) as shown in Equn. 1.12. Similarly, localization of n^{th} electronic state is computed as shown in Equn. 1.7. By comparison of the localization of states for both 2D and 3D a-graphene near Fermi energy, we see mostly extended states with few weakly localized states. We again obtain that the vibrational modes are mostly extended, with few localized modes around $\sim 1800 - 2000\ cm^{-1}$. We further dissect the VDOS and

EDOS into sp, sp^2 and sp^3 contributions to gain further insight into 3D a-graphene model (Fig. 4.16). The decomposed VDOS shows that sp^2 bonding clearly dominates the vibrational spectrum. Further, we can clearly observe the narrow neck at $\sim 470\ cm^{-1}$, seen in 2D a-G. We further decompose the vibrational localization into sp, sp^2 and sp^3 components. Most localization in this system is contributed by sp and sp^3 bond. Decomposition of EDOS into sp, sp^2 and sp^3 contributions shows quite an interesting result. The sp and sp^3 bonding atoms have almost no effect on the electronic properties both at conduction band or deep into valance band. Similar to VDOS, most of the electronic localization in due to sp and sp^3 bonded carbon networks. We have computed specific heat in the harmonic approximation, $C_v(T)$ for the four models shows similar pattern at high temperatures, with p-graphene showing slight deviation compared to other models (see Fig. 4.17). The inset shows more prominent changes at the lower temperatures (0 K to 100 K). The two amorphous graphene models (2-D and 3-D) increases with same slope between 0 K to 100K. Meanwhile, a deviation from a-graphene is seen for the case of p-graphene and schwarzite.

4.3.4 Conclusion

In summary, we have shown that a-C with density $0.95\ g/cm^3$ is a form of a-G. We provide a detailed analysis of our model by computing structural, vibrational and electronic properties and comparing to 2D amorphous graphene along with other sp^2 structures. Surprisingly, bonding defects ($\sim 11\%\ sp^3$ and $\sim 11\%\ sp$) has little effect on properties like EDOS and VDOS.

5 Conclusion

In the first three chapters we have extensively discussed the vibrational properties of two amorphous system: a) amorphous silica and b) low density amorphous carbon. The first study is interesting as it is one of largest *ab initio* based model used to probe vibrational properties of amorphous silica. Our study also has qualitative agreement with the experiment and produces all four principal peak observed in experimental findings. In addition, we also proved that the plateau observed ($\sim$ 20 K) in the specific heat plot is due to "*Boson peak*" seen in the VDOS.

In our second study we have studied the low density regime of amorphous carbon by preparing several DFT models for density range $0.90 - 1.6\ g/cm^3$. Our studies reveal that at these densities amorphous carbon is dominated by sp^2 bonding but still possess significant proportion of sp and sp^3. For these low densities, the vibrational density of states is computed for the first time, along with localization of modes and the specific heat with comparison to experiments. The vibrational modes are well extended and are more complex than simple molecular pictures. We note similarities and differences between a-C and hypothetical amorphous graphene material.

In the last chapter, we have discussed the results obtained from a novel modeling technique FEAR. We have extended FEAR to model several large systems. This includes challenging system like amorphous carbon across densities and we reveal that low density nano-porous carbon as amorphous graphene. FEAR provides a suitable alternative as it does not incur expensive computational cost compared to the melt quench (MQ) method. In FEAR inclusion of *ab initio* interactions guides us towards a chemically sensible structures. It is a direct upgrade to usual RMC method as FEAR avoid chemically unphysical structures. A typical RMC based calculation fails to accurately model amorphous systems without the addition of experimental based constraints. We have used an unbiased and uniform approach to model amorphous carbon for density range

$0.923 - 3.5\ g/cm^3$. The 648 atom models at various densities represent the largest *ab initio* based model and will act as a benchmark calculations for future research. Lastly, we extended our work on FEAR on low density amorphous carbon. We incorporate the experimental data of nano-porous carbon and *ab initio* interactions to create a model of amorphous graphene. We compare our obtained graphene network with 2D-amorphous graphene, crystalline graphene and schwarzite to verify that these are indeed warped form of amorphous carbon.

5.1 Future Works

FEAR method thus far has been carried out in limited systems. An immediate application of this method would be on complex problem like Bulk Metallic Glasses (BMG) [135]. Further, extension of FEAR to make it a general method, incorporation of Extended X-ray Absorption Fine Structure (EXAFS) would be ideal. EXAFS experimental data would be extremely useful for complex metallic alloys as these multicomponent system are complicated and neutrons total scattering may not be sufficient to provide the necessary compositional contrast.

Additionally, machine learning based potentials have shown to be a great asset to simulate system for a long time scale without compromising the accuracy of the system [128, 129]. Since, FEAR needs fewer force call thus we can use these inexpensive interactions to model even large systems.

References

[1] G. T. Barkema and N. Mousseau, "Event-based relaxation of continuous disordered systems," *Phys. Rev. Lett.*, vol. 77, pp. 4358–4361, Nov 1996.

[2] A. Pandey, P. Biswas, and D. A. Drabold, "Force-enhanced atomic refinement: Structural modeling with interatomic forces in a reverse monte carlo approach applied to amorphous si and sio_2," *Phys. Rev. B*, vol. 92, p. 155205, Oct 2015.

[3] A. Pandey, P. Biswas, and D. A. Drabold, "Inversion of diffraction data for amorphous materials," *Scientific Reports*, vol. 6, p. 33731, Sep 2016.

[4] D. A. Drabold, "Topics in the theory of amorphous materials," *The European Physical Journal B*, vol. 68, pp. 1–21, Mar 2009.

[5] R. A. Street, ed., *Technology and Applications of Amorphous Silicon*, vol. 37. Singapore: Springer-Verlag Berlin Heidelberg, 2000.

[6] L. Li, M. Xu, W. Song, A. Ovcharenko, G. Zhang, and D. Jia, "The effect of empirical potential functions on modeling of amorphous carbon using molecular dynamics method," *Applied Surface Science*, vol. 286, pp. 287 – 297, 2013.

[7] J. Robertson, "Diamond-like amorphous carbon," *Materials Science and Engineering: R: Reports*, vol. 37, no. 4, pp. 129 – 281, 2002.

[8] G. Opletal, T. C. Petersen, D. G. McCulloch, I. K. Snook, and I. Yarovsky, "The structure of disordered carbon solids studied using a hybrid reverse monte carlo algorithm," *Journal of Physics: Condensed Matter*, vol. 17, no. 17, p. 2605, 2005.

[9] I. Valov, R. Waser, J. R. Jameson, and M. N. Kozicki, "Electrochemical metallization memoriesfundamentals, applications, prospects," *Nanotechnology*, vol. 22, no. 25, p. 254003, 2011.

[10] N. E. Cusack in *The Physics of Structurally Disordered Matter* (D. F. Brewer, ed.), vol. 37, Bristol and Philadelphia: Adam Hilger, 1987.

[11] S. R. Elliott, *Physics of amorphous materials*. Newyork: Longman Inc., 1984.

[12] R. Zallen, *The Physics of Amorphous solids*. Newyork: John Wiley and Sons, INC., 1998.

[13] W. H. Zachariasen, "The atomic arrangement in glass," *Journal of the American Chemical Society*, vol. 54, no. 10, pp. 3841–3851, 1932.

[14] N. F. Mott, "Electrons in glass," *Contemporary Physics*, vol. 18, no. 3, pp. 225–245, 1977.

[15] R. J. Bell and P. Dean, "Atomic vibrations in vitreous silica," *Discuss. Faraday Soc.*, vol. 50, pp. 55–61, 1970.

[16] D. Polk, "Structural model for amorphous silicon and germanium," *Journal of Non-Crystalline Solids*, vol. 5, no. 5, pp. 365 – 376, 1971.

[17] L. Guttman, "Simulation of continuous random network models with periodic boundary conditions," *AIP Conference Proceedings*, vol. 20, no. 1, pp. 224–228, 1974.

[18] L. Guttman, "Vibrational spectra of four coordinated random networks with periodic boundary conditions," *AIP Conference Proceedings*, vol. 31, no. 1, pp. 268–272, 1976.

[19] L. Guttman, W. Y. Ching, and J. Rath, "Charge-density variation in a model of amorphous silicon," *Phys. Rev. Lett.*, vol. 44, pp. 1513–1516, Jun 1980.

[20] F. Wooten, K. Winer, and D. Weaire, "Computer generation of structural models of amorphous si and ge," *Phys. Rev. Lett.*, vol. 54, pp. 1392–1395, Apr 1985.

[21] B. R. Djordjević, M. F. Thorpe, and F. Wooten, "Computer model of tetrahedral amorphous diamond," *Phys. Rev. B*, vol. 52, pp. 5685–5689, Aug 1995.

[22] D. N. Tafen and D. A. Drabold, "Realistic models of binary glasses from models of tetrahedral amorphous semiconductors," *Phys. Rev. B*, vol. 68, p. 165208, Oct 2003.

[23] D. N. Tafen and D. A. Drabold, "Models and modeling schemes for binary iv-vi glasses," *Phys. Rev. B*, vol. 71, p. 054206, Feb 2005.

[24] V. Kapko, D. A. Drabold, and M. F. Thorpe, "Electronic structure of a realistic model of amorphous graphene," *physica status solidi (b)*, vol. 247, no. 5, pp. 1197–1200, 2010.

[25] Y. Li, F. Inam, A. Kumar, M. F. Thorpe, and D. A. Drabold, "Pentagonal puckering in a sheet of amorphous graphene," *physica status solidi (b)*, vol. 248, no. 9, pp. 2082–2086, 2011.

[26] "Quantum mechanics of many-electron systems," *Proceedings of the Royal Society of London A: Mathematical, Physical and Engineering Sciences*, vol. 123, no. 792, pp. 714–733, 1929.

[27] P. Hohenberg and W. Kohn, "Inhomogeneous electron gas," *Phys. Rev.*, vol. 136, pp. B864–B871, Nov 1964.

[28] W. Kohn and L. J. Sham, "Self-consistent equations including exchange and correlation effects," *Phys. Rev.*, vol. 140, pp. A1133–A1138, Nov 1965.

[29] R. M. Martin, *Electronic Structure: Basic Theory and Practical Methods*. Cambridge: Cambridge University Press, 2004.

[30] D. M. Ceperley and B. J. Alder, "Ground state of the electron gas by a stochastic method," *Phys. Rev. Lett.*, vol. 45, pp. 566–569, Aug 1980.

[31] J. P. Perdew and A. Zunger, "Self-interaction correction to density-functional approximations for many-electron systems," *Phys. Rev. B*, vol. 23, pp. 5048–5079, May 1981.

[32] J. P. Perdew and Y. Wang, "Accurate and simple analytic representation of the electron-gas correlation energy," *Phys. Rev. B*, vol. 45, pp. 13244–13249, Jun 1992.

[33] J. P. Perdew, K. Burke, and M. Ernzerhof, "Generalized gradient approximation made simple," *Phys. Rev. Lett.*, vol. 77, pp. 3865–3868, Oct 1996.

[34] Y. Zhang and W. Yang, "Comment on "generalized gradient approximation made simple"," *Phys. Rev. Lett.*, vol. 80, pp. 890–890, Jan 1998.

[35] B. Hammer, L. B. Hansen, and J. K. Nørskov, "Improved adsorption energetics within density-functional theory using revised perdew-burke-ernzerhof functionals," *Phys. Rev. B*, vol. 59, pp. 7413–7421, Mar 1999.

[36] J. M. Soler, E. Artacho, J. D. Gale, A. Garcia, J. Junquera, P. Ordejon, and D. Sanchez-Portal, "The siesta method for ab initio order- n materials simulation," *Journal of Physics: Condensed Matter*, vol. 14, no. 11, p. 2745, 2002.

[37] J. Harris, "Simplified method for calculating the energy of weakly interacting fragments," *Phys. Rev. B*, vol. 31, pp. 1770–1779, Feb 1985.

[38] K. Laasonen, R. Car, C. Lee, and D. Vanderbilt, "Implementation of ultrasoft pseudopotentials in ab initio molecular dynamics," *Phys. Rev. B*, vol. 43, pp. 6796–6799, Mar 1991.

[39] G. Kresse and J. Furthmüller, "Efficient iterative schemes for ab initio total-energy calculations using a plane-wave basis set," *Phys. Rev. B*, vol. 54, pp. 11169–11186, Oct 1996.

[40] G. Kresse and D. Joubert, "From ultrasoft pseudopotentials to the projector augmented-wave method," *Phys. Rev. B*, vol. 59, pp. 1758–1775, Jan 1999.

[41] R. L. McGreevy and L. Pusztai, "Reverse monte carlo simulation: A new technique for the determination of disordered structures," *Molecular Simulation*, vol. 1, no. 6, pp. 359–367, 1988.

[42] R. L. McGreevy, "Reverse monte carlo modelling," *Journal of Physics: Condensed Matter*, vol. 13, no. 46, p. R877, 2001.

[43] O. George, P. T. C., B. A. S., and R. S. P., "On reverse monte carlo constraints and model reproduction," *Journal of Computational Chemistry*, vol. 38, no. 17, pp. 1547–1551, 2017.

[44] G. Opletal, T. Petersen, B. O'Malley, I. Snook, D. G. McCulloch, N. A. Marks, and I. Yarovsky, "Hybrid approach for generating realistic amorphous carbon structure using metropolis and reverse monte carlo," *Molecular Simulation*, vol. 28, no. 10-11, pp. 927–938, 2002.

[45] P. Biswas, D. N. Tafen, and D. A. Drabold, "Experimentally constrained molecular relaxation: The case of glassy $Gese_2$," *Phys. Rev. B*, vol. 71, p. 054204, Feb 2005.

[46] P. Biswas, R. Atta-Fynn, and D. A. Drabold, "Experimentally constrained molecular relaxation: The case of hydrogenated amorphous silicon," *Phys. Rev. B*, vol. 76, p. 125210, Sep 2007.

[47] H. Morita, S. Kohara, and T. Usuki, "A new reverse monte carlo simulation code combined with molecular mechanics simulation (rmcmm) for molecular and ionic liquids," *Journal of Molecular Liquids*, vol. 147, no. 3, pp. 182 – 185, 2009.

[48] A. Pandey, P. Biswas, B. Bhattarai, and D. A. Drabold, "Realistic inversion of diffraction data for an amorphous solid: The case of amorphous silicon," *Phys. Rev. B*, vol. 94, p. 235208, Dec 2016.

[49] B. Bhattarai, A. Pandey, and D. Drabold, "Evolution of amorphous carbon across densities: An inferential study," *Carbon*, vol. 131, pp. 168 – 174, 2018.

[50] B. Bhattarai, P. Biswas, R. Atta-Fynn, and D. A. Drabold, "Amorphous graphene: a constituent part of low density amorphous carbon," *Phys. Chem. Chem. Phys.*, vol. 20, pp. 19546–19551, 2018.

[51] D. Igram, B. Bhattarai, P. Biswas, and D. Drabold, "Large and realistic models of amorphous silicon," *Journal of Non-Crystalline Solids*, vol. 492, pp. 27 – 32, 2018.

[52] D. A. Keen, "A comparison of various commonly used correlation functions for describing total scattering," *Journal of Applied Crystallography*, vol. 34, pp. 172–177, Apr 2001.

[53] J.-P. Hansen and I. R. McDonald, "Chapter 4 - distribution function theories," in *Theory of Simple Liquids (Fourth Edition)* (J.-P. Hansen and I. R. McDonald, eds.), pp. 105 – 147, Oxford: Academic Press, fourth edition ed., 2013.

[54] S. V. King, "Ring configurations in a random network model of vitreous silica," *Nature*, vol. 213, p. 1112, Mar 1967.

[55] D. S. Franzblau, "Computation of ring statistics for network models of solids," *Phys. Rev. B*, vol. 44, pp. 4925–4930, Sep 1991.

[56] S. Le Roux and V. Petkov, "*ISAACS* – interactive structure analysis of amorphous and crystalline systems," *Journal of Applied Crystallography*, vol. 43, pp. 181–185, Feb 2010.

[57] P. W. Anderson, "Absence of diffusion in certain random lattices," *Phys. Rev.*, vol. 109, pp. 1492–1505, Mar 1958.

[58] J. M. Ziman, *Models of disorder*. Cambridge University Press, 1979.

[59] S. Berber, Y.-K. Kwon, and D. Tománek, "Unusually high thermal conductivity of carbon nanotubes," *Phys. Rev. Lett.*, vol. 84, pp. 4613–4616, May 2000.

[60] J. Hone, B. Batlogg, Z. Benes, A. T. Johnson, and J. E. Fischer, "Quantized phonon spectrum of single-wall carbon nanotubes," *Science*, vol. 289, no. 5485, pp. 1730–1733, 2000.

[61] A. A. Balandin, "Thermal properties of graphene and nanostructured carbon materials," *Nature Materials*, vol. 10, p. 569, Jul 2011.

[62] T. Zhu and E. Ertekin, "Phonons, localization, and thermal conductivity of diamond nanothreads and amorphous graphene," *Nano Letters*, vol. 16, no. 8, pp. 4763–4772, 2016.

[63] D. A. Drabold, "Molecular dynamics simulations of network glasses," in *Insulating and Semiconducting Glasses, series on directions in Condensed Matter Physics* (P. Boolchand, ed.), vol. 17, p. 635, Singapore: World Scientific, 2000.

[64] A. Maradudin, E. Montroll, and G. H. Weiss, *Theory of lattice dynamics in the harmonic approximation*, p. 123. New York: Academic Press, 1963.

[65] B. Bhattarai and D. Drabold, "Vibrations in amorphous silica," *Journal of Non-Crystalline Solids*, vol. 439, pp. 6 – 14, 2016.

[66] B. Bhattarai and D. Drabold, "Amorphous carbon at low densities: An ab initio study," *Carbon*, vol. 115, pp. 532 – 538, 2017.

[67] A. Pasquarello, J. Sarnthein, and R. Car, "Dynamic structure factor of vitreous silica from first principles: Comparison to neutron-inelastic-scattering experiments," *Phys. Rev. B*, vol. 57, pp. 14133–14140, Jun 1998.

[68] W. Jin, P. Vashishta, R. K. Kalia, and J. P. Rino, "Dynamic structure factor and vibrational properties of sio_2 glass," *Phys. Rev. B*, vol. 48, pp. 9359–9368, Oct 1993.

[69] P. A. Johnson, A. C. Wright, and R. N. Sinclair, "Neutron scattering from vitreous silica ii. twin-axis diffraction experiments," *Journal of Non-Crystalline Solids*, vol. 58, no. 1, pp. 109 – 130, 1983.

[70] R. M. Van Ginhoven, H. Jónsson, and L. R. Corrales, "Silica glass structure generation for ab initio calculations using small samples of amorphous silica," *Phys. Rev. B*, vol. 71, p. 024208, Jan 2005.

[71] N. Jorg and L. K.-D., "Bond angle distribution in amorphous germania and silica," *Berichte der Bunsengesellschaft fr physikalische Chemie*, vol. 100, no. 8, pp. 1341–1349, 1996.

[72] S. N. Taraskin and S. R. Elliott, "Connection between the true vibrational density of states and that derived from inelastic neutron scattering," *Phys. Rev. B*, vol. 55, pp. 117–123, Jan 1997.

[73] F. L. Galeener, A. J. Leadbetter, and M. W. Stringfellow, "Comparison of the neutron, raman, and infrared vibrational spectra of vitreous sio_2, geo_2, and bef_2," *Phys. Rev. B*, vol. 27, pp. 1052–1078, Jan 1983.

[74] J. M. Carpenter and D. L. Price, "Correlated motions in glasses studied by coherent inelastic neutron scattering," *Phys. Rev. Lett.*, vol. 54, pp. 441–443, Feb 1985.

[75] W. Humphrey, A. Dalke, and K. Schulten, "Vmd: Visual molecular dynamics," *Journal of Molecular Graphics*, vol. 14, no. 1, pp. 33 – 38, 1996.

[76] S. M. Nakhmanson and D. A. Drabold, "Approximate ab initio calculation of vibrational properties of hydrogenated amorphous silicon with inner voids," *Phys. Rev. B*, vol. 58, pp. 15325–15328, Dec 1998.

[77] R. J. Bell and D. C. Hibbins-Butler, "Acoustic and optical modes in vitreous silica, germania and beryllium fluoride," *Journal of Physics C: Solid State Physics*, vol. 8, no. 6, p. 787, 1975.

[78] S. N. Taraskin and S. R. Elliott, "Nature of vibrational excitations in vitreous silica," *Phys. Rev. B*, vol. 56, pp. 8605–8622, Oct 1997.

[79] N. Zotov, I. Ebbsjö, D. Timpel, and H. Keppler, "Calculation of raman spectra and vibrational properties of silicate glasses: Comparison between $na_2si_4o_9$ and sio_2 glasses," *Phys. Rev. B*, vol. 60, pp. 6383–6397, Sep 1999.

[80] R. O. Pohl, "Low temperature specific heat of glasses," in *Topics in Current Physics* (W. A. Phillips, ed.), vol. 24, p. 27, Berlin: Springer-Verlag Berlin Heidelberg, 1981.

[81] B. W. H. van Beest, G. J. Kramer, and R. A. van Santen, "Force fields for silicas and aluminophosphates based on ab initio calculations," *Phys. Rev. Lett.*, vol. 64, pp. 1955–1958, Apr 1990.

[82] J. Horbach, W. Kob, and K. Binder, "Specific heat of amorphous silica within the harmonic approximation," *The Journal of Physical Chemistry B*, vol. 103, no. 20, pp. 4104–4108, 1999.

[83] Taraskin, S. N. and Elliott, S. R., "Phonons in vitreous silica: Dispersion and localization," *Europhys. Lett.*, vol. 39, no. 1, pp. 37–42, 1997.

[84] M. Sadjadi, B. Bhattarai, D. A. Drabold, M. F. Thorpe, and M. Wilson, "Refining glass structure in two dimensions," *Phys. Rev. B*, vol. 96, p. 201405, Nov 2017.

[85] A. C. Ferrari and J. Robertson, "Interpretation of raman spectra of disordered and amorphous carbon," *Phys. Rev. B*, vol. 61, pp. 14095–14107, May 2000.

[86] P. Mitchell, S. Parker, A. Ramirez-Cuesta, and J. Tomkinson, "Non-hydrogenous materials and carbon," in *Vibrational Spectroscopy with Neutrons, with applications in Chemistry, Biology, Material Science and Catalysis* (J. L. Finney and D. L. Worcester, eds.), vol. 3, p. 487, Singapore: World Scientific, 2005.

[87] D. Mildner and J. Carpenter, "On the short range atomic structure of non-crystalline carbon," *Journal of Non-Crystalline Solids*, vol. 47, no. 3, pp. 391 – 402, 1982.

[88] P. Mitchell, S. Parker, A. Ramirez-Cuesta, and J. Tomkinson, "Non-hydrogenous materials and carbon," in *Vibrational Spectroscopy with Neutrons, with applications in Chemistry, Biology, Material Science and Catalysis* (J. L. Finney and D. L. Worcester, eds.), vol. 3, p. 507, Singapore: World Scientific, 2005.

[89] D. G. McCulloch, D. R. McKenzie, and C. M. Goringe, "Ab initio simulations of the structure of amorphous carbon," *Phys. Rev. B*, vol. 61, pp. 2349–2355, Jan 2000.

[90] G. Galli, R. M. Martin, R. Car, and M. Parrinello, "Ab initio calculation of properties of carbon in the amorphous and liquid states," *Phys. Rev. B*, vol. 42, pp. 7470–7482, Oct 1990.

[91] F. Li and J. S. Lannin, "Radial distribution function of amorphous carbon," *Phys. Rev. Lett.*, vol. 65, pp. 1905–1908, Oct 1990.

[92] B. O'Malley, I. Snook, and D. McCulloch, "Reverse monte carlo analysis of the structure of glassy carbon using electron-microscopy data," *Phys. Rev. B*, vol. 57, pp. 14148–14157, Jun 1998.

[93] X. Zhang and D. A. Drabold, "Direct molecular dynamic simulation of light-induced structural change in amorphous selenium," *Phys. Rev. Lett.*, vol. 83, pp. 5042–5045, Dec 1999.

[94] L. Ravagnan, F. Siviero, C. Lenardi, P. Piseri, E. Barborini, P. Milani, C. S. Casari, A. Li Bassi, and C. E. Bottani, "Cluster-beam deposition and in situ characterization of carbyne-rich carbon films," *Phys. Rev. Lett.*, vol. 89, p. 285506, Dec 2002.

[95] Y. Li and D. A. Drabold, "Symmetry breaking and low energy conformational fluctuations in amorphous graphene," *physica status solidi (b)*, vol. 250, no. 5, pp. 1012–1019, 2012.

[96] C. Wang, S. Qiu, and K. Ho, "O(n) tight-binding molecular dynamics study of amorphous carbon," *Computational Materials Science*, vol. 7, no. 3, pp. 315 – 323, 1997.

[97] D. Beeman, J. Silverman, R. Lynds, and M. R. Anderson, "Modeling studies of amorphous carbon," *Phys. Rev. B*, vol. 30, pp. 870–875, Jul 1984.

[98] S. F. Parker, S. Imberti, S. K. Callear, and P. W. Albers, "Structural and spectroscopic studies of a commercial glassy carbon," *Chemical Physics*, vol. 427, pp. 44 – 48, 2013. Advances and frontiers in chemical spectroscopy with neutrons.

[99] C. S. Casari, A. Li Bassi, A. Baserga, L. Ravagnan, P. Piseri, C. Lenardi, M. Tommasini, A. Milani, D. Fazzi, C. E. Bottani, and P. Milani, "Low-frequency modes in the raman spectrum of $sp{-}sp^2$ nanostructured carbon," *Phys. Rev. B*, vol. 77, p. 195444, May 2008.

[100] W. Kamitakahara, J. Lannin, R. Cappelletti, J. Copley, and F. Li, "Vibrational spectroscopy of c60 and graphitic carbons," *Physica B: Condensed Matter*, vol. 180-181, pp. 709 – 710, 1992.

[101] Y. Takahashi and E. F. Westrum, "Glassy carbon low-temperature thermodynamic properties," *The Journal of Chemical Thermodynamics*, vol. 2, no. 6, pp. 847 – 854, 1970.

[102] J. Robertson and E. P. O'Reilly, "Electronic and atomic structure of amorphous carbon," *Phys. Rev. B*, vol. 35, pp. 2946–2957, Feb 1987.

[103] C. Chen and J. Robertson, "Nature of disorder and localization in amorphous carbon," *Journal of Non-Crystalline Solids*, vol. 227-230, pp. 602 – 606, 1998.

[104] M. G. Tucker, D. A. Keen, M. T. Dove, A. L. Goodwin, and Q. Hui, "Rmcprofile: reverse monte carlo for polycrystalline materials," *Journal of Physics: Condensed Matter*, vol. 19, no. 33, p. 335218, 2007.

[105] K. W. R. Gilkes, P. H. Gaskell, and J. Robertson, "Comparison of neutron-scattering data for tetrahedral amorphous carbon with structural models," *Phys. Rev. B*, vol. 51, pp. 12303–12312, May 1995.

[106] A. H. Farmahini, G. Opletal, and S. K. Bhatia, "Structural modelling of silicon carbide-derived nanoporous carbon by hybrid reverse monte carlo simulation," *The Journal of Physical Chemistry C*, vol. 117, no. 27, pp. 14081–14094, 2013.

[107] A. C. Ferrari, A. Libassi, B. K. Tanner, V. Stolojan, J. Yuan, L. M. Brown, S. E. Rodil, B. Kleinsorge, and J. Robertson, "Density, sp^3 fraction, and cross-sectional structure of amorphous carbon films determined by x-ray reflectivity and electron energy-loss spectroscopy," *Phys. Rev. B*, vol. 62, pp. 11089–11103, Oct 2000.

[108] P. J. Fallon, V. S. Veerasamy, C. A. Davis, J. Robertson, G. A. J. Amaratunga, W. I. Milne, and J. Koskinen, "Properties of filtered-ion-beam-deposited diamondlike carbon as a function of ion energy," *Phys. Rev. B*, vol. 48, pp. 4777–4782, Aug 1993.

[109] C. Z. Wang and K. M. Ho, "Structural trends in amorphous carbon," *Phys. Rev. B*, vol. 50, pp. 12429–12436, Nov 1994.

[110] A. H. Farmahini and S. K. Bhatia, "Hybrid reverse monte carlo simulation of amorphous carbon: Distinguishing between competing structures obtained using different modeling protocols," *Carbon*, vol. 83, pp. 53 – 70, 2015.

[111] D. R. McKenzie, "Tetrahedral bonding in amorphous carbon," *Reports on Progress in Physics*, vol. 59, no. 12, p. 1611, 1996.

[112] S. K. Jain, R. J.-M. Pellenq, J. P. Pikunic, and K. E. Gubbins, "Molecular modeling of porous carbons using the hybrid reverse monte carlo method," *Langmuir*, vol. 22, no. 24, pp. 9942–9948, 2006. PMID: 17106983.

[113] P. Zetterstrom, S. Urbonaite, F. Lindberg, R. G. Delaplane, J. Leis, and G. Svensson, "Reverse monte carlo studies of nanoporous carbon from tic," *Journal of Physics: Condensed Matter*, vol. 17, no. 23, p. 3509, 2005.

[114] T. Petersen, I. Yarovsky, I. Snook, D. G. McCulloch, and G. Opletal, "Structural analysis of carbonaceous solids using an adapted reverse monte carlo algorithm," *Carbon*, vol. 41, no. 12, pp. 2403 – 2411, 2003.

[115] J. Pikunic, C. Clinard, N. Cohaut, K. E. Gubbins, J.-M. Guet, R. J.-M. Pellenq, I. Rannou, and J.-N. Rouzaud, "Structural modeling of porous carbons: constrained reverse monte carlo method," *Langmuir*, vol. 19, no. 20, pp. 8565–8582, 2003.

[116] D. A. Drabold, P. A. Fedders, and P. Stumm, "Theory of diamondlike amorphous carbon," *Phys. Rev. B*, vol. 49, pp. 16415–16422, Jun 1994.

[117] G. P. Lopinski, V. I. Merkulov, and J. S. Lannin, "Vibrational states of tetrahedral amorphous carbon," *Applied Physics Letters*, vol. 69, no. 22, pp. 3348–3350, 1996.

[118] C. Z. Wang and K. M. Ho, "Structure, dynamics, and electronic properties of diamondlike amorphous carbon," *Phys. Rev. Lett.*, vol. 71, pp. 1184–1187, Aug 1993.

[119] P. Papanek, W. A. Kamitakahara, P. Zhou, and J. E. Fischer, "Neutron scattering studies of disordered carbon anode materials," *Journal of Physics: Condensed Matter*, vol. 13, no. 36, p. 8287, 2001.

[120] J. Kotakoski, A. V. Krasheninnikov, U. Kaiser, and J. C. Meyer, "From point defects in graphene to two-dimensional amorphous carbon," *Phys. Rev. Lett.*, vol. 106, p. 105505, Mar 2011.

[121] H. Terrones, M. Terrones, E. Hernández, N. Grobert, J.-C. Charlier, and P. M. Ajayan, "New metallic allotropes of planar and tubular carbon," *Phys. Rev. Lett.*, vol. 84, pp. 1716–1719, Feb 2000.

[122] M. J. Lopez, I. Cabria, and J. A. Alonso, "Simulated porosity and electronic structure of nanoporous carbons," *The Journal of Chemical Physics*, vol. 135, no. 10, p. 104706, 2011.

[123] L. Alonso, J. A. Alonso, and M. J. Lopez, "Computer simulations of the structure of nanoporous carbons and higher density phases of carbon," in *Many-body Approaches at Different Scales* (G. G. N. Angilella and C. Amovilli, eds.), p. 21, Switzerland: Springer, 2018.

[124] C. de Tomas, I. Suarez-Martinez, F. Vallejos-Burgos, M. J. Lpez, K. Kaneko, and N. A. Marks, "Structural prediction of graphitization and porosity in carbide-derived carbons," *Carbon*, vol. 119, pp. 1 – 9, 2017.

[125] H. Terrones and M. Terrones, "Curved nanostructured materials," *New Journal of Physics*, vol. 5, no. 1, p. 126, 2003.

[126] H. Mohamed, A.-S. Ani, R. Xavier, K. Diego, G. Thomas, and F.-L. Paul, "Accelerating vasp electronic structure calculations using graphic processing units," *Journal of Computational Chemistry*, vol. 33, no. 32, pp. 2581–2589.

[127] M. Hutchinson and M. Widom, "Vasp on a gpu: Application to exact-exchange calculations of the stability of elemental boron," *Computer Physics Communications*, vol. 183, no. 7, pp. 1422 – 1426, 2012.

[128] V. L. Deringer, N. Bernstein, A. P. Bartk, M. J. Cliffe, R. N. Kerber, L. E. Marbella, C. P. Grey, S. R. Elliott, and G. Csanyi, "Realistic atomistic structure of amorphous silicon from machine-learning-driven molecular dynamics," *The Journal of Physical Chemistry Letters*, vol. 9, no. 11, pp. 2879–2885, 2018. PMID: 29754489.

[129] V. L. Deringer and G. Csányi, "Machine learning based interatomic potential for amorphous carbon," *Phys. Rev. B*, vol. 95, p. 094203, Mar 2017.

[130] G. Zhao, P. Buseck, A. Rouge, and M. Treacy, "Medium-range order in molecular materials: Fluctuation electron microscopy for detecting fullerenes in disordered carbons," *Ultramicroscopy*, vol. 109, no. 2, pp. 177 – 188, 2009.

[131] A. Filipponi, F. Evangelisti, M. Benfatto, S. Mobilio, and C. R. Natoli, "Structural investigation of a-si and a-si:h using x-ray-absorption spectroscopy at the si k edge," *Phys. Rev. B*, vol. 40, pp. 9636–9643, Nov 1989.

[132] J. J. Rehr, J. J. Kas, F. D. Vila, M. P. Prange, and K. Jorissen, "Parameter-free calculations of x-ray spectra with feff9," *Phys. Chem. Chem. Phys.*, vol. 12, pp. 5503–5513, 2010.

[133] M. Newville, "*IFEFFIT*: interactive XAFS analysis and *FEFF* fitting," *Journal of Synchrotron Radiation*, vol. 8, pp. 322–324, Mar 2001.

[134] D. Van Tuan, A. Kumar, S. Roche, F. Ortmann, M. F. Thorpe, and P. Ordejon, "Insulating behavior of an amorphous graphene membrane," *Phys. Rev. B*, vol. 86, p. 121408, Sep 2012.

[135] V. Kumar, T. Fujita, K. Konno, M. Matsuura, M. W. Chen, A. Inoue, and Y. Kawazoe, "Atomic and electronic structure of $pd_{40}ni_{40}p_{20}$ bulk metallic glass from ab initio simulations," *Phys. Rev. B*, vol. 84, p. 134204, Oct 2011.

APPENDIX: FEAR ALGORITHM: A BRIEF OVERVIEW

In this appendix, a brief overview of FEAR algorithm is explained. We have carried our calculations of FEAR employing **RMCProfile** [104] and *ab initio* softwares **VASP** or **SIESTA** [36]. The tutorials and manuals have made it really convenient to use. It is recommended to compile and test run each softwares (RMCProfile or SIESTA or VASP) individually before performing FEAR calculations. In particular, RMCprofile tutorials are short and really helpful to understand its working format.

This brief algorithm is written expecting that the user already is familiar with VASP or SIESTA or LAMMPS.

Running FEAR: To begin FEAR calculations, we start either with RMC calculation or relaxation of the model. In this brief overview we start with RMCProfile as our first step.

(i) Running RMCProfile:

To run RMCProfile we need to have few files in a same folder. These files are described below for **RMCProfile version 6.5.1**:

(1) **Input file, extension (*.dat):** This input file contains all the information about input environments which include: number density, maximum moving distance, minimum distances between two atoms, time limit for simulation, information about atoms and a detailed information about the experimental data file.

(2) **Position file, extension (*.rmc6f):** This file is also supplied by user. This contains the information about the box and co-ordinate position consistent with the input file (*.dat). The coordinate format should be consistent with the sample from tutorials or according to the rules mentioned in manual.

(3) **Experimental data file, extension (*.sq or *.dat or *.gr):** This file contains experimental data points obtained for a fixed incremental values that should be consistent with the input file. The extension of these experimental file can be chosen by user but it should be consistent with the input file (*.dat). Typically, experimental data file extension are choosen consistent with the experiment e.g. *.sq for structure factor, *.gr for pair correlation function and so on.

(4) **RMCProfile executable :** RMCProfile executable can be easily obtained from the **RMCProfile** software package.

A special attention should be provided naming these files. Both input file (*.dat) and position file (*.rmc6f) file should have a same name. Upon completion of simulation another file with an extension (*.his6f) is created. This file has the same format as position file (*.rmc6f) and contains the latest configuration of the atoms after the simulation. Similarly, other files with extensions: .csv, .xml and so on are generated which are well described in the manual.

(ii) Running SIESTA or VASP or LAMMPS:

For FEAR calculations we need to save at least two informations from rmcprofile run: i) Goodness of the fit (χ^2) and ii) Latest configuration simulation (*.his6f). The user needs to append the latest configuration (*.his6f) in desired format (*.xyz, compatible with Jmol and ISAACS). Thus multiple FEAR runs create multiple sets of configuration (multiple *.xyz). Further, this latest configuration has to be converted in appropriate input file for (VASP or SIESTA or LAMMPS). All the other files which are surplus to the calculation are usually erased (except files 1-4 and saved files).

Similarly few files have to be included in the same folder for these runs for e.g: SIESTA (*.psf. *.fdf (includes position and boxsize consistent with rmcprofile calculation) and siesta executable) or VASP (KPOINTS, POTCAR, POSCAR (from

rmcprofile), INCAR). After performing the relaxation we again save the appropriate informations like final configuration energy, final configuration and so on. All the unnecessary files excluding those required to run are deleted. This practice helps to keep track of all the files and is easier to debug. Finally from the final configuration new position file (*.rmc6f) is created. This new position file replaces the old position file and the calculation keeps moving in a cyclic process until the desired accuracy for χ^2 and final energy is obtained.

Thesis and Dissertation Services